ABSTRACT

Title of Thesis: INVESTIGATION OF GRAPHENE AND OTHER LOW DIMENSIONAL MATERIALS

Jacob Alexander Tosado, Doctor of Philosophy, 2017

Thesis directed by: Professor, Michael Sears Fuhrer, Department of Physics

This thesis describes experiments to characterize defects in two-dimensional materials and understand their effect on electrical conductivity. Defects limit the electrical conductivity through a material by scattering electrons. Understanding the physics of defects is therefore essential to building materials and structures with novel electronic properties. This dissertation has focused on low dimensional materials because they are simple thereby allowing for more advanced theory and they will act as a foundation for understanding higher dimensional systems.

High resolution x-ray photoelectron spectroscopy (XPS) and near edge x-ray absorption fine structure spectroscopy (NEXAFS) were used to determine the character of vacancy defects in graphene. Vacancies were induced in graphene on a thermally oxidized silicon substrate using argon ion bombardment. XPS of the carbon 1s core level of pristine graphene shows a C 1s spectrum consistent with a single C 1s

peak broadened both instrumentally and by a Doniach-Sunjic type effect. As defects are created, the resulting spectrum is deconvolved into two peaks. The first retains the same spectral width as that for the pristine graphene but with a reduced intensity. The broader second peak at higher binding energy (~200 meV), increases in intensity with increasing defect concentration. This second peak is identified as the experimental XPS signature of defective graphene. The observation is somewhat at odds with theoretical calculations of XPS spectra for graphene with various vacancy arrangements, which generally produce C 1s peaks shifted to lower binding energy. Instead, the emergence of this second peak, together with the emergence of a single sharp resonance seen near the vacuum level in the NEXAFS spectra, is interpreted as a distribution of molecular-like states forming on the surface.

Preliminary efforts were made to characterize defects in semiconducting monolayer MoS2 using scanning tunneling microscopy (STM) and spectroscopy (STS). Techniques for obtaining a clean MoS2 surface suitable for ultra-high vacuum STM were developed, and preliminary characterization of the single layer tungsten disulfide surface by STM and STS was carried out. The local density of states of MoS2, as measured by STS, shows the semiconducting bandgap as well as signatures of donor and acceptor states within the gap.

INVESTIGATION OF GRAPHENE AND OTHER LOW DIMENSIONAL MATERIALS

by

Jacob Alexander Tosado

Thesis submitted to the Faculty of the Graduate School of the
University of Maryland, College Park, in partial fulfillment
of the requirements for the degree of
Doctorate of Philosophy in
Physics
2017

Advisory Committee:
Professor Ellen D. Williams, Chair
Theodore Einstein
Michael S. Fuhrer
Min Ouyang
Janice Reutt-Robey

Dedicated to my mother Diane Tidball

To remind her that

Given great expectations, a good will and absolute perseverance
***Y**ou can achieve anything*

Acknowledgements

Firstly, I am thankful to Dr. Ellen D. Williams for her initial support of my scientific career. It was this initial connection which allowed me to move forward and move faster. Secondly and equally, I am thankful to Dr. Michael S. Fuhrer for providing me with a realm of opportunities which has allowed me to grow both scientifically and as an individual. I am grateful to Dr. Min Ouyang for his passion in the context of building scientific equipment. I am grateful for the very interesting intellectual conversation and help provided by Dr. Theodore Einstein specifically in logic and higher level physics. I am thankful to Dr. Janice Reutt-Robey for her sense of propriety with regard to scientific inquiry and presentation. I am grateful to Dr. Karen Gaskell for her advice and trust with regard to scientific equipment. I am grateful to Dr. Vince Ballarotto and Dr. Dan Hines at the Laboratory for Physical Sciences for their useful conversation. I am grateful for the many conversations with my once graduate colleagues Dr. Brad Conrad, Dr. Michelle Groce, Dr. Kristen Burson, Dr. Mahito Yamamoto, and Jonathan Larson. I am grateful for all the founding support from my mentors at the University of Florida, namely, Dr. Amlan Biswas, Dr. Christopher Stanton, Dr. Guido Mueller, Dr. Tara Dahkal, Dr. Sung Hee Yun, Dr. Yoonseok Lee, Dr. Arthur Hebard, Dr. Eugene Dunam, Dr. Khandker Muttalib and Dr. Bernard Whiting. I am also grateful for all the founding support from my mentors at Miami-Dade College, namely, Prof. Diane McKinney, Prof. Bird and Dr. Felix Rodriguez-Trelles. Thank you Steven Bachmeyer!

Thanks to Donna Hammer for her support in academic outreach at the University of Maryland. Thanks to Wendy Wexler for her support in academic outreach at the City of Greenbelt. Thanks to Dr. Peter Shawhan, Lorraine DeSalvo, Jessica Crosby, Linda Ohara, Mary Sutton and Margaret Lukomska for their help in organization.

Thanks to my family. I love you all!

Finally, I would like to acknowledge Nightvid Cole, Laura Serong, Simcha Korenblit, James Davis, Emmitt Thompson, Amruta Deshpande, Cathy Ye, Linda Watson and Bonnie Richards-Becker for their friendship, intellectual conversation and creativity.

Thank you Katy!

Contents

List of Figures

List of Tables

Chapter 1

Introduction

Low-dimensional materials are systems described with an electronic state wave function confined to less than three spatial dimensions. The carbon-based nanomaterials are the modern archetype. Reduced dimensional systems have generally been crucial to the development of modern electronic devices. Transistors, which are the core element of modern electronics, are typically formed by the two-dimensional interface between a silicon surface and its oxide layer. From this, the study of surfaces and interfaces are integral to understanding low-dimensional material systems.

With two-dimensional materials the surface of a two-dimensional crystal is also its interior. Therefore, studying the surfaces of these materials is essential to understanding these materials as a whole. Many experimental methods have been used to study surfaces [16] [17]. In this thesis I will describe the three main methods I have used in the course of my dissertation to study two-dimensional monolayer materials. These three are reflective bright field Raman spectroscopy, x-ray photoelectron spectroscopy and scanning tunnelling spectroscopy. I have used these methods to mainly investigate graphene, grown through chemical vapour deposition (CVD), on silicon dioxide substrates. I have also completed preliminary work on two other low-dimensional materials, namely, molybdenum disulphide and tungsten disulphide.

In this chapter I will lay out the structure of this thesis and briefly summarize the information in each chapter. This thesis has six chapters. Chapter 2 introduces the physics of low-dimensional materials with defects, graphene being the archetype. Chapter 3 introduces Raman scattering in graphene and highlights the work I have published using Raman scattering to qualify dry transferred graphene films. Chapter 4 is a literature review of photoelectron spectroscopy on graphene and other graphene like materials. Chapter 5 discusses the work I have done using photoelectron spectroscopy to examine defected graphene. Chapter 6 introduces the methods of scanning tunnelling microscopy

and spectroscopy and describes my effort to apply these methods to understand other low dimensional materials, specifically molybdenum disulphide and tungsten disulphide.

Chapter 2 opens by discussing the importance of understanding the roll defects play in the electrical conduction of low dimensional materials, specifically graphene. In the second section of this chapter you will find a complete derivation of the graphene electronic band structure. The last section of this chapter describes briefly how defects limit the conductivity of graphene.

Chapter 3 opens by discussing Raman spectroscopy of graphene. In the first section the three characteristic G, 2D and D resonances are highlighted. The second section describes the experimental uncertainty inherent in a reflective bright field Raman spectra measurement. The third section describes how I applied Raman spectroscopy to qualify the successful dry transfer of CVD grown graphene on copper foil to polystyrene substrates. In this qualification, spectra were used to map the transfer printed surface at the micron scale. These local measurements were found to be consistent with global millimetre scale sheet resistance measurements.

Chapter 4 is a literature review of photoelectron spectroscopy on graphene and graphene-like systems in the context of defects. The first section covers the basic physics of x-ray photoelectron spectroscopy (XPS) in the context of graphene. The second section covers the basic physics of near edge x-ray absorption fine structure (NEXAFS) in the context of graphene. The third section covers the mechanics of the x-ray photoelectron spectrometer. In the fourth section the graphene system is compared to carbon, carbon nanotubes, fullerenes and boron nitride thin films.

Chapter 5 describes work that was done on CVD graphene transferred to thermally oxidized silicon substrates. The data presented here shows how the carbon 1s binding energy changes when defects are added in situ. It is found that the C 1s photoelectron lineshape splits into two nearly unresolvable peaks. As defects are added, a higher binding energy peak emerges while the pristine state peak is suppressed. The effect is seen together with the emergence of a sharp resonance in the near edge x-ray absorption fine structure. These two clues suggest that graphene, becoming activated through the addition of defects, forms a molecular-like surface states.

Chapter 6 describes work I completed to design a room temperature scanning probe microscope and my later application of scanning probe spectroscopy at low temperatures to other low dimensional materials, specifically molybdenum disulphide and tungsten disulphide. In the first section I review in detail the method of scanning tunnelling and atomic force microscopy. In the following section I discuss calibration techniques for imaging and local density of states measurements. The last section show preliminary

data on bulk molybdenum disulphide and monolayer CVD tungsten disulphide on a sapphire substrate.

There are two main publications associated with this thesis. The first is the work of Lock et al. (2011) [18]. This work is the main result of chapter 3. The second work, Tosado et al. (2017) [19], will be immediately submitted for publication. This work is the main result of chapters 4 and 5.

Chapter 2

Two Dimensional Crystals

Defects limit the electrical conduction through a material by acting as electron scattering centers. The practical perfect crystal should then maximize conduction [1] and be well understood by models of standard solid state textbooks. It is from this starting point that theory strives to understand the defects that perturb a crystal from its pristine state so as to harness and tailor a material's properties. A defect, being the quantum of imperfection, is classified by both its dimension and size. Point defects, dislocations, grain boundaries and precipitates refer to a dimensionality of zero, one, two and three, respectively. These categories are descriptive and increase in complexity with increasing dimension. To this, the size of the defect will then limit the scale over which that defect type will affect the bulk crystal properties.

2.1 Low-Dimensional Materials

The carbon based nanomaterials such as carbon fullerenes, nanotubes and graphene are arguably the prime experimental realization of zero, one and two dimensional crystals, respectively. Graphene is fundamentally the simplest and it is the theoretical basis for the other two [20]. Remarkably its properties adhere quite well to the basic nearest neighbour tight binding approximation for low energy electrons.

Graphene is a two-dimensional sheet of carbon atoms and can be grown from organic gases or produced through mechanical exfoliation of graphite. In this material, specifically near the Fermi level, electrons are analogous to relativistic massless charge carriers owing to their dispersion being well described by the Dirac equation. The first measurements of graphene's carrier mobility at room temperature were in excess of 15,000

[1] Bloch theory suggests that an electron in a perfect lattice experiences no collisions. See Ashcroft and Mermin (1976), p.315

$cm^2\ V^{-1}\ s^{-1}$ [20], which is an order of magnitude greater than is expected for many metals[2] [21]. This carrier mobility is practically independent of temperature between 10 K and 100 K [22][23][24]. This indicates that the dominant scattering mechanism is due to defects. For graphene adhered to a SiO_2 substrate the mobility is limited by defects in the form of charged impurities from the substrate [25] [26] and so, one finds that the mobility can be greater by an order of magnitude from simply using a more chemically inert substrate such as hexagonal boron nitride [27] [28].

The two-dimensionality of graphene makes it unique in that, unlike three-dimensional crystals, the bulk plays just as an important role in the crystal's boundary conditions as do the edges. With this, defects within the bulk are expected to significantly change its chemical reactivity. Indeed, how truly two-dimensional graphene is has been greatly questioned. Graphene in absence of a substrate supporting structure has been expected to bend or crumple into a fluctuating three-dimensional structure [29]. If such fluctuations could be achieved the structure could be further modified, for example, by introducing vacancy defects which would produce an auxetic material (a material that has a negative coefficient of expansion along its transverse axis) [30].

In all, the simplicity of the graphene system allows for advanced studies of many-body interactions. The physics of graphene and other two-dimensional materials have natural parallels to quantum electrodynamics. These parallels are also the foundation of semiconducting and superconducting materials, where defects are ultimately the main limiting factor of the conductivity. Eventually it may be possible to investigate the details of quantum field theory [31]. To date, the study of graphene like systems has led to the realization of topological insulators, a material type with the potential to revolutionize modern electronics [32]. To begin however, the following sections of this chapter will focus on graphene's electronic structure and from that, electron transport in graphene in the presence of defects.

2.2 Graphene

Carbon has four valence electrons. From valence bond theory three out of the four half filled valence electron orbitals can hybridize to sp^2 orbitals. This allows in-plane carbon-carbon σ bonds between adjacent atoms which forms the graphene crystal. The fourth p_z orbital overlaps with neighbouring p_z orbitals creating an out-of-plane π bond. In the context of molecular orbital theory the bonding of the carbon atoms has the effect of removing the energy degeneracy possessed by each atomic orbital in isolation. This serves to create bonding and antibonding states.

[2] That is to say, a non-degenerate free electron gas

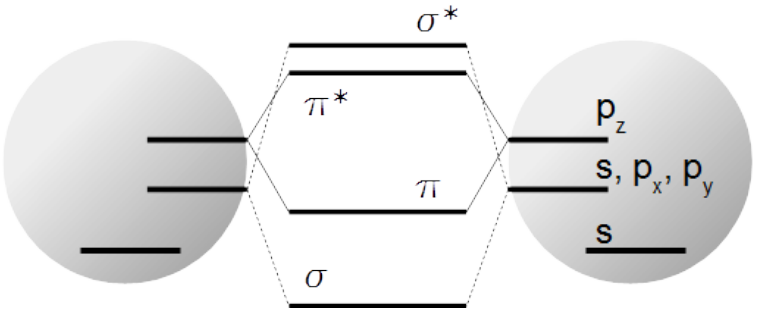

FIGURE 2.1: Energy diagram showing how the atomic orbitals of two carbon atoms break their degeneracy at close proximity

For π bonds (and equivalently σ bonds), bonding and antibonding states are referred to as π and π^* states, respectively. The bonding state has a spatially symmetric wave function with a lower energy than the antibonding one. Ultimately, the σ bonds account for the majority of graphene's structural properties while the π bonds account for the majority of graphene's electronic properties at low energies. The following analysis focuses on that band structure which originates from the overlap of the π electrons.

2.2.1 The Graphene Lattice

Graphene has a two-dimensional honeycomb structure which is described by a hexagonal lattice which has two atoms associated with each lattice point and thus two atoms within each Wigner-Seitz cell. Alternatively, it can be viewed as a bipartite lattice composed of two interpenetrating triangular sublattices. Since the real space lattice is hexagonal so too is the corresponding reciprocal lattice, rotated by 90^o. Let $\mathbf{G}$ be the location of the $\bar{\Gamma}$ symmetry point at the center of the Brillouin zone and $\mathbf{G}_i$ be the location of the center of the i^{th} Brillouin zone, i.e. the position of the respective lattice points in reciprocal space. The reciprocal lattice is best described as the set $\{\mathbf{G}_i | \mathbf{G}_i = n_1\mathbf{b}_1 + n_2\mathbf{b}_2 \ \forall \ n_1, n_2 \in \mathbb{Z}\}$ such that,

$$\mathbf{b_1} = 2\pi \frac{\mathbb{R}\ \mathbf{a_2}}{\mathbf{a_1} \cdot \mathbb{R}\ \mathbf{a_2}} \tag{2.1a}$$

$$\mathbf{b_2} = 2\pi \frac{\mathbb{R}\ \mathbf{a_1}}{\mathbf{a_2} \cdot \mathbb{R}\ \mathbf{a_1}} \tag{2.1b}$$

Here the matrices, $\mathbb{R}$, are 90^o rotation matrices. High symmetry points, $\bar{K}$, at the corners of the Brillouin zone, located by the reciprocal lattice vectors $\mathbf{K}_i$, are thus,

$$\mathbf{K}_1 = \frac{1}{3}(2\mathbf{G_2} + \mathbf{G_1}), \tag{2.2a}$$

$$\mathbf{K}_2 = \frac{1}{3}(\mathbf{G_2} - \mathbf{G_1}), \tag{2.2b}$$

$$\mathbf{K}_3 = \mathbf{K}_1 - \mathbf{G_1} - \mathbf{G_2}, \tag{2.2c}$$

$$\mathbf{K}_4 = -\mathbf{K}_2 - \mathbf{G_2}, \tag{2.2d}$$

$$\mathbf{K}_5 = -\mathbf{K}_1 - \mathbf{G_2}, \tag{2.2e}$$

$$\mathbf{K}_6 = \mathbf{K}_2 + \mathbf{G_1}. \tag{2.2f}$$

Notice that there are two distinct symmetry point or "K-points"[3] located by $\mathbf{K}_1$ and $\mathbf{K}_2$. The other corners of the Brillouin zone differ from these two by only reciprocal lattice vectors and are therefore indistinguishable.

Graphene's lattice can be classified as the plane group p6mm[4]. In this sense all translations commute with reflections in the plane of the lattice. This implies that all electron (and phonon) eigenstates are either even or odd under reflection. The segregation of the electron states into σ and π bonds accentuate this idea. The even states lie in the nodal plane of the crystal and are symmetrical with respect to rotation about the bond axis. These states compose the σ bonds. The odd states lie outside of the nodal plane but are cylindrically symmetric within it. These half-filled states lie near the Fermi level, are electrically active (in the low energy limit) and thus compose π bonds [33][34]. For this reason, the π states are the easiest to access by experimental probing.

2.2.2 The Hamiltonian of Graphene using the Tight-Binding Model

To understand the basic electronic behaviour of graphene it is necessary to describe the behaviour of its π electrons. Using the tight-binding model for their description assumes that each π electron should be tightly bound to its originating carbon atom and should have limited interactions with the states and potentials of neighbouring atoms in the crystal. The degree of limitation will be conceptualized by the overlap integral matrix $\hat{S}$.

Each atom in the lattice is located at sublattice points "A" and "B" corresponding to vectors $\mathbf{R}_a = n_1\mathbf{a}_1 + n_2\mathbf{a}_2$ and $\mathbf{R}_b = \mathbf{R}_a + \Delta\mathbf{r}$ with $\Delta\mathbf{r} = -\frac{1}{3}(\mathbf{a}_1 + \mathbf{a}_2)$ such that

[3] The symbols $\bar{K}$ and $\bar{\Gamma}$ formally refer to the two-dimensional symmetry points, as standard in surface science, whereas the terms K-point or Γ-point are the common reference to these symmetry points in experimental literature.

[4] This plane group assumes all the symmetries of the lattice are in a plane

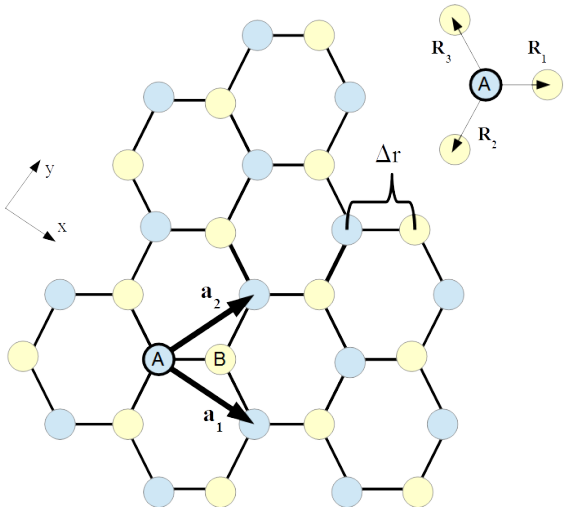

FIGURE 2.2: Atomic Lattice Vectors $\mathbf{a_1}$ and $\mathbf{a_2}$. Nearest neighbour vectors $\mathbf{R_1}$, $\mathbf{R_2}$ and $\mathbf{R_3}$, see equations 2.10. The carbon-carbon spacing, $\mathbf{\Delta r}$

$\mathbf{a}_1 = \sqrt{3}a_o\hat{x}$ and $\mathbf{a}_2 = \frac{1}{2}\sqrt{3}a_o\hat{x} + \frac{3}{2}a_o\hat{y}$[5]. If now $\chi(\mathbf{r})$ is the normalized $2p_z$ atomic orbital wave function of an isolated carbon atom then let $|\mathbf{R}\rangle$ be the corresponding carbon atom orbital wave function positioned at lattice point $\mathbf{R}$. Since there are two atoms in each Wigner-Seitz cell (at site A and B), one can expect the π electron wave function to have a two-dimensional basis such that each basis function is formed from the isolated carbon atom wave function at the respective lattice sites. Translational symmetry from Bloch's theorem and normalization of these basis functions, in the context of the tight binding model for graphene, yield two basis wave functions which are Bloch wave functions[6], i.e.,

$$|\phi_1\rangle = \frac{1}{\sqrt{N}}\sum_a e^{i\mathbf{k}\cdot\mathbf{R}_a}|\mathbf{R}_a\rangle, \tag{2.3a}$$

$$|\phi_2\rangle = \frac{1}{\sqrt{N}}\sum_b e^{i\mathbf{k}\cdot\mathbf{R}_b}|\mathbf{R}_b\rangle. \tag{2.3b}$$

In the low energy limit (near the Fermi level) it is safe to assume that no other orbitals can mix with with the p_z orbitals. Therefore, from the basis wave functions the eigenstates can be written as,

$$|\psi\rangle = \alpha|\phi_1\rangle + \beta|\phi_2\rangle. \tag{2.4}$$

[5]Carbon atoms are separated by a distance a_o equal to 1.42Å.

[6]Keep in mind that while the two basis states are different, their form involves the same orbital for both the "A" and "B" sites.

These eigenstates must of course satisfy the Schrödinger equation, i.e.,

$$\hat{H}|\psi\rangle = \mathbb{E}|\psi\rangle \tag{2.5}$$

where $\hat{H}$ is the graphene Hamiltonian and $\mathbb{E}$ is the energy of the π electron[7]. Following the derivation of Wallace, (1947) [35], the components of the Hamiltonian can now be described in terms of the basis states of the crystal. This is to say that, the inner product of the Schrödinger equation with either basis function yields,

$$\langle\phi_1|\hat{H}|\psi\rangle = \mathbb{E}\langle\phi_1|\psi\rangle \text{ and} \tag{2.6a}$$
$$\langle\phi_2|\hat{H}|\psi\rangle = \mathbb{E}\langle\phi_2|\psi\rangle. \tag{2.6b}$$

This implies that,

$$\begin{bmatrix} H_{11} & H_{12} \\ H_{21} & H_{22} \end{bmatrix} \begin{bmatrix} \alpha \\ \beta \end{bmatrix} = E \begin{bmatrix} S_{11} & S_{12} \\ S_{21} & S_{22} \end{bmatrix} \begin{bmatrix} \alpha \\ \beta \end{bmatrix} \tag{2.7}$$

where $H_{ij} = \langle\phi_i|\hat{H}|\phi_j\rangle$ and $S_{ij} = \langle\phi_i|\phi_j\rangle$ correspond to the elements of $\hat{H}$ and $\hat{S}$, respectively. While there are two distinct lattice sites, each carbon atom is identical to its neighbour. With this in mind, the energy of a p_z electron of an isolated carbon atom is then

$$\mathbb{E}_{p_z} = \langle\phi_1|\hat{H}|\phi_1\rangle = \langle\phi_2|\hat{H}|\phi_2\rangle. \tag{2.8}$$

The off diagonal elements are related due to the Hamiltonian being Hermitian, i.e.,

$$H_{12} = H_{21}^* \tag{2.9}$$

These elements correspond to the energy needed for a π electron to "hop" from one lattice site to another. If only hops to nearest neighbours are considered, then these

[7] $\mathbb{E}$ will be used as opposed to E to distinguish energy from electric field.

off-diagonal elements take a fairly simple expression. To formulate this, first consider an A lattice site at the origin, namely, $\mathbf{R}_a = \mathbf{0}$. Next, consider the three B site nearest neighbours to this A site, namely, $\mathbf{R}_b = \mathbf{R}_1$, $\mathbf{R}_2$ and $\mathbf{R}_3$ where

$$\mathbf{R}_1 = \mathbf{0} + \Delta\mathbf{r}, \tag{2.10a}$$

$$\mathbf{R}_2 = \mathbf{a}_1 + \Delta\mathbf{r} \text{ and} \tag{2.10b}$$

$$\mathbf{R}_3 = \mathbf{a}_2 + \Delta\mathbf{r}. \tag{2.10c}$$

The off-diagonal elements then take the form,

$$\begin{aligned} H_{12} = \langle\phi_1|\hat{H}|\phi_2\rangle &= \frac{1}{\sqrt{N}}\sum_a e^{-i\mathbf{k}\cdot\mathbf{R}_a}\langle\mathbf{R}_a|\hat{H}(\frac{1}{\sqrt{N}}\sum_b e^{i\mathbf{k}\cdot\mathbf{R}_b}|\mathbf{R}_b\rangle) \\ &= \frac{1}{N}\langle\mathbf{0}|\hat{H}|\mathbf{R}_{N.N.}\rangle(e^{i\mathbf{k}\cdot\mathbf{R}_1} + e^{i\mathbf{k}\cdot\mathbf{R}_2} + e^{i\mathbf{k}\cdot\mathbf{R}_3}) \end{aligned} \tag{2.11}$$

where $\langle\mathbf{0}|\hat{H}|\mathbf{R}_{N.N.}\rangle = \langle\mathbf{0}|\hat{H}|\mathbf{R}_1\rangle = \langle\mathbf{0}|\hat{H}|\mathbf{R}_2\rangle = \langle\mathbf{0}|\hat{H}|\mathbf{R}_3\rangle$. The quantity $\frac{1}{N}\langle\mathbf{0}|\hat{H}|\mathbf{R}_{N.N.}\rangle = -t \approx 2.75$ eV is the "hopping integral" [36] which represents the kinetic energy of electrons hopping between atoms. The value of t is chosen to match first-principles calculations of graphene's band structure around the corners of the Brillouin zone to experimental observation [37].

As for the overlap integral matrix $\hat{S}$, its elements can be formulated similarly. The overlap integral can be visualized as a measure of the mutual resemblance of the wave functions of two basis states [38]. In this case, $S_{11} = S_{22} = \langle\phi_1|\phi_1\rangle = 1$ (i.e., a basis wave function resembles itself 100%) and

$$S_{12} = S_{21}^* = \langle\phi_1|\phi_2\rangle = \frac{1}{N}\langle\mathbf{0}|\mathbf{R}_{N.N.}\rangle(e^{i\mathbf{k}\cdot\mathbf{R}_1} + e^{i\mathbf{k}\cdot\mathbf{R}_2} + e^{i\mathbf{k}\cdot\mathbf{R}_3}) \tag{2.12}$$

Here, the quantity $s = \frac{1}{N}\langle\mathbf{0}|\mathbf{R}_{N.N.}\rangle$ is also experimentally determined. For the purpose of this chapter $s \approx 0$[8] which simplifies the Schrödinger equation to yield the secular

[8] In practice, s, is on the order of 0.13, see Saito (1998) p.27 [36]

equation

$$0 = det(\hat{\mathbf{H}} - \mathbb{E}\mathbf{1}) \tag{2.13a}$$

$$0 = det\begin{bmatrix} \mathbb{E}_{p_z} - \mathbb{E} & -t(e^{i\mathbf{k}\cdot\mathbf{R}_1} + e^{i\mathbf{k}\cdot\mathbf{R}_2} + e^{i\mathbf{k}\cdot\mathbf{R}_3}) \\ -t(e^{-i\mathbf{k}\cdot\mathbf{R}_1} + e^{-i\mathbf{k}\cdot\mathbf{R}_2} + e^{-i\mathbf{k}\cdot\mathbf{R}_3}) & \mathbb{E}_{p_z} - \mathbb{E} \end{bmatrix} \tag{2.13b}$$

$$0 = \mathbb{E}_{p_z}^2 + \mathbb{E}^2 - 2\mathbb{E}_{p_z}\mathbb{E} - t^2(e^{-i\mathbf{k}\cdot\mathbf{R}_1} + e^{-i\mathbf{k}\cdot\mathbf{R}_2} + e^{-i\mathbf{k}\cdot\mathbf{R}_3}) (e^{i\mathbf{k}\cdot\mathbf{R}_1} + e^{i\mathbf{k}\cdot\mathbf{R}_2} + e^{i\mathbf{k}\cdot\mathbf{R}_3}) \tag{2.13c}$$

$$0 = \mathbb{E}^2 - 2\mathbb{E}\mathbb{E}_{p_z} + \mathbb{E}_{p_z}^2 - t^2(3 + e^{i\mathbf{k}\cdot\mathbf{a}_1} + e^{i\mathbf{k}\cdot\mathbf{a}_2} + e^{-i\mathbf{k}\cdot\mathbf{a}_1} + e^{i\mathbf{k}\cdot\mathbf{a}_2 - i\mathbf{k}\cdot\mathbf{a}_1} + e^{-i\mathbf{k}\cdot\mathbf{a}_2} + e^{i\mathbf{k}\cdot\mathbf{a}_1 - i\mathbf{k}\cdot\mathbf{a}_2}) \tag{2.13d}$$

Substituting for a_1 and a_2 gives,

$$0 = \mathbb{E}^2 - 2\mathbb{E}\mathbb{E}_{p_z} + \mathbb{E}_{p_z}^2 - t^2(3 + e^{\sqrt{3}ik_x a_o} + e^{-\sqrt{3}ik_x a_o} + e^{\frac{1}{2}\sqrt{3}ik_x a_o + \frac{3}{2}ik_y a_o} + e^{-\frac{1}{2}\sqrt{3}ik_x a_o - \frac{3}{2}ik_y a_o} + e^{-\frac{1}{2}\sqrt{3}ik_x a_o + \frac{3}{2}ik_y a_o} + e^{\frac{1}{2}\sqrt{3}ik_x a_o - \frac{3}{2}ik_y a_o}) \tag{2.14a}$$

$$0 = \mathbb{E}^2 - 2\mathbb{E}\mathbb{E}_{p_z} + \mathbb{E}_{p_z}^2 - t^2[3 + e^{\sqrt{3}ik_x a_o} + e^{-\sqrt{3}ik_x a_o} + (e^{\frac{1}{2}\sqrt{3}ik_x a_o} + e^{-\frac{1}{2}\sqrt{3}ik_x a_o})(e^{\frac{3}{2}ik_y a_o} + e^{-\frac{3}{2}ik_y a_o})] \tag{2.14b}$$

$$0 = \mathbb{E}^2 - 2\mathbb{E}\mathbb{E}_{p_z} + \mathbb{E}_{p_z}^2 - t^2[3 + 2cos(\sqrt{3}k_x a_o) + 4cos(\frac{1}{2}\sqrt{3}k_x a_o)cos(\frac{3}{2}k_y a_o)] \tag{2.14c}$$

which implies that

$$\mathbb{E} = \mathbb{E}_{p_z} \pm H_{12} = \mathbb{E}_{p_z} \pm t\sqrt{3 + 2cos(\sqrt{3}k_x a_o) + 4cos(\frac{1}{2}\sqrt{3}k_x a_o)cos(\frac{3}{2}k_y a_o)} \tag{2.15}$$

It is common to use this energy corresponding to $s \approx 0$ where the "plus" case is energy of the antibonding state and the "minus" is the energy of the bonding state. In reference to figure 2.3, notice that these two energies are degenerate at just the K-points of the Brillouin zone. For this reason, graphene is a zero-band-gap semiconductor.

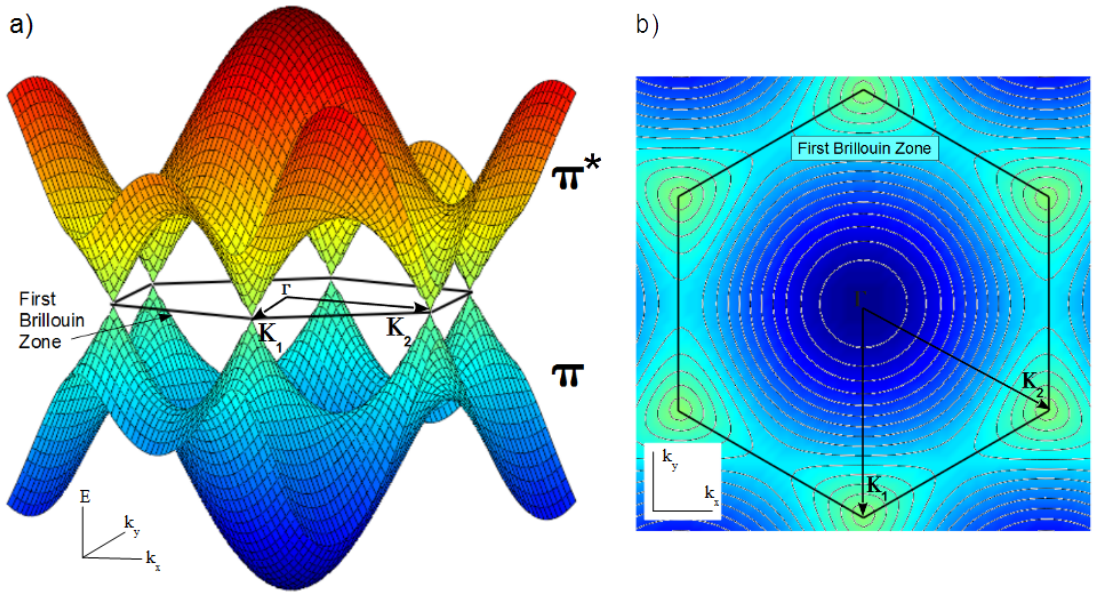

FIGURE 2.3: a) Graphene π and π^* dispersion ($\mathbb{E}(k_x, k_y)$) around the Brillouin zone. b) Contour plot of the dispersion around the first Brillouin zone.

2.2.3 The Low-Energy Limit

Low energy excitations of π electrons into the conducting π^* state are more likely to occur near the K-points. A description of situations where only these excitations are likely gives reason to Taylor expand graphene's Hamiltonian about these points. Consider a circle about the $\mathbf{K}_1$ location, i.e., some $\mathbf{k} = \mathbf{K}_1 + \Delta\mathbf{k}$.

$$\hat{H} = \hat{H}_o - \frac{3}{2\hbar} a_o t \begin{bmatrix} 0 & \hbar(\Delta k_x - i\Delta k_y) \\ \hbar(\Delta k_x + i\Delta k_y) & 0 \end{bmatrix}$$

$$= \hat{H}_o - \frac{3}{2\hbar} a_o t(\hbar\Delta k_x \sigma_x + \hbar\Delta k_y \sigma_y) = \hat{H}_o - v_F \sigma \cdot \mathbf{p} \tag{2.16}$$

This is analogous to the Dirac equation for massless fermions moving at velocity v_F rather than the speed of light c. The low energy limit dispersion relation is thus,

$$\mathbb{E} = \mathbb{E}_{p_z} \pm \frac{3}{2} a_o t \sqrt{\Delta\mathbf{k}_x^2 + \Delta\mathbf{k}_y^2}. \tag{2.17}$$

This describes the energy of the charge carriers in the lattice near the K-points. Knowing the energy gives an associated frequency according to $\omega = \mathbb{E}/\hbar$ and thus a group velocity

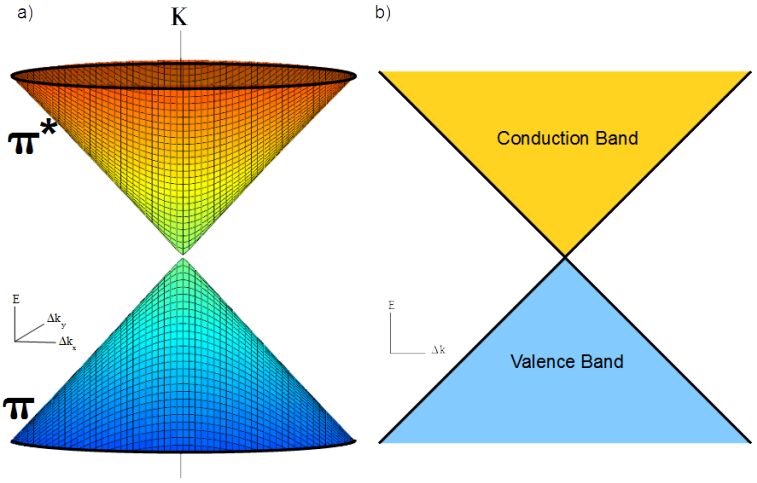

FIGURE 2.4: a) Graphene π and π^* dispersion ($E(\Delta k_x, \Delta k_y)$) in the low energy limit. b) A simpler depiction of the linear dispersion around the $\bar{K}$-point.

$v = d\omega/dk = \hbar^{-1}(d\mathbb{E}/dk)$. In a metal the group velocity of the charge carriers is known to be the Fermi velocity, i.e.,

$$v_{_F} = \frac{1}{\hbar}\frac{d\mathbb{E}}{dk} = \frac{3}{2\hbar}a_o t \approx \frac{1}{300}c \tag{2.18}$$

which is of the order of magnitude typical for metals. The dispersion is clearly linearly increasing, i.e.,

$$\mathbb{E} = \mathbb{E}_{p_z} \pm v_{_F}\hbar\Delta k \tag{2.19}$$

where

$$\mathbb{E}_{_F} = \hbar v_{_F} k_{_F}. \tag{2.20}$$

is the Fermi energy.

The dispersion in in equation 2.19 is similar to other massless particles (e.g. photons, where $\mathbb{E} = ck$).

The resulting identification of the Pauli spin matricies, σ_x and σ_y, indicate that the charge carriers in graphene have a pseudo-spin that is in the same direction as that particle's momentum.

The linear dispersion relation also yields a linear density of states. To understand this consider first that some number of electron states is proportional to the product of the density of those electron states with some energy over a range, in other words

$$N = \int_{\pm\infty} D(\mathbb{E})\ d\mathbb{E}. \tag{2.21}$$

Or in differential form,

$$D(\mathbb{E}) = \frac{dN}{d\mathbb{E}} \tag{2.22}$$

which is the density of electron states per unit energy. In order to describe the two-dimensional graphene electron density one must first consider the volume of momentum states,

$$\mathbb{V}_k = \pi k^2 \tag{2.23}$$

so that the volume in a region between k and $k + dk$ is

$$d\mathbb{V}_k = 2\pi k\ \ dk \tag{2.24}$$

It has been assumed that a single electron state has momentum $\mathbf{k} = k_x\hat{x} + k_y\hat{y}$ where $k_i = n_i\pi L_i^{-1}$ and let $n = 2$ for periodic boundary conditions so that the volume of momentum for this single state is $4\pi^2 V_o^{-1}$. Thus, the number of single-electron states is,

$$dN = (4)2\pi k(4\pi^2\mathbb{V}_o^{-1})^{-1}dk = 4\mathbb{V}_o k\pi^{-1}dk \tag{2.25}$$

(where a factor of four has been included for spin and valley degeneracy)

or in terms of energy where $k = \frac{\mathbb{E}}{\hbar v_F} \Rightarrow (dk/d\mathbb{E}) = \frac{1}{\hbar v_F}$ which implies that

$$dN = 2\mathbb{V}_o \mathbb{E}\pi^{-1}\hbar^{-2}v_F^{-2}\ d\mathbb{E}. \tag{2.26}$$

The density of states per unit energy is then

$$D(\mathbb{E}) = (dN/d\mathbb{E}) = 2\mathbb{V}_o E\pi^{-1}\hbar^{-2}v_F^{-2} \qquad \text{or} \tag{2.27}$$

$$D(\mathbb{E}) = \frac{2\mathbb{V}_o \mathbb{E}}{\pi\hbar^2 v_F^2}. \tag{2.28}$$

Hence, one can write the density of states per energy per volume, i.e.,

$$D(\mathbb{E})_{\mathbb{V}} = \frac{2\mathbb{E}}{\pi\hbar^2 v_F^2}. \tag{2.29}$$

For the rest of this thesis the graphene density of states in this last expression, equation 2.29, will be referred to as, $D(\mathbb{E})$ for simplicity.

2.2.4 Defects and Measurement

Defects, in the form of dopants, will tend to impact the net electron and hole concentrations within graphene and should manifest as changes in the electrical, magnetic, and optical properties [39]. In the presence of defects it is reasonable to expect the lowest energy electrons to be easily scattered and, in this regime, these electrons would have a non-zero effective mass that would impead their conduction [40][41].

For defect types such as lattice vacancies or charged impurities, the conductivity has been expected to take the following two forms [40][42][43]:

Charged Impurities

$$\sigma = C_{imp}\frac{q^2}{h}\frac{n}{n_{imp}} \tag{2.30}$$

Lattice Vacancies

$$\sigma = C_{vac}\frac{q^2}{h}\frac{n}{n_{vac}}ln^2(k_F R) \tag{2.31}$$

In equation 2.30, C_{imp}, depends on the fine structure constant for graphene and n_{imp} is the charged impurity density. For equation 2.31, C_{vac}, depends on k_F, R is the defect radius which is modeled as a circular region within which the sublattice symmetry is broken and, n_{vac}, is the vacancy defect density.

These two expressions of graphene's conductivity essentially behave the same in that they are both proportional (or nearly proportional) to n/n_d, where n is the carrier density and n_d is the specified defect density. This makes the presence of defects obvious but distinguishing between two types of defects difficult. The dependence on $1/n_d$ comes from Matthiessen's rule and is expected for any type of disorder.

The linear dependence on the carrier density, n, is not obvious and happens to be similar for both charged impurities and lattice vacancies. The carrier density is not exactly the same in either case. For vacancies there is an additional dependence on n through the factor of k_F in the log term. In general, once a current is established in the material, it will be the density of defects which will control a time, τ, over which that current will decay to zero.

The well-known conductivity of graphene takes the form,

$$\sigma = \frac{1}{2}q^2 v_f^2 \tau D(\mathbb{E}) \tag{2.32}$$

where q is the carrier charge, v_F is the Fermi velocity of the carriers, $D(\mathbb{E})$ is the graphene density of states and τ will be known as the total relaxation time which is inversely proportional to the total scattering rate. The total rate, from Matthiessen's rule, is no more than the sum of rates from the constituent scattering processes within the crystal. So too will the net scattering rate from a defect distribution be the scaled rate from scattering off a single such defect [44]. Thus a defect scattering rate is proportional to the defect density, i.e.,

$$\frac{1}{\tau_d} \propto n_d \tag{2.33}$$

The total defect scattering rate follows from Fermi's golden rule,

$$\frac{1}{\tau_d} = \frac{2\pi}{\hbar}|\langle\psi_f|V_d|\psi_i\rangle|^2 D(\mathbb{E}) \tag{2.34}$$

The defect potential, V_d, is again Coulombic and falls off as r^{-1}. To understand how V_d relates to energy, the defect potential must be Fourier transformed into reciprocal space which implies,

$$V_d \propto \frac{1}{k_F} \qquad \text{and that implies} \qquad V_d \propto \frac{1}{\mathbb{E}}$$

Now since

$$D \propto \mathbb{E} \qquad \text{then} \qquad \frac{1}{\tau_d} \propto \frac{1}{\mathbb{E}}$$

Consider now that the carrier density, n, is the total carrier density of all availble carriers. This is an integration of the product of the density of states with the total electron distribution, f_o, over those states taken with respect to the entire conduction band [44], i.e.,

$$n = \int_0^\infty f_o(\mathbb{E})D(\mathbb{E})\ d\mathbb{E} = \int_0^\infty (dn/d\mathbb{E})\ d\mathbb{E} \tag{2.35}$$

For energies near the Fermi level in graphene, where the integration is valid, n, can be expanded to second order.

$$n \approx n\Big|_0 + (dn/d\mathbb{E})\Big|_0 \mathbb{E} + \frac{1}{2}(d^2n/d\mathbb{E}^2)\Big|_0 \mathbb{E}^2 = \frac{\mathbb{E}^2}{2\pi\hbar^2 v_F^2} \tag{2.36}$$

This implies that,

$$\mathbb{E} \propto n^{1/2} \quad \Rightarrow \quad D \propto \mathbb{E} \propto n^{1/2} \quad \text{and}$$
$$\tau_d \propto \mathbb{E} \propto n^{1/2} \quad \text{as well.}$$

Therefore, defect scattering draws the expectation that the conductivity is proportional to the ratio of carrier density to the defect density, i.e.,

$$\sigma \propto \frac{n}{n_d} \tag{2.37}$$

This result is due to a bare defect potential. This defect inside the crystal, forces a charge distribution to form immediately around it thereby screening its potential. Thus, within the crystal, the net scattering potential is a superposition of the defect potential and the screening potential. Surprisingly, due to the non-linear screening in graphene (the screening wavevector is proportional the Fermi wavevector) equation 2.37 holds even for the screened potential [42]. The screened potential may be calculated using various approximations, such as the Random Phase Approximation, to obtain the constant C_imp in equation 2.30.

Generally, the presence of defects has the potential to decrease the electron mobility by several orders of magnitude [45][46][47][48][49][50][51][52] [53]. The situation becomes even more complex when the defect density becomes a non-negligible fraction of the crystal medium. High densities of lattice vacancies remove long range order. Charged impurities, in contrast, have the potential to break the carbon-carbon symmetry of the lattice which is expected to open up a band gap, bringing on ferromagnetism or even superconductivity [48][54] [55].

It is also known that in the limit of complete chemical saturation, an insulating state is achieved. In this limit graphene oxide is a prime example of where graphene loses its semi-metallic transport properties [56]. Just below this limit graphene is in a nearly fully reversible regime where graphene's chemical and electronic properties have the potential to be controllably tuned by changing its chemical environment. Reversibility is also important in the context of graphene intercalation compounds which have the potential for novel energy storage technologies [57].

Chapter 3

Raman Spectroscopy on transfer printed CVD Graphene

The work preformed in this chapter was published by ACS Nano Letters in 2011 [18]. Evgeniya H. Lock, Mira Baraket, Matthew Laskoski, Shawn P. Mulvaney, Woo K. Lee, Paul E. Sheehan, Daniel R. Hines, Jeremy T. Robinson, Jacob Tosado, Michael S. Fuhrer, Sandra C. Hernandez, and Scott G. Walton were authors. Substrate preparation and the production of graphene films as described in this publication was preformed and coordinated by Dr. E. H. Lock with the others at the Naval Research Laboratory. Dr. D. R. Hines, Dr. E. H. Lock and I worked worked together to transfer print graphene from copper to the substrates described and characterize their resistance. All Raman measurements were performed at the University of Maryland by this dissertation author. All authors participated in the analysis of the data and the writing of the manuscript.

In this chapter I will discuss Raman spectroscopy as a method of detecting defects in graphene. I will first briefly introduce Raman scattering in graphene, then describe the work I did using this technique to characterize the quality of graphene films transferred onto polystyrene substrates.

3.1 Raman Scattering

The most direct way to distinctly observe defects is with scanning tunnelling microscopy. While that may be, the scale of such measurements is typically on the order of Ångströms, which is three orders of magnitude smaller than the transport scale of typical graphene devices. Thus, practical STM measurements are strongly local and not strictly representative of the bulk system without some other form of detection.

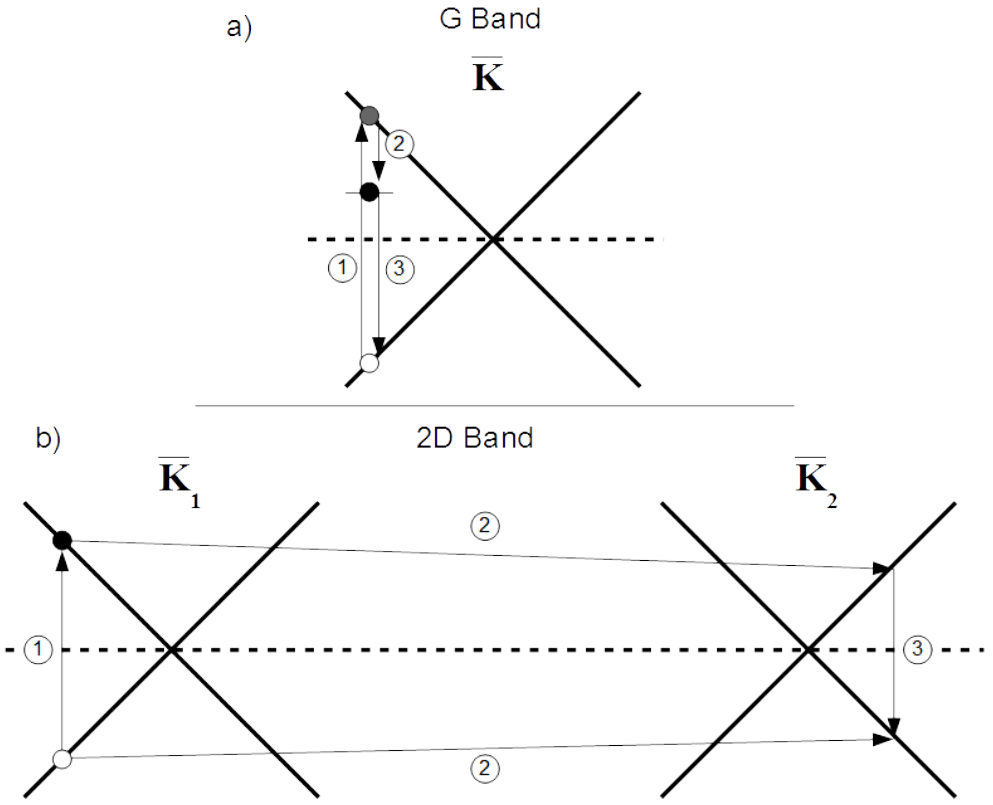

FIGURE 3.1: a) G band scattering mechanism 1. Carrier-hole photoexcitation 2. Scattering from the lattice, production of zero momentum phonons, decay into a virtual state 3. Stokes shifted radiative recombination; b) 2D band scattering mechanism 1. Carrier-hole photoexcitation 2. Scattering from the lattice, production of K-point phonons by both the carrier and the hole 3. Stokes shifted radiative recombination (see also reference [1])

Raman scattering in the optical regime is strongly sensitive to backscattering centers and is the simplest way to characterise defects in graphene devices. To understand why, one must first recall that in the absence of scattering centers, charge carriers are ballistic (equation 2.19), only scattering off the lattice in ways that allow momentum conservation. The charge carriers in graphene are observed to scatter in modes that leave behind either a single motionless phonon or two high momentum phonons. The dispersion for graphene phonons is well known[1].

A Raman signal due to the first scattering mechanism, figure 3.1a, results from carriers scattering off the lattice that leave behind zero-momentum phonons. This scattering mechanism forces the scattered carriers into a virtual state at a slightly lower energy, which then radiatively recombine with their holes. This recombination process is enhanced when the virtual states are closer to actual states, so much so that, only resonant Raman scattering is effectively observed. The resulting phonons exist at the Γ-point, and the observed Stokes shift in reflected light is consequently known as the G band.

[1]Consider the doctoral thesis of Jun Yan from Columbia University (2009), p.26. http://library.columbia.edu/subject-guides/southasia/resources/eresources/dissertations.html

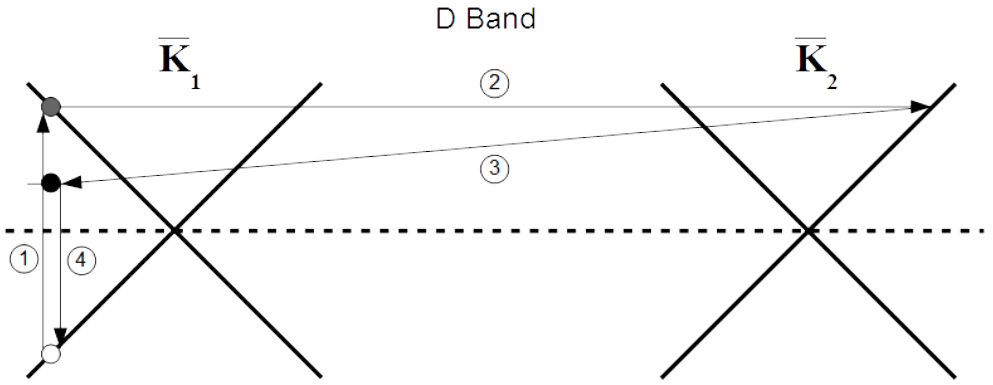

FIGURE 3.2: D band scattering mechanism 1. Carrier-hole photoexcitation 2. Backscattering event 3. Scattering from the lattice, production of a K-point phonon, decay into a virtual state 4. Stokes shifted radiative recombination (see also reference [1])

The second scattering mechanism, figure 3.1b, involves both a carrier and its hole. The scattering process reverses the direction of the carrier and hole such that they each leave behind a high-momentum phonon. This quasi-backscattering mechanism is allowed only because the net change in momentum and pseudo-spin is zero and is due to a strong natural coupling of the photo-electric born carriers at the K-point to high momentum K-point phonons. This inter-valley mechanism, in that carriers will scatter from one K-point to another (equation 2.2), produces a Stokes shift in the reflected light known as the 2D band for reasons that will be explained in the following.

In the presence of scattering centers, backscattering without momentum conservation becomes allowed in that no new particles need to be created to explain the momentum and spin reversal. In such a system, access to K-point phonons is enhanced [1] in that a backscattering event will allow the production of K-point phonons to conserve the carrier-hole momentum (see figure 3.2). The cost of energy in this scattering mechanism is half that of the 2D scattering, and the resulting Stokes shift in the reflected light is known as the D band. Thus, the 2D band can then be thought of as an overtone of the D band.

Originally the D band was observed to be a function of graphite crystallite size, where the crystallite edges were understood to be the source of the backscattering. With the discovery of crystalline graphene, defects are understood to be a comparable source of backscattering centers due to two main factors. The first is the large momentum transfer between $\bar{K}_1$ and $\bar{K}_2$, which is on the order of an inverse lattice constant. The second is that the carrier pseudospin has to flip which implies that the disorder must be sharp on the atomic scale, and break sublattice symmetry. Hence, the D band is thought to signify the presence of point defects localised on one of the sublattices. This makes a measurement of the D band intensity a direct way of quantifying defect concentrations

below 10 %[2] [58]. In fact, the degree of Stokes shift allows one to distinguish between defects resulting from donors and acceptors [59] although charged impurities are not expected to give a significant D peak.

Raman spectroscopy as a mode of defect characterization, as it stands, has its limitations. For structural defects specifically, at concentrations towards and above 1% the intensity of the D band depends more weakly on concentration and tends to saturate [58]. At these concentrations the chemical state of the crystal has been changed drastically and notable changes in chemical potential are expected. In this regime, binding energy measurement become worthwhile.

Ultraviolet and x-ray photoemission spectroscopy allows the experimenter to probe electron energies from the Fermi level down to the core levels providing insight not only into electron-electron interactions but also into bonding arrangements. The following chapter will focus on the science of x-ray photoemission spectroscopy specifically in the context of defected graphene.

3.2 Raman Scattering with Reflective Bright Field Microscopy

A standard light source for Raman spectroscopy is a narrow band laser with spectral width on the order of a few hundred MHz. The 00 transverse electromagnetic mode (TEM) is always used for simplicity. Often, the laser light will become contaminated with spurious Raman signals by interacting with various optical components in the apparatus. The band and mode can be further purified using apertures and intermediate gratings.

To investigate opaque thin film devices a reflective bright field microscope is used. In this set up, the laser light is collimated then directed into the rear aperture of a microscope objective lens through reflection off a narrow band low pass filter. The filter used in the experiment described in the next section has a 100 wave number (cm^{-1}) threshold. The light exits the front aperture of the objective, interacts and thereby reflects off of the thin film surface which is then collected by the same objective lens. This reflected light is now passed through the filter and towards the detector. It is this pass through the filter which blocks the source wavelength and transmits the red shifted Raman scattered light. Before the transmitted light hits the detector the light is dispersed by a grating.

[2]This is the ratio of defects to carbon atoms. A concentration of 10% corresponds to a 0.5 nm crystallite size, refer to the inset of figure 6 in reference [58].

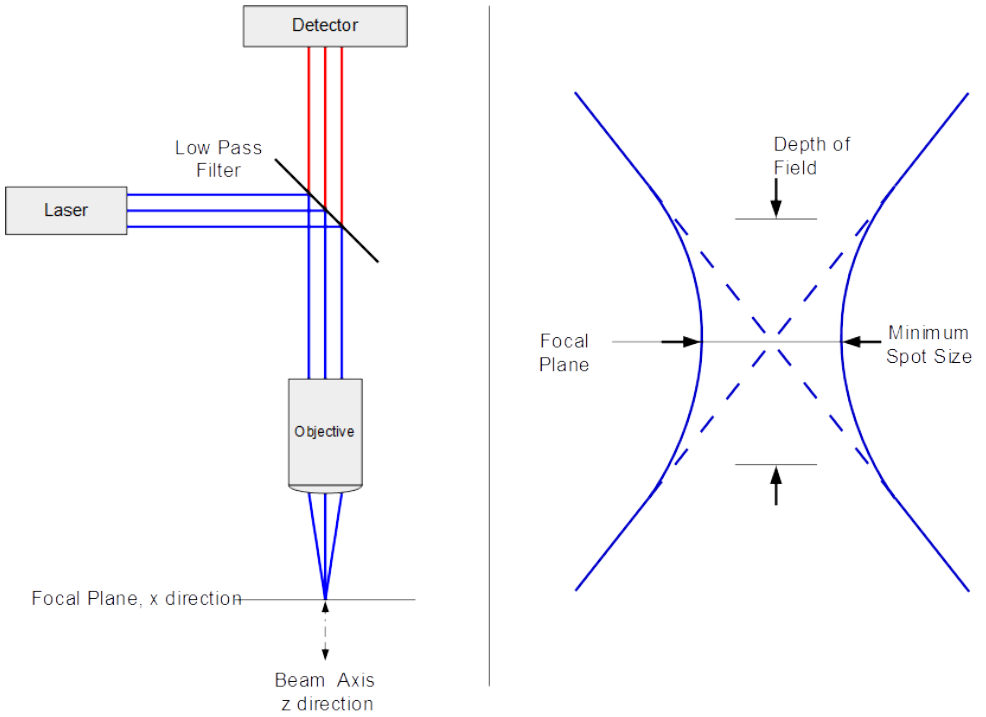

FIGURE 3.3: (Left) Basic concept of an optical bright field microscope. Collimated light is emitted from a laser and directed into an objective lens. This light is then focused to a point on the focal plane. That light is reflected by a device surface at the focal plane back into the objective. The light is recollimated and then filtered by a low pass filter. The filtered light is then measured by a detector.

The grating used in the experiment described had 300 rulings per millimeter which corresponds to about three data points per cm^{-1}.

The measurements described in the next section are Raman maps of a monolayer graphene surface. The features in these maps are determined by the resolution of the microscope. The resolution is characterized by the size of the laser spot on the device surface[3]. The theoretical minimum spot size can be estimated using Rayleigh's criterion knowing the wavelength of light and numerical aperture.

$$\Delta x_o = \frac{1.22\lambda}{\mathrm{NA}} \tag{3.1}$$

Here, Δx_o, is the resolution or minimum lateral feature size detectable in the focal plane which is approximately the full width of the spot at half the maximum intensity (FWHM). The term λ, represents the wavelength of the light used and, NA, is the numerical aperture of the objective lens. For a 632.8 nm HeNe laser focused through a 0.9 NA objective, the minimum spot size will be in the neighbourhood of 860 nm.

[3]I am assuming the device surface is always in focus.

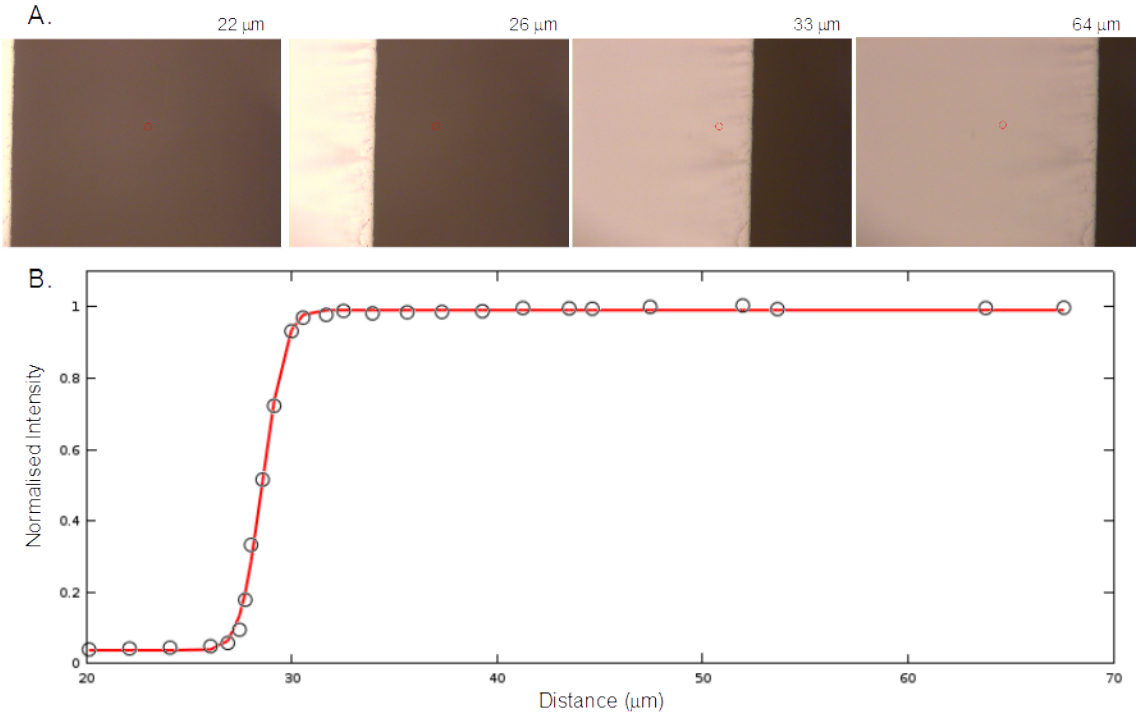

FIGURE 3.4: Measurement of the intensity of a HeNe laser spot. A) Gold thermally evaporated onto a glass slide provides the metallic edge. As the slide is translated through the field of view the reflected intensity increases. B) Normalized reflected intensity (black circles) as a function of distance. The resulting profile is described by a cumulative distribution function (red curve).

This can be confirmed by measuring the width of the spot with a metallic edge. By translating a metallic edge in the focal plane through the focal point and measuring the reflected intensity one will observe a cumulative distribution of the Gaussian intensity. Figure 3.4A shows a metallic gold edge being translated through the focal plane. As the edge intercepts the focal point of the objective lens more intensity is reflected back. The resulting spot size of the error function fit, shown in figure 3.4B, reveals a spot size of about 890 nm.

The numerical aperture together with the minimum spot size also determines the resolution normal to the focal plane. A 00 transverse electromagnetic mode (TEM) beam will have a Gaussian profile which implies that, as the beam converges to the focus, it becomes hyperboloidal, i.e.,

$$\Delta x = \Delta x_o \sqrt{1 + \frac{z^2}{\Delta z_o^2}} \tag{3.2}$$

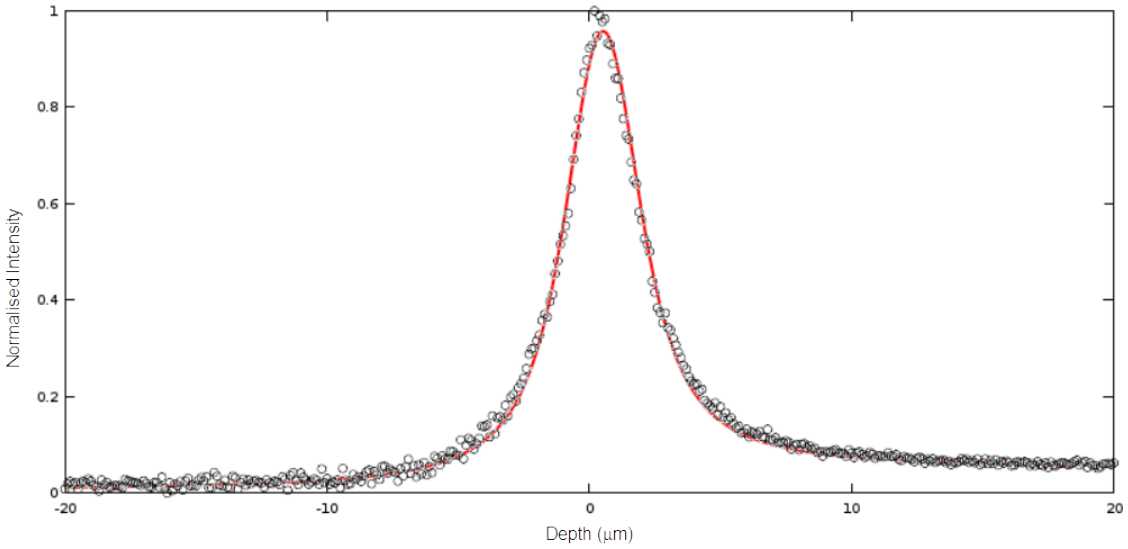

FIGURE 3.5: (Black circles) Measurement of the focused laser intensity as the focus is moved normal to a reflecting surface. (Red curve) Fit to the data based on equation 3.3. The depth of field, Δz_o, measured to be 1.7 μm

Since the beam intensity is inversely proportional to the area of the spot, the intensity of the beam along the beam axis will be Lorentzian, i.e.,

$$I \propto \frac{1}{\Delta x_o^2(1+\frac{z^2}{\Delta z_o^2})} \tag{3.3}$$

Here, the FWHM of the resulting Lorentzian, Δz_o, defines the resolution of the minimum feature size resolvable in the direction along the beam axis known as the depth of field. This quantity can be measured by translating a reflecting surface normal to the beam axis through the focal plane. Figure 3.5 shows the resulting intensity variation for a 532 nm laser. The resulting Lorentzian width, based on equation 3.3, is 1.7 μm indicating the depth of field for the 0.9 NA objective used. In the next section these resolution limits will be considered in the measurements taken.

3.3 Raman Spectroscopy of Graphene on Polystyrene

Monolayer graphene films were grown through chemical vapour deposition (CVD) on copper foil substrates as described below. These films were then both transfer printed, as described below, onto polystyrene substrates and wet transferred [60] to thermally oxidized silicon substrates. Prior to growth, the 1 cm square 0.25 mm thick copper foil substrates were pressed flat between two glass slides to remove large scale corrugation

which aids in the transfer of the graphene to other flat surfaces. Once pressed, the copper substrates were then sonicated in a sequence of 10 mL of acetone and then in an equal amount of isopropyl alcohol. Following the sonication, the substrates were then immediately heated under a glass cover at 100^o C to quickly remove the solvent.

The cleaned copper substrates contained in a quartz crucible were placed in a 1 inch diameter single zone tube furnace. The substrates were heated to 985^o C in a hydrogen and argon atmosphere for 30 minutes. This has the effect of decomposing large hydrocarbons from the surface. The resulting smaller radical components are expected to combine with the flow of hydrogen to form substances that are either aromatic or gaseous which would then be carried away by the gaseous flow.

After this, the flow of hydrogen was reduced and a flow of methane was introduced. The methane decomposes, allowing the carbon to deposit on the copper surface. This deposition process was expected to be self-limiting in that, once a complete monolayer is on the surface, the process would stop. Complete coverage was established within 5 minutes by prior examination of samples with Raman spectroscopy. Therefore, the growth was limited to 5 minutes. To stop growth, the flow of hydrogen and methane was removed. A flow of argon continued until the system was back to room temperature.

Polystyrene substrate surfaces treated with low energy electron beam-generated plasma and then dipped in N-ethylamino-4-azidotetrafluorobenzoate (TFPA-NH_2) [18]. Polystyrene (PS) was chosen for two reasons. Firstly, because it is a well-characterized polymer with simple chemical composition and can thus serve as a model substrate to understand the basic requirements for graphene transfer. Secondly, polystyrene in its native state has a low adhesion to graphene. Therefore, the surface chemistry of polystyrene can be systematically varied to enhance the adhesion to graphene and ensure transfer.

To transfer print graphene onto the PS, the substrates were placed in contact with the CVD grown graphene-covered copper foil and pressed together under heat and pressure with a NX 2000 Nano Imprinter. Since the TFPA acts as an adhesive, the graphene was thereby printed onto the substrates. Proof and ultimately the quality of the transfer was provided in two ways. The first was a four probe push contact measurement of the resistance per square. This was a global measurement. The second was to map the intensity of the characteristic Raman peaks for graphene described in the previous section over a continuous area. This was a local measurement. These measurements at their respective scales give definition to the quality of a particular transfer.

At the local 80 μm scale , mapping of the printed surface via Raman spectroscopy confirmed the transfer of graphene to polystyrene and measured the uniformity of the transfered graphene film. As shown in figure 3.6, graphene was transferred to PS H and

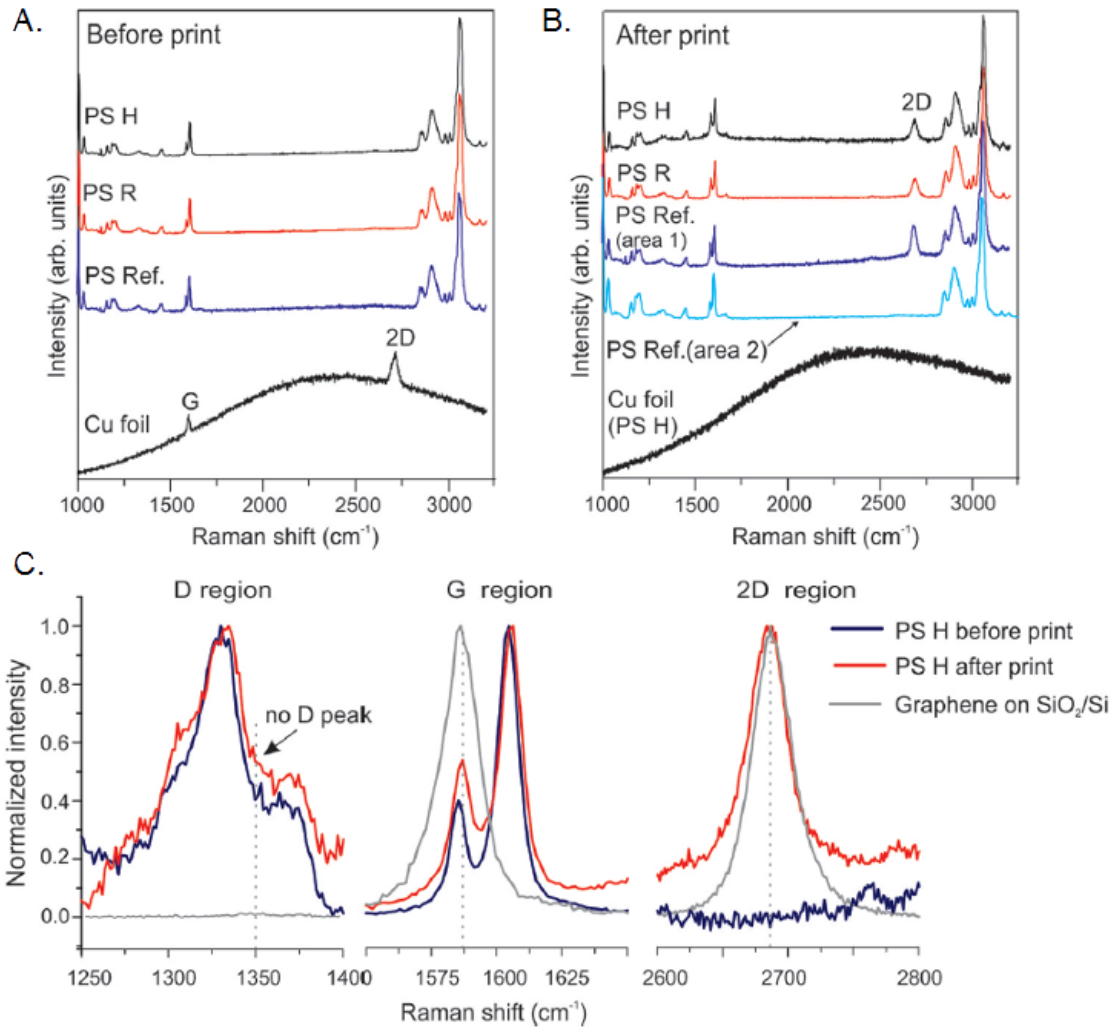

FIGURE 3.6: Raman spectra of polystyrene surfaces. Panels (a) and (b) show the samples named PS ref, PS H, PS R, and Cu foil before and after print, respectively. Panel (c) shows high-resolution D, G, and 2D regions of PS H before and after print. As a reference, graphene on SiO2/Si substrate is included.

PS R as signified by the appearance of the 2D peak on the TFPA-treated polystyrene and the absence of that peak on the copper foil after print. A comparison of PS H with graphene transferred onto thermally oxidized silicon substrates using a wet transfer (figure 3.6C) indicates that the 2D graphene peak on PS matches the peak position (2686 cm^{-1}). It also matches the peak width ($\approx$ 23 cm^{-1}) of graphene/SiO2/Si. The peak width is also of importance since a larger peak width would be indicative of a possible folding of the graphene onto itself. Thus, the graphene printed onto the polymer substrate is of relatively high quality and single layer [61] [1].

In the regions of the D- and G-peak of graphene, polystyrene shows several Raman modes that obscure the observation of the graphene modes. However, an increase of peak height at the 1586 cm^{-1} is clearly visible and indicative of the graphene G-peak. A closer look at the D region revealed no change in the shape of the peak around 1350

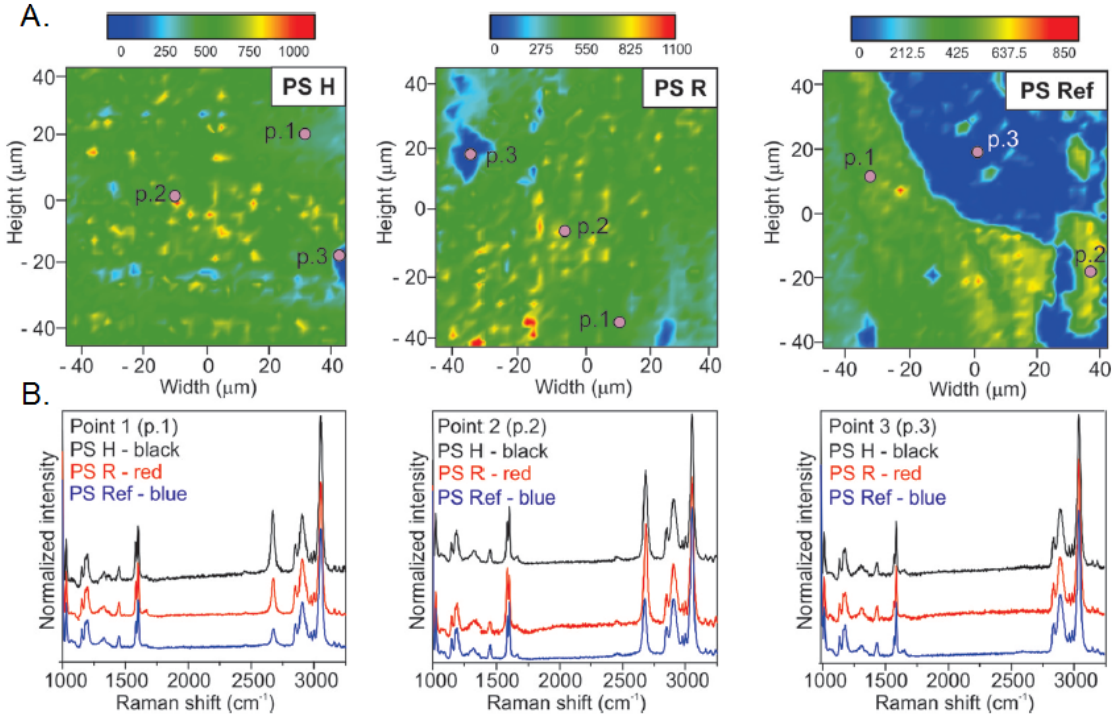

FIGURE 3.7: Microraman maps A) of PS H, PS R, and PS ref after print and the corresponding Raman spectra at chosen points B) of each map.

cm^{-1}, suggesting negligible D peak and thus no significant increase in point defects in the graphene layer during transfer. This is perhaps surprising because the covalent bonding of the TFPA to graphene may be expected to create defects. Interestingly, the signature graphene peaks were detected on some areas of the unmodified sample as well (figure 3.6B, PS ref area 1). This might be because the printing temperature is above the glass transition temperature allowing for good conformal contact at the polymer/graphene interface.

The micro-Raman maps (Figure 3.7A) of the 2D peak intensity over about an 800 μm^2 area show uniform coverage for PS H and PS R. This was not true for PS ref where large areas with no graphene signature were observed. Here, it is important to keep in mind that the polymer surface roughness after printing was on the order of ones of microns which is at the edge of the 1.4 μm depth of field for the instrument as discussed in the previous section. Thus, some intensity variation over large areas should not be surprising. To better characterize this phenomenon, I performed a survey of individual Raman spectra over many different locations (examples are shown in Figure 3.7B). This revealed that intensities lower than 200 (dark blue color in Figure 3.7A) is likely to be bare polymer and intensities above 200 are likely to be transferred graphene while the overall variations in intensity (light blue to red color in Figure 3.7A) reflect the variation in height.

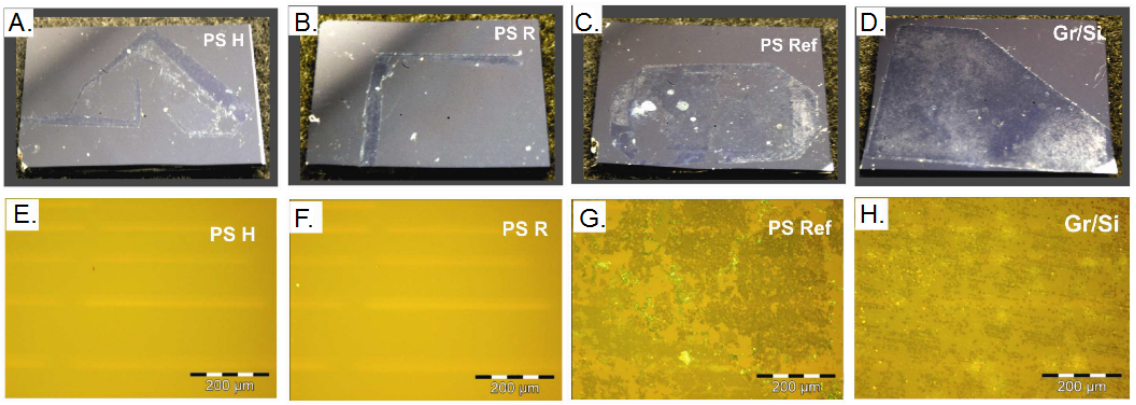

FIGURE 3.8: Photographs (top row) and corresponding microscope images (bottom row) for PS-H (A, E), PS-R (B,F), PS ref (C, G) and graphene on SiO2/Si (D, H). In this work the polymer samples were smaller than the graphene/Cu substrates and so in cases (A) and (B) the residues on the Si wafers are the edges of the graphene/Cu foil that did not come into contact with the polymer surface during print. Thus, these images (A, B) suggest that in PS H and PS R cases graphene was completely transferred to the whole adhesion treated polystyrene surface

Alternatively, the uniformity of the transferred graphene on the macroscale can be evaluated by analysing the residual graphene left over on the copper foil substrates after transfer printing. I accomplished this by dissolving away the printed copper growth substrates in an ammonium persulfate solution leaving only a film of the residual graphene film backed by a poly-methyl methacrylate (PMMA) over layer on the liquid surface. The residual films were then transferred to thermally oxidized silicon substrates. The PMMA is then washed away leaving only the graphene. This is the common wet transfer process. Figure 3.8 shows the outcome. For the PS H and the PS R transfers, only graphene from the foil edges, which did not come into contact with PS, remain. This together with the Raman data of figure 3.7 indicate that full transfer of graphene onto the PS H and PS R substrates was achieved, while for the reference sample (PS ref) only a partial transfer was observed.

To confirm electrically what is evident in figure 3.8, a standard 4-point probe configuration was used on a 1 mm square of each sample, refer to reference [18]. The insulating polymer surface was indeed found to be conducting after transfer with low sheet resistances of 1 (PS H) and 3 kΩ/sq (PS R). These values are consistent with the sheet resistance (<1 kΩ/sq) of monolayer graphene transferred to PET and SiO2/Si[62] [63] [64]. The reference sample (PS ref) did not show measurable conductivity, which is consistent with the incomplete transfer suggested in figure 3.8C and G.

This dry transfer of graphene from copper foil to PS, based on the enhanced adhesion of the polystyrene surface using TFPA, allows the copper foil growth substrate to be reused. This is not possible in the wet transfer method where it is entirely dissolved away. The graphene monolayer transferred to the treated polymer was uniform and of

high quality as signified by a narrow 2D peak width (23 cm^{-1}) and low sheet resistance (1-3 kΩ/sq)[4]. The size of the transferred area is limited only by the size of the growth Cu foil and the polystyrene sheet. Therefore in principle, this method can be applied to transfer graphene to a wide range of organic or inorganic substrates. Additionally, transfer from other growth substrates should also be possible as well.

[4]Complementary measurements of the carbon 1s photoelctron line, the conductivity and mobility were also taken, see Lock et al., (2011) [18] for details

Chapter 4

X-Ray Spectroscopic Methods to Characterize 2-D Materials

4.1 X-Ray Spectroscopic Methods to Characterize 2-D Materials

This chapter is a literature review of photoelectron spectroscopy on graphene and graphene-like systems in the context of defects. The first section covers the basic physics of x-ray photoelectron spectroscopy (XPS) in the context of graphene. The second section covers the basic physics of near edge x-ray absorption fine structure (NEXAFS) in the context of graphene. The third section covers the mechanics of the x-ray photoelectron spectrometer. In the fourth section the graphene system is compared to carbon, carbon nanotubes, fulerenes and boron nitride thin films.

4.1.1 One Step Photoemission

For x-ray photoemission to occur, incident x-rays on a crystal medium must have an energy, $\mathbb{E}_x$, greater than the binding energy, $\mathbb{E}_b$, of the electrons in the crystal. On incidence, electrons bound within the crystal absorb the incident energy equal to their binding energy and emerge from the crystal with a kinetic energy, $\mathbb{E}_k$, equal to the energy excess.

The detection process (see figure 4.1) almost works in reverse with the exception of x-ray production. The photoelectrons are first collected and focused. The electron kinetic energy is then filtered. Then a conductor of known work function kept at a positive bias,

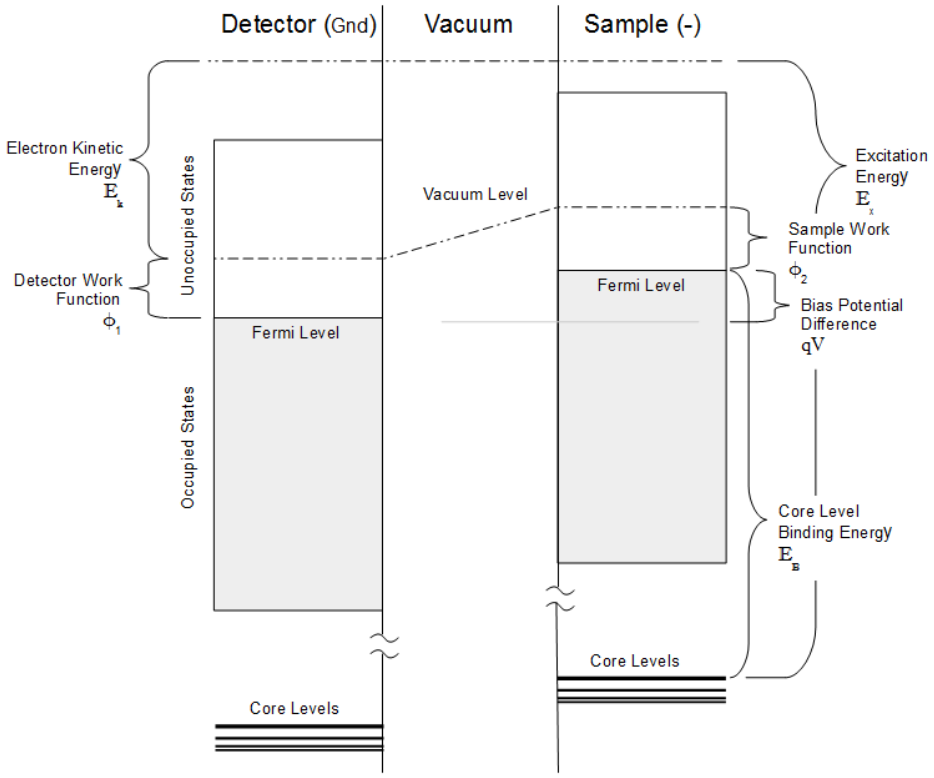

FIGURE 4.1: Energy diagram of the excitation and detection process

V, relative to the crystal absorbs the photoelectron current as a function of its kinetic energy. This in turn allows a calculation of the binding energy of the photoelectrons resulting from emission, i.e.,

$$\mathbb{E}_b = \mathbb{E}_x + qV - \phi_1 - \mathbb{E}_k \quad . \tag{4.1}$$

Here, ϕ_1, is the work function of the crystal and the quantity, qV, is the potential energy difference between the crystal and detector. The photoelectron spectral lineshape is, in the simplest sense, a Lorentzian distribution resulting from the decay rate of the core hole left behind (refer to figure 4.2). The Lorentzian width then gives the lifetime of the core hole from the energy-time uncertainty relation.

4.1.2 The Core Photoelectron Lineshape

The liberated photoelectrons do not emerge from the crystal unimpeded. Two main modes of inelastic scattering occur which modify the resulting photoelectron signal.

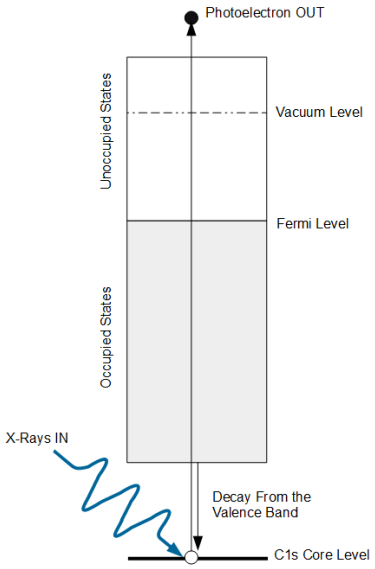

FIGURE 4.2: One step photo-emission.

These modes are generally classified into intrinsic and extrinsic scatterings. The extrinsic scattering is due photoelectron interactions with the positively charged nuclear cores. Consequently the accelerating photoelectrons lose energy to the production of Bremsstrahlung radiation (see figure 4.3). On the other hand, intrinsic scattering results from electron-electron interactions between the emerging photoelectrons and free conduction electrons at the Fermi level. This form of scattering is only prominent in metals where conduction electrons are abundant.

The loss of energy to Bremsstrahlung radiation is generally proportional to the fraction of lower-energy photoelectrons emerging from the crystal. This has been crudely modelled as a linear or step-like increase in the background signal. The more accurate description is based on the observation that the inelastic loss for a given energy is proportional to the relative fraction of higher energy electrons above that energy. This description of the Bremsstrahlung background is known as the Shirley background and takes the following form [65]:

$$I_{in}(\mathbb{E}) = B_o \int_{\mathbb{E}}^{\mathbb{E}_{max}} [I(\mathbb{E}') - I(\mathbb{E}_{max})] \; d\mathbb{E}' \tag{4.2}$$

Low-dimensional materials like graphene provide a very low nuclear cross-section for photoelectrons being emitted normal to the plane (see figure 4.4). And so, it is expected that the Shirley background contribution is a small fraction of the signal.

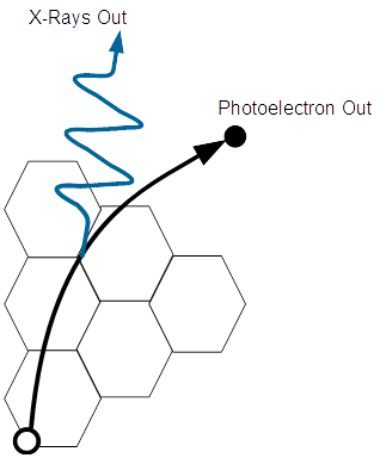

FIGURE 4.3: Production of Bremsstrahlung radiation. The scattering cross-section is only significant within the atomic plane

On the other hand, energy loss to conduction electrons through electron-electron interactions is certain for all core liberated photoelectrons in that these electrons must pass through the π bonding plane (again refer to figure 4.4). Since the lower energy photoelectrons are more susceptible to interactions, this type of scattering is then expected to enhance the signal on the low kinetic energy side of the peak core hole signal. In effect, the naturally pure Lorentzian line shape resulting from core hole decay acquires an asymmetric tail towards lower kinetic energies or equivalently higher binding energies. The magnitude of this effect can be quantified by an asymmetry parameter best described through the Doniach-Sunjic line shape [66][67], i.e.,

$$I_{ex} = cos[\frac{1}{2}\pi a + (1-a)atan([\mathbb{E}_o - \mathbb{E}]\Delta\mathbb{E}_L^{-1})][(\mathbb{E}_o - \mathbb{E})^2 + \Delta\mathbb{E}_L^2]^{\frac{1}{2}(a-1)} \tag{4.3}$$

which reduces to a Lorentzian line shape in the limit that $a = 1$ centred at an energy E_o, the core binding energy[1]. From here we can construct the net photoelectron signal,

$$I(\mathbb{E}) = I_{in}(\mathbb{E}) + I_{ex}(\mathbb{E}) \tag{4.4}$$

with $\mathbb{E}_o$ expected to be near 284.4eV for the C1s binding energy observed in pure graphite.

[1]In the original formulation of equation 4.3 it was assumed that the probability of bulk energy loss would be a function of film thickness, i.e., the probability would go to zero at zero thickness. Graphene then lies at this limit. A reformulation of this experssion was later done specifically for graphene, see specifically reference [67]

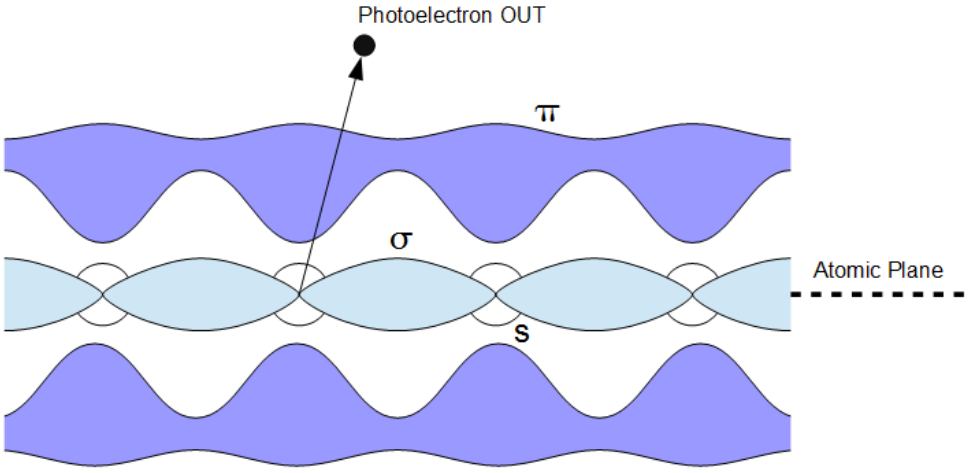

FIGURE 4.4: Inelastic scattering with the π conduction electrons. The scattering cross-section is large for electrons moving from the tightly bound 1s orbital normal to the atomic plane.

4.2 Near Edge X-Ray Absorption Fine Structure

4.2.1 Two-Step Photoemission

When the incident x-ray is near resonance with a core level, the photoelectron, rather than emerging from the crystal, is transitioned to an excited state near the Fermi level. It is near this point that the absorption of the incident x-rays sharply increases producing an absorption edge. Since the incident x-rays are not energetic enough to produce free photoelectrons, the consequent absorption is due to Auger electron production. The Auger process is a two step process where: 1) an incident x-ray, on resonance with a core electron, transitions that electron to an empty state near the Fermi level and, 2) the excited electron is then ejected from the crystal non-radiatively by absorbing the energy produced from a valence band decay of the core hole[2] (see figure 4.5) [68]. This ejected photoelectron is an Auger electron. In effect, this near edge x-ray absorption is entirely dependent on the number of empty sates above the Fermi level for a given excitation energy.

The simplest mode of x-ray absorption is absorption from resonance with a K-shell electron orbital[3]. For crystalline solids, this core electron will only transition to empty states above the Fermi level. For the transition to occur, the empty states must additionally be able to accommodate angular momenta, $l \pm 1$ of the initial core energy state. That is to say that the transitioned s-originating photoelectron will have p-like symmetry [70].

[2]This process is not strictly non-radiative. Some of the photoelectron energy can produce photons in addition to Auger electrons. The absorbtion probability is monitored by collecting Auger electrons as the core hole is filled.

[3]Absorption due to inner shells can be subject to effects such as line broadening from excitation of phonon modes [69].

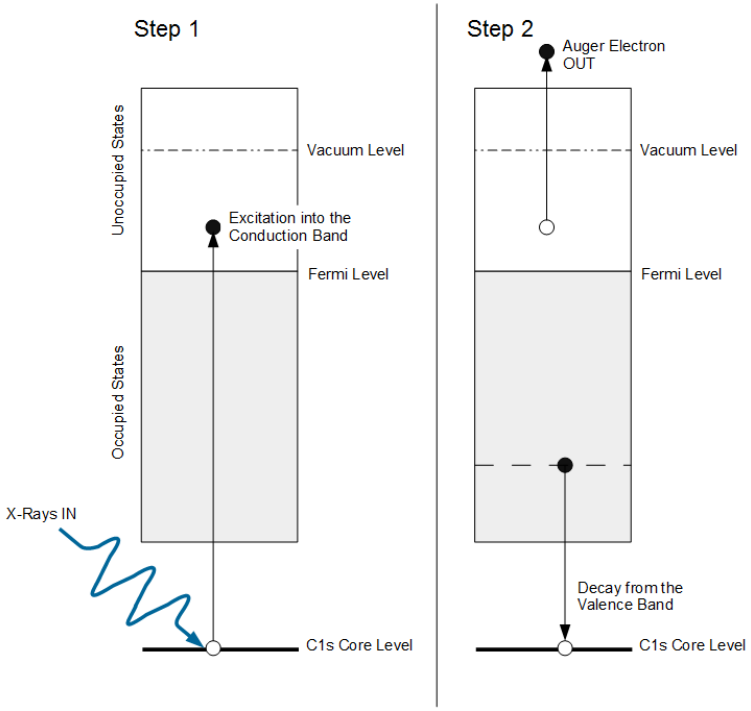

FIGURE 4.5: Two-step photoemission.

Impurities or adatoms which affect this symmetry will greatly affect the photoelectron transition rate. This effect will add to the absorption edge a fine structure dependent on the various bonding arrangements accessible to photoelectrons. From an alternate point of view, the change in absorption fine structure is due to the photoelectrons scattering off of impurities and adatoms while in the excited state [4].

The fine structure regarding adsorbed low-Z molecules is firstly decomposed into resonances with the π^* and σ^* bands. The π^* resonance is often distinguished as being the lowest energy structure of the absorption edge [16]. The σ^* resonance can then be identified when the polarization of the the incident x-rays is aligned with the bond axis, this is often parallel to the substrate plane for layered materials. The reverse is true for the π^* resonance when the polarization of the the incident x-rays is normal to the bond axis. Thus the net absorption will vary between π and σ symmetric transitions as [71],

$$I(\theta) = I_\sigma sin^2(\theta) + I_\pi cos^2(\theta) \tag{4.5}$$

This assumes that p-orbitals tend to align somewhat normal to the bond axis and adjusting the incident polarization can be used to optimize either the π^* or σ^* signals [72].

[4] Indeed, Near Edge X-Ray Absorption Fine Structure (NEXAFS) is of necessity described by multiple scattering theory [16].

Indeed, for low-dimensional materials, observing this change in photoelectron intensity as a function of polarization angle helps distinguish that material from its substrate.

In simple gasses such as argon, the K-shell photoelectrons first enter empty Rydberg states for energies below the ionization potential [73]. In this case, these transitions are seen as a series of peaks increasing in number asymptotically towards the ionization potential. Equivalently for crystals, K-shell photoelectrons will first transition to conduction band empty states near the Fermi level. This resonance is the π^* resonance and for insulating materials the transition will not occur until the excitation energy is above the band gap energy. At higher excitation energies, photoelectrons transition into the vacuum where there is a continuum of empty states. At these energies the x-ray absorption is expected to increase abruptly producing a step-like absorption edge [74]. In the continuum regime, for energies greater than the work function of the material, σ^* resonances are often accessible. Other resonances and features in this regime can be attributed to trapping of the photoelectrons by the centrifugal portion of existing molecular potentials or step-like increases due to multi-electron excitations [74].

4.2.2 Near Edge Resonance Lineshapes

The photoelectron is not measured directly since, in theory, it recombines with its hole. The resulting energy from recombination is transferred to a valence band electron which is then ejected from the crystal, and it is this Auger electron which is measured. Therefore, the resulting lineshape should reflect the lifetime of the photoelectron in the excited state. Indeed, the higher the energy of the final excited state, the shorter the lifetime which implies higher energy resonances will have broader lineshapes [74]. In general the near-absorption lineshapes are described by a Voigt distribution[5],

$$I(\mathbb{E}) = \int_{\mathbb{E}} G(\mathbb{E}-\mathbb{E}')L(\mathbb{E}'-\mathbb{E}_o)\ d\mathbb{E}' \qquad \text{where} \tag{4.6}$$

$$G(\mathbb{E}-\mathbb{E}') = exp[-\frac{1}{2}(\mathbb{E}-\mathbb{E}')^2(\Delta\mathbb{E}_G)^{-2}] \qquad \text{and} \tag{4.7}$$

$$L(\mathbb{E}'-\mathbb{E}_o) = [(\mathbb{E}'-\mathbb{E}_o)^2 + \Delta\mathbb{E}_L^2]^{-1} \tag{4.8}$$

[5]Normalization factors in equations 4.6 through 4.8 have been taken to be unity for simplicity. These factors are experimentally determined though data reduction.

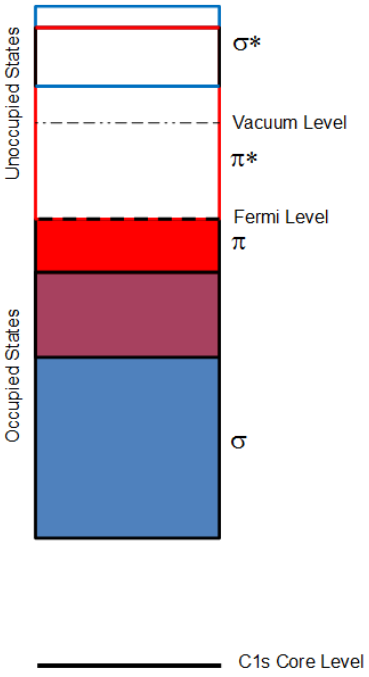

FIGURE 4.6: An approxiamte energy level visualization of graphene derived from reference [2].

Here, G and L represent a Gaussian and Lorentzian distribution, respectively.

In particular, the σ^* molecular orbital, which is formed from the degeneracy breaking of the neighbouring atomic states (refer to fig.2.1), is at an energy high enough for electrons to scatter from those neighbouring atoms. This is to say that electrons in the σ^* state above the vacuum level are quasi-bound. This leads to two broadening mechanisms. The first results from any change in the inter-atomic distance. Here, the energy of σ^* will decrease linearly with increasing inter-atomic distance[6] [75]. This implies that any existing bond length distribution should then broaden the σ^* lineshape[7] [77]. The second, results from the quasi-bound electrons tunnelling into the vacuum. This will weight the distribution of σ^* electrons towards lower energies in so much that higher energy electrons are more likely to tunnel into the vacuum. The effect is a tailing of the lineshape towards higher energies [76]. This has been described empirically by modifying the Gaussian width to be linearly dependent on energy [77], i.e.,

$$\Delta\mathbb{E}_G \rightarrow m\mathbb{E} + b \tag{4.9}$$

[6]The work of Sette et al., determined this result empirically [75].

[7]The work of Arvanitis et al., demonstrated that the natural C-C bond stretching frequencies in adsorbed C_2H_n molecules produces a broadening of less than 2eV [76].

At the Fermi level or the conduction band minimum (for either metals or insulators) the density of empty energy states abruptly increases following the Fermi-Dirac distribution. Due to energy-momentum restrictions, π-like symmetric transitions near this point are preferred forming the π^* resonance. Similarly, at the vacuum level the density of empty energy states again increases abruptly representing the continuum of energy states throughout the vacuum. For a particular energy, electronic transitions that carry σ-like symmetry are enhanced forming the σ^* resonance. Most notably, however, it is the continuum of vacuum energy states which produce a step or edge-like feature in the absorption. This absorption edge is as abrupt in energy as the crystal potential maximum where the sharpness in the edge is naturally lifetime limited due to decay. Therefore a convolution of the near edge resonance lineshape (equation 4.6) with a step distribution provides the best physical interpretation of the vacuum level edge-like feature, namely,

$$I_B = \int_{\mathbb{E}} I(\mathbb{E}') \ d\mathbb{E}' \tag{4.10}$$

In the limit of low noise measurements, where the signal is lifetime limited the vacuum adsorption edge takes the form of a Lorentzian convolution [78],

$$I_B = \frac{1}{2} - \frac{1}{\pi}\arctan[\frac{1}{2}(\mathbb{E} - \mathbb{E}_o)(\Delta\mathbb{E}_L)^{-1}]. \tag{4.11}$$

When the measurement is limited by instrumental noise, the edge is instead a Gaussian convolution [77],

$$I_B = \frac{1}{2} + \frac{1}{2}\mathrm{erf}[\frac{1}{2}(\mathbb{E} - \mathbb{E}_o)(\Delta\mathbb{E}_G)^{-1}]. \tag{4.12}$$

At this point, two x-ray excitation processes have been discussed, one involving photoelectron release and the other involving Auger electron release. The two processes are similar in that a photoelectron and core hole are created. This core hole, in the case of absorption, is electrostatically coupled to the photoelectron. In fact, for low energy near Fermi level excitations the coupling is strong enough to form an excitonic-like state. The state arises from core hole screening by conduction electrons and is specific to metals. This is to say that, in the limit where the reduced mass of the exciton is very small

the exciton binding energy goes to zero[8]. This means that any resulting Rydberg-like states are so closely spaced that a single resonance is produced. The corresponding density of states has been described by a power law which is singular at the Fermi level [79][80]. This acts to enhance the continuum of conduction states above the Fermi level by adding to it this Rydberg-like continuum. This is observed in two ways. Firstly, this joint density of states near the Fermi level increases the probability for escaping photoelectrons to lose energy to electrons near that level, as mentioned earlier in section 4.1.2. Secondly, the absorption cross section will be enhanced for transitions near the Fermi level due to this joint density of states between the conduction band and the core hole exciton [80][81].

4.3 Measuring Photoelectrons: The X-Ray Photoelectron Spectrometer

It is paramount, prior to any measurement, to clearly understand the origin and limitations of the accuracy and precision of that measurement. The x-ray photoelectron spectrometer, used to measure the generated free electrons, comprises an x-ray source, a sample staging chamber and photoelectron spectrometer. Each component adds error to the measurement and can be accounted for to some degree. The x-ray source has traditionally been an x-ray tube which generates spectrally broad x-rays through electron bombarding a metal target. The bombarding electrons have enough energy to excite K-shell core electron states, the decay of which produces, for example, K^{α} x-rays. These x-rays can be collimated using spatial filters and directed at a sample. The emitted photoelectrons are then collected and focused with an electrostatic lens. The resulting image is then discriminated according to the electron's energy and momentum.

4.3.1 X-Ray Production: The Synchrotron Light Source

The modern x-ray photoelectron spectrometer uses a synchrotron light source as opposed to the, still used, x-ray tube. By comparison the spectral line width superior. Here, electrons are accelerated in a ring at relativistic speeds. At these speeds the electrons lose energy through radiation. Orbiting electrons with kinetic energy on the order of 1GeV will radiate photons on the order of more that 100eV [69].

The electrons in the ring will exist with some distribution of velocities which thereby places a distribution on the energy of the radiation emitted. The band width of the

[8]Consider graphene where the hole mass, being localized to an atom, is infinite [79] and the carrier mass is zero

emitted radiation can be narrowed by constructively interfering the radiation of electrons with similar accelerations. This is accomplished by undulating the trajectory of the electrons in the ring at a fixed spatial frequency. A set of magnets held close to the accelerating electrons with an alternating polarity causing them to take on a nearly sinusoidal trajectory. Assuming that the resulting trajectory is planar and sinusoidal, radiation at the high acceleration points will constructively interfere to yield a narrow band of x-rays. Due to the sinusoidal nature of the trajectory the radiated light has a select set of frequencies with maximal intensity.

Much in the same way a laser can output higher order spatial modes of light distribution of varying symmetry so too does the radiated light from undulation. To select out a "zeroth order mode" a pinhole type spatial filter is used. The output intensity distribution in energy is Gaussian-like but not actually so[9] and it is up to the discretion of the experimenter to determine the intensity profile used. To further narrow the band width of the resultant light, the x-rays are collimated onto a grating. The diffracted x-rays are then band width limited by an adjustable slit. The monochromated x-rays are then focused to a spot on the sample[10].

4.3.2 The Hemispherical Energy Analyser

Early uses of the hemispherical energy analyser involved measuring electron beam absorption [82] and scattering through gases, [83] measuring proton binding energies [84] and measuring photoelectron energies of molecular hydrogen and oxygen [85] the theoretical basis of which had been described much earlier by Hughes [86] and Purcell [87]. By 1970 the hemispherical analyser was employed to measure electron binding energies as a function of angle [88][89][90]. A modern version of the hemispherical analyser was developed over the next five years [3]. The modern version is preferred over the plane mirror analyser and the cylindrical analyser for its greater electron throughput and circular stigmatic focusing [87][82][90]. Mainly, the hemispherical analyser allows a higher electron transmission and energy resolution for its overall size and will easily achieve a resolution of 0.5 eV with standard machining and placement tolerances of 0.025 mm. This is with respect to a hemisphere diameter on the order of 250 mm[11] [91].

Free electrons originating from a point subject to a radial, r^{-2}, field can be focused to a point forming an axis from that stigmatic pair [92]. The resulting energy dispersion

[9] The "modes" of the radiated x-rays are non-trivial, e.g., they cannot be derived from the paraxial equation

[10] The Australian Synchrotron Soft x-ray beam line produces a $\approx 400\mu$m spot.

[11] The first analysers made appear to be quite small. The work by Simpson states a mean radius of 2.5cm! See reference [82]. Larger diameter hemispheres are less a subject to common millimetre scale work function variations in the hemisphere surfaces.

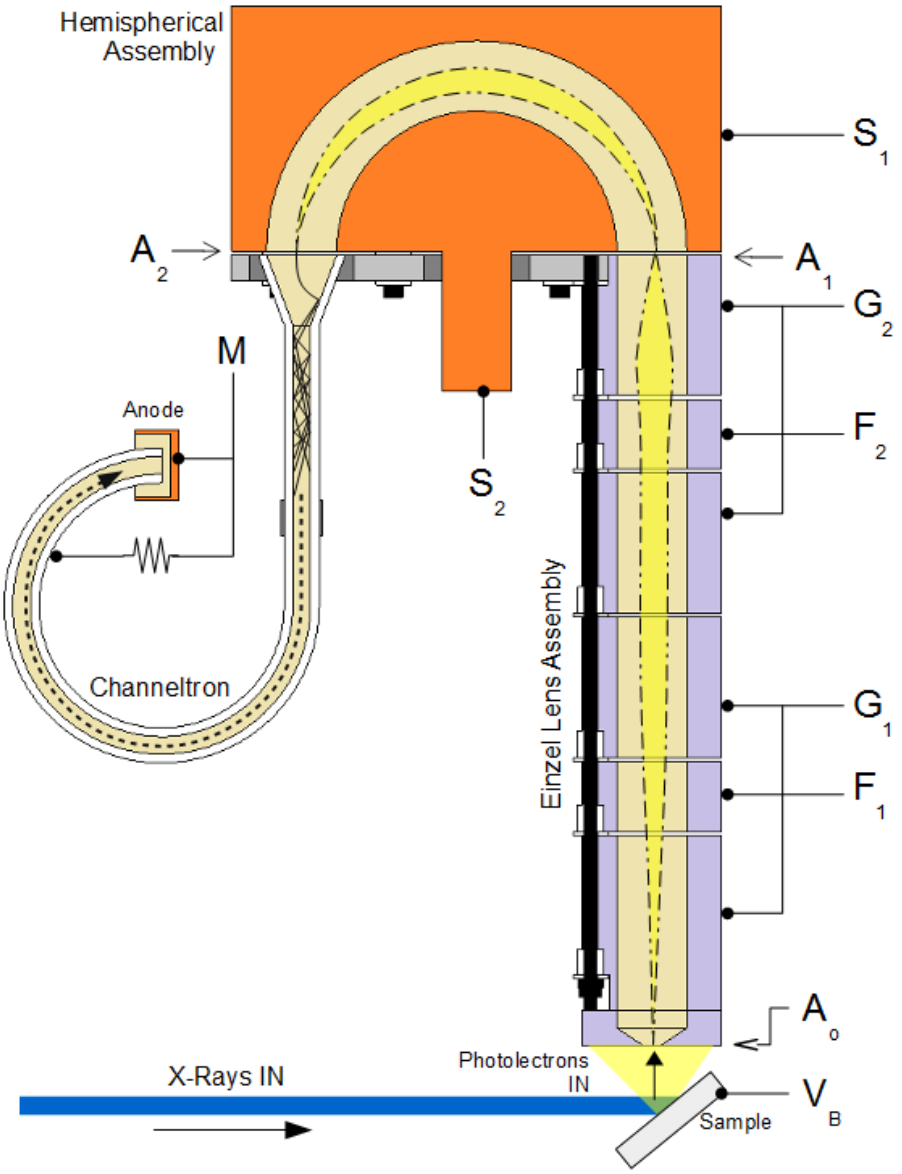

FIGURE 4.7: Diagram of a simplified hemispherical energy analyzer. The design presented here, created by the author, was derived mainly from references [3] and [4], and has been cost minimized (excluding the channeltron). The channeltron depicted, based on a 1/4" glass tube which measures 3 times a commercial channeltron, has been enlarged for clarity. X-Ray generated photoelectrons are liberated from the sample with help by a potential bias, V_B. The dotted lines trace the path of photoelectrons through the detector starting at the entrance aperture, A_o. Apertures, A_1 and A_2 then direct electrons into and out of the hemispherical deflector, respectively. Photoelectrons first pass through the the Einzel lens assembly held at potentials G_1, F_1, G_2 and F_2. Potentials F_1 and F_2 are used for focusing while the ratio of G_1 to G_2 determines the photoelectron kinetic energy loss prior to entering the deflector [4]. The deflector, energy segregates the electron flux with a radial electric field set by potentials S_1 and S_2 where S_1 in the simplest arrangement is at ground. On exiting, the deflector electrons are accelerated to the channeltron walls by a potential, M, creating a electron cascade which amplifies the photoelectron current that is finally measured.

along that axis is then proportional to the product of the mean trajectory radius with the square of the opening angle of the originating electron beam [87]. The electron beam is, of course, formed from photoelectrons emanating from the sample. The photoelectrons emerge from the sample surface in all directions and must be focused to a point so that points of a given energy in the dispersed image are distinguishable. An electrostatic Einzel lens is typically used for focusing which fixes the opening angle of the resulting beam prior to entering the radial field (see figure 4.7). This beam emerges from a slit which is then dispersed in the field. Here, the construction of the analyser and mathematical description of the resulting instrumental broadening in the image due to a finite beam width and imperfect focussing is greatly simplified by extending the field to a hemispherical volume. Further confining the field to a shell volume permits work function variations, existing in either the anode or cathode of the field, to be averaged out.

With focusing in the hemispherical configuration alone, aberration due to space charge effects is significant. Space charge, which is the mutual Coulombic repulsion of the electrons, effects the throughput of an electron beam within the analyser. The throughput is inversely proportional to the square root of the electron kinetic energy in the limit of perfect focusing where the resolving power, defined as $\Delta\mathbb{E}/\mathbb{E}$, is much less than one[12]. This relationship breaks down at very low energies where the resolving power is on the order of unity which implies that, for a given analyser geometry, there is an optimum throughput energy. Therefore, it is ideal to decelerate high kinetic energy electrons (a character common to all core level photoelectrons) to this optimal throughput energy prior to entry in the analyser. In doing so, other effects due to stray or unused electrons produced through either discrimination or collision with the analyser itself are minimized [82].

As with all cylindrical electrostatic optics, aberration due to non-linear refraction of electron trajectories away from the optical axis are prevalent [92]. Steps can be taken in the analyser design to minimize spherical and chromatic aberration such as incorporating fringe field control electrodes [93] and optimising the filling factor of each lens element [94]. Truly minimizing spherical or chromatic aberrations and other fringing effects can only be accomplished by modelling the analyser which involves numerically solving Poison's equation over the geometry in question. Having that in mind, much work has been done with regard to simplifying that problem by modelling lenses with first-order matrix representations [95][96][97][98][99], however, the problem of analyser optimization continues and most of the recent work in analyser design has relied on advances in computer processing speed to solve exactly for analyser potentials and the resulting electron trajectories [100][101][102][103][104][4].

[12]The theoretical resolving power of the hemispherical analyser is on the order 1E-3 in energy [83][91].

4.4 X-Ray Photoelectron Spectroscopy and Absorption in Graphene

4.4.1 X-Ray Photoemission of Carbon

X-ray photoelectron spectroscopy is generally a surface sensitive measurement since the mean free path for inelastic collisions of photoelectrons is on the order of 10 to 20 Å. In turn, any ambient substances not accounted for that can react with the surface can erroneously effect the measurement. For this reason, the study of a substance requires that it must initially be isolated from the environment. This is easily achieved in an ultrahigh vacuum environment at pressures near 10^{-10} Torr or lower where exposure of the surface to a single Langmuir can take up to three hours. One Langmuir corresponds roughly to the flux needed to adsorb one monolayer with a sticking coefficient of unity[13]. Here in this environment, it has been widely noted that thin films of carbonaceous material, usually hydrocarbons from handling and operation of the instrumentation, tend to form on surfaces over time[14] [69]. Indeed for this apparent ubiquity, the carbon 1s photoelectron signal has historically been used for spectrographic energy calibration [69].

Carbon is the most versatile of all elements in that it defines that which is organic and so, the C 1s core level has been extensively examined [69]. The most general form of carbon is amorphous carbon, which is composed *mostly* of a carbon that does not have any crystalline structure and is free from functional groups. The carbon-carbon bonding arrangement is mainly a mixture of sp^3 and sp^2 hybridization with some much lesser fraction due to an sp hybrid [105]. When prepared by a filtered cathodic vacuum arc technique [106], pulsed laser deposition [107] or through plasma decomposition [108][109] varying, sometimes controllable, ratios of sp^2 to sp^3 bonding can be achieved.

As one should expect, the features in the photoelectron and x-ray absorption spectra of amorphous carbon, while similar to the features in crystalline carbon, are much more broad in comparison representing a distribution of carbon arrangements [105]. For example, amorphous carbon derived from plasma decomposed C_{60} has been studied [109]. Here the width of the C 1s C_{60} peak (0.8 eV) was found to be less than half that of the amorphous carbon peak (1.8 eV) where the difference is an indicator to the fraction of C_{60} remaining. On this point, the broadness appears to be an indicator of disorder

[13] 'The **langmuir** (symbol: **L**) is a unit of exposure (or dosage) to a surface (e.g. of a crystal) and is used in ultra-high vacuum (UHV) surface physics to study the adsorption of gases. It is a practical unit, and is not dimensionally homogeneous, and so is only used in this one field. It is named after American physicist Irving Langmuir.' Wikipedia c.2016

[14] This time scale is on the order of weeks for modern systems that use all metal seals and oil-free vacuum pumps.

[110]. However, precise quantification of the type of disorder through deconvolution of the carbon 1s lineshape has been considered more difficult due to the number of allotropic possibilities to which any one photoelectron producing constituent can refer to and as a result, an analysis is sometimes ignored altogether [111]. The difficulty in deconvolving the C 1s lineshape is not solely a condition of carbon's allotropes, many of these allotropes are metallic, and the resulting asymmetry of the C 1s lineshape (see section 4.2.2) significantly adds to this impalpability.

4.4.2 The Graphene Core Level

While many different forms of carbon have been investigated through x-ray photoelectron spectroscopy, a review of all these works is unnecessary and beyond the purpose of this section. The C 1s lineshape is convoluted and therefore a proper understanding of its linshape requires initially focusing on the simplest system. Graphene, with its two-dimensional electronic structure, is used as the building block to describe so many other substances and is the main focus of this section. Since it exists as a metal with a simple π and σ bonding arrangement forming massless charge carries at the Fermi level (refer to section 2.2), its C 1s lineshape is asymmetric with a tail toward higher binding energy. This asymmetry represents significant coupling between the conduction electrons and the core photo-hole. This coupling, and with it the asymmetric lineshape, are expected to not be directly related to disorder, and it has been suggested that more experimentation is needed to understand any relationship if present [67].

In the presence of lattice vacancies, as the material becomes more chemically reactive, the C 1s core level signal is expected to yeild components grouped around lower binding energies [112]. In contrast, dopant-based defects which are expected to tightly bind to the carbon have the effect of passivating the material's surface leading to a binding energy increase. For example, in the case of graphene oxide, carbon-oxygen bonds are quite strong, being on the order of an electron volt or greater [5][113][114]. This is also the case with carbon-nitrogen bonds [115][116] and the hydrogenation of single-walled carbon nanotubes [117]. However, boron adsorbed to the graphene surface and nickel acting as a substrate has the effect of lowering the binding energy by the same order [118][119].

There have been many attempts to deconvolve the C 1s lineshape in the presence of disorder. Experiments involving graphene oxide provide many examples. In these works graphene oxide is created from graphite and then graphene is recovered through reduction. In the reduced material the lower kinetic energy tail is often interpreted as a series of symmetric decay modes occurring at energies corresponding to different carbon

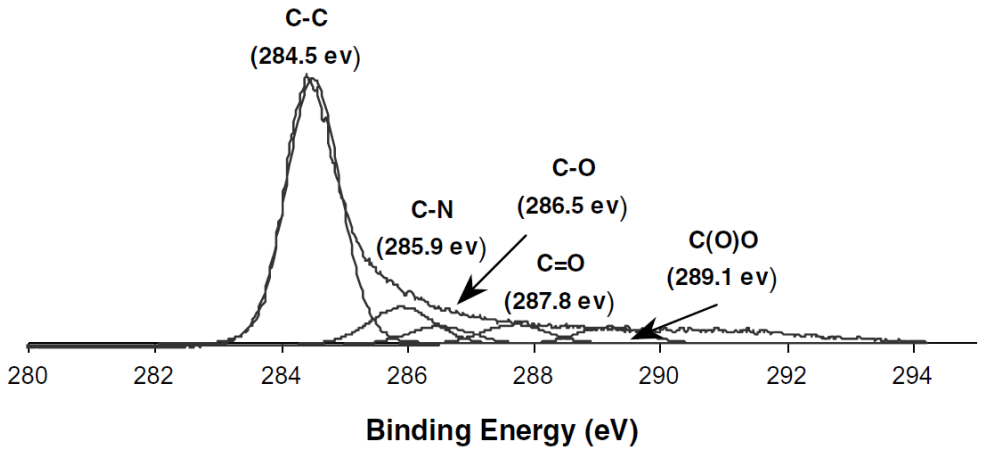

FIGURE 4.8: C1s spectrum of reduced graphene oxide [5]

bondings [5] [115][116] [113]. This is highly questionable since the pristine lineshape is already expected to show the asymmetric tail to higher binding energy, due to interaction of the photoelectron with the metallic graphene electrons. Consider figure 4.8 [5]. The measured line shape shows no apparent maxima in the high energy tail. Still the authors take the liberty to decompose the curve into a series of apparently pure decay modes[15]. A similar analysis produced figures 4.9 [6] and 4.10 [7]. At least in these analyses a Voigt distribution is used and, there are apparent maxima in the data. The Gaussian component of the Voigt distribution would account for experimental broadening, however, in reference [6], the authors neglect to mention what that broadening might be. In reference [7] the broadening is placed between 400 meV to 700 meV which is quite large for a synchrotron based light source.

Annealed hydrogenated single-walled carbon nanotubes display broader C 1s lineshapes after consecutive hydrogenation and annealing which was interpreted as increased disorder [117]. Occasionally investigators acknowledge the asymmetry resulting from inelastic Fermi-photoelectron collisions in graphene [120] [121] [122][123] [124] [125][126]. This observation leaves these and other works [127] [128] [129][7][6] to be reinterpreted since the asymmetry parameter alone can account for a significant fraction of the features claimed to be measured in data (see figures 4.8, 4.9 and 4.10)[16].

4.4.3 X-Ray Absorption Fine Structure in Carbons

Amorphous carbon, while very ambiguous in analysis of the C 1s lineshape when compared to pure carbon, often shows fine structure in x-ray absorption. Namely, in addition

[15]The actual lineshape used is never mentioned.

[16]This is a key point in analysis. This is to say that the Shirley background of graphene, as describe in section 4.1.2, should be very small in the resulting fit

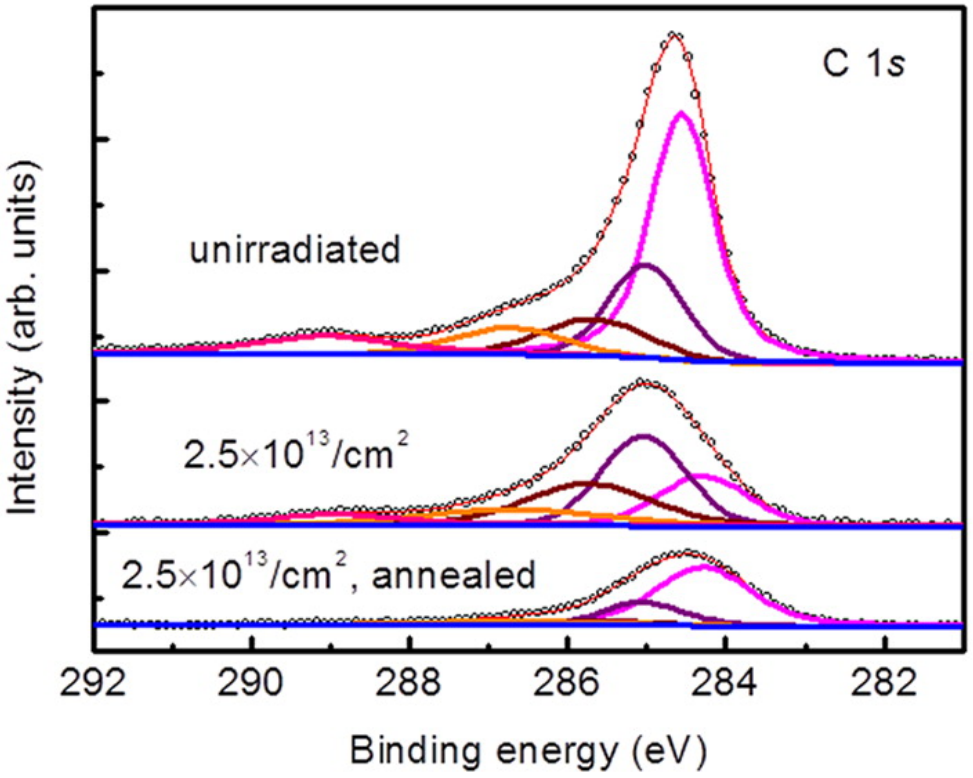

FIGURE 4.9: C1s spectrum of CVD graphene exposed to PMMA [6]

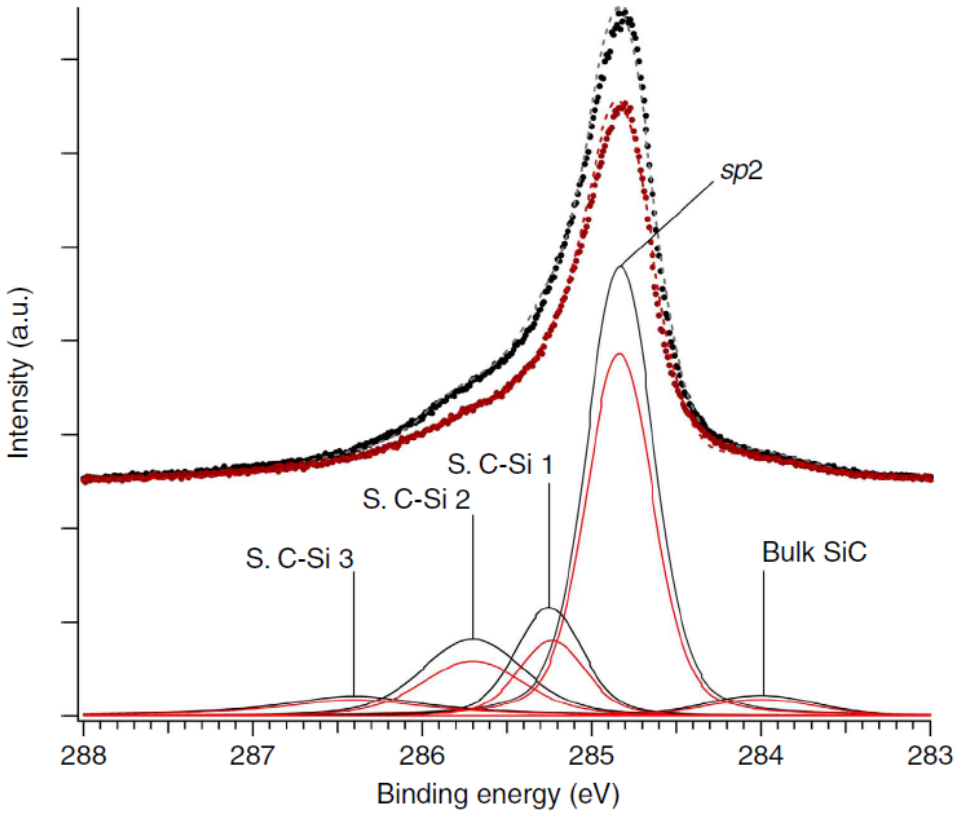

FIGURE 4.10: C1s spectrum of epitaxial graphene [7]

TABLE 4.1: C1s XPS Reference Data for Pristine and Chemically Modified Graphene

Material	Binding Energy	Assignment	Literature Reference #
CVD Graphene	284.6	C-C	[6]
	285.0	C-C(H)	
	285.7	C-C=O	
	286.7	C-O-C(H)	
	289.0	O-C=O	
CVD Graphene + N	284.8	C-C	[115]
	285.8	N-sp2 C	
	287.5	N-sp3 C	
CVD Graphene + N	284.6	C-C	[116]
	285.8	C-N	
	288.2	C-O	
CVD Graphene + Ni	285.0	C-Ni	[118]
	284.88	C-Ni	
	283.6	C-Ni	
CVD Graphene + Ni,B	284.31	C-B	[119]
	283.34	C-2B	
	282.27	C-3B	
Epitaxial Graphene	284.8	C-C	[7]
	285.77	C-Si	
Epitaxial Graphene	284.5	C-C	[114]
	286.3	C-O	
	283.7	C-Si	
Graphene Oxide	284.5	C-C	[5]
	286.5	C-O	
	287.8	C=O	
	289.1	C(O)O	
Graphene Oxide	284.5	C-C	[113]
	285	C-H	
Carbon Nanotubes + H	284.75	C-C	[117]
	285.5	C-H	

to π^* and σ^* resonances at 285 eV and 293 eV respectively[17], there is a mid band resonance near 288 eV (see figure 4.11) [9][8]. This resonance lies very close to the graphene vacuum level and has also been seen in C_{60} [109][131] and is expected in C_{60}-like structures [9]. Structure originating below the vacuum level is considered to be π-like [74] which has generally been confirmed from observations of the fine structure of graphite and diamond [108][130]. Diamond is an entirely sp^3 type material and its absorption edge which begins just above this energy is entirely due to σ^* type resonances which suggests that the mid band feature is of a π^* origin [132].

The work of Comelli et al. (1998) [108], which in the context of amorphous carbon presents data of adsorbed benzene and cyclohexane that suggests the mid band feature is some residual carbon-hydrogen bonding. This conclusion stems from a previous analysis

[17]The symmetry of the resonances was confirmed by Rosenberg et al. (1986) [130].

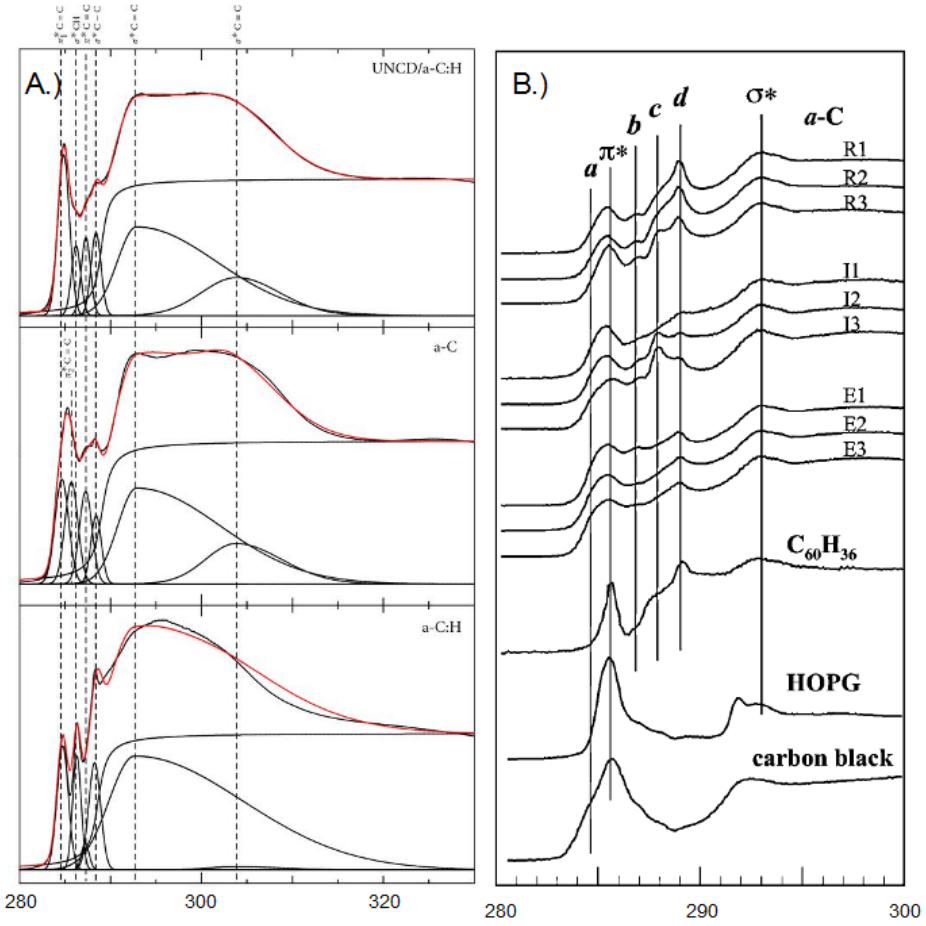

FIGURE 4.11: a.) Figures 1a through 1c of reference [8]. B.) Figure 1 from reference [9].

of solid phase and absorbed saturated polymeric molecules which lack π bonding [77] [133]. In the context of such molecules adsorbed to a surface, the contribution of Rydberg states to this feature, in its nearness to the ionization potential, was assumed to be zero due to the large spatial extent of those states relative to the valence states[18]. This leaves the mid band feature to be a result of transitions to valence final states which, in that context, are hydrogen saturated. For unsaturated hydrocarbons the valence states merge into a molecular π state that is degenerate with other such molecules. Degeneracy breaking of the π^* state would then result in multiple π-like resonances, namely, two π^* resonances to first order [74].

In graphite, the mid band feature has been suggested to be due to interlayer states having a mixture of π or σ-like symmetry[19] [132]. Similar mid band fine structure also exists in layered hexagonal boron nitride seen in the K edge of both boron and nitrogen [71]. Together, boron and nitrogen parenthesize carbon on the periodic table and so, the boron-nitrogen bond is expected to be isoelectronic with the carbon-carbon bond

[18]The radial extent of Rydberg orbitals relative to the ionic radius of the atom or molecule is large and is therefore expected to overlap with the surface upon absorption.

[19]These states are conceived as a mixture of px, py and pz orbitals.

of graphene [134]. Here the observed mid band feature lies closer to the π^* resonance for both K edges which seems to correlate with the lower work function of the material (approximately 3 eV in BN as opposed to 4.6 eV in graphene) and is deduced to have p_z-like symmetry. An ion implantation and bombardment experiment on hexagonal boron nitride by Jimenez et al. (1996) [135], observed three additional π-like peaks below the vacuum level . The peaks were produced by both ion bombardment and ion implantation. Here, a peak lying at the vacuum level increased dramatically with both bombardment and implantation while the peak closest to the characteristic π^* edge resonance only increased as dramatically as the vacuum level feature did after implantation. The third peak, being just above the noise level and located between these two, was observed after both bombardment and implantation but consistently remained at a low intensity. A later work on bilayer hexagonal boron nitride by Shimoyama et al. (2004) [134], argues that the peak nearest to the characteristic π^* edge resonance is a result of hybridization with the nickel substrate. To add to all this, this mid band feature has been shown to be enhanced by oxygenation in both carbon and boron nitride nanotubes [136][137].

Again, splitting of the π^* resonance is expected when the π states are in close proximity with neighbouring π states to first order. Further minimizing that proximity to include second order effects would only act to move the resultant π^* pair to higher energies [74]. With this in mind, Shimoyama's argument is quite strong and, in the context of graphene, is further supported by theoretical calculations [2]. This still does not totally explain the mid band feature at the vacuum level which appears to have an intensity directly proportional to the amount of impurities in the system and is common to layered materials.

TABLE 4.2: NEXAFS Reference Data for Pristine Graphene and Related Carbon Materials

Material	Resonance Energy	Assignment	Literature Reference #
Amorphous Carbon	285.5	π^*	[9]
	293	σ^*	
	284.5	(a) sp2	
	287	(b) unknown	
	288	(c) sp2-C(I)	
	289	(d) sp2-C(II, III)	
Amorphous Carbon	285	π^*	[108]
Carbon Black	285.5	π^*	[9]
C_{60}, C_{70}	285.35	π^*	[131]
Graphite	285.5	π_o	[130]
	292.5	$\sigma_{1,2}$	
Graphite	285	π^*	[132]
	289	Interlayer	
	292	σ^*	
Graphene	283.7	Doping	[138]
	285.5	π^*	
	288	Interlayer	
	291.5	σ^*	

Chapter 5

Formation and Analysis of Graphene Vacancies via XPS and NEXAFS Measurements

High resolution x-ray photoelectron spectroscopy (XPS) and near edge x-ray absorption fine structure spectroscopy (NEXAFS) were used to determine the character of vacancy defects in graphene. Vacancies were induced in graphene on a thermally oxidized silicon substrate using argon ion bombardment. XPS of the carbon 1s core level of pristine graphene shows a C 1s spectrum consistent with a single C 1s peak broadened both instrumentally and by a Doniach-Sunjic type effect. As defects are created, deconvolution of the resulting spectrum reveals two peaks. The first retains the same spectral width as that of the pristine graphene but with a reduced intensity. The second peak, which is broader and at a slightly higher binding energy (200 meV), increases in intensity with increasing defect concentration. This second peak is identified as the experimental XPS signature of defective graphene. The observation is somewhat at odds with theoretical calculations of XPS spectra for graphene with various vacancy arrangments, which generally produce C 1s peaks shifted to lower binding energy. Instead, the emergence of this second peak, together with the emergence of a single sharp resonance seen near the vacuum level in the NEXAFS spectra, is interpreted as a distribution of molecular-like states forming on the grapahene surface.

5.1 Introduction

Defects limit the electrical conductivity through a material. Understanding the physics of defects is therefore essential to building materials and structures with novel electronic

properties. Low dimensional materials, because they are simple, act as a foundation for understanding higher dimensional systems by allowing the exploration of more advanced theory.

Graphene is the archetypal two dimensional crystal and has been the foundation for understanding carbon based systems. The first measurements of graphene's carrier mobility at room temperature were in excess of 15,000 cm^2 V^{-1} s^{-1} [20], which is an order of magnitude greater than is expected for many metals [21]. This carrier mobility is practically independent of temperature between 10 K and 100 K [22][23][24]. This indicates that the dominant scattering mechanism is due to defects. For graphene adhered to a SiO_2 substrate the mobility is limited by defects in the form of charged impurities from the substrate [25] [26] and so, one finds that the mobility can be greater by an order of magnitude from simply using a more chemically inert substrate such as hexagonal boron nitride [27] [28].

Many different forms of carbon have been investigated through XPS and NEXAFS. The existing large body of work on carbon is a result of carbon's versatility and as a result the C 1s core level, with a binding energy of about 284.5 eV, has been extensively examined [69]. The most general form of carbon is amorphous carbon composed *mostly* of a carbon without any crystalline structure and free from functional groups. The carbon-carbon bonding arrangement will mainly be a mixture of sp^3 and sp^2 hybridization with some much lesser fraction due to an sp hybrid [105]. When prepared by a filtered cathodic vacuum arc technique [106], pulsed laser deposition [107] or through plasma decomposition [108][109] varying, sometimes controllable ratios of sp^2 to sp^3 bonding can be achieved.

As one should expect, the features in the XPS and NEXAFS of amorphous carbon, while similar to the features in crystalline carbon, are much broader representing a distribution of carbon arrangements [105]. For example, amorphous carbon derived from plasma decomposed C_{60} has been studied [109]. Here the width of the C 1s C_{60} peak (0.8 eV) was found to be less than half that of the amorphous carbon peak (1.8 eV) where the difference is an indicator to the fraction of C_{60} remaining. On this point, the broadness appears to be an indicator of disorder [110]. However, precise quantification of the type of disorder through deconvolution of the carbon 1s lineshape has been considered too difficult due to the number of allotropic possibilities to which any one photoelectron producing constituent can refer and as a result, an analysis is sometimes ignored altogether [111].

The pristine C 1s lineshape is modified by four main factors, chemical coordination, extrinsic scattering, intrinsic scattering and instrumental broadening. For pristine graphene, being a two-dimensional semi-metal with carbon situated high on the periodic table, it

has a simple planar π and σ bonding arrangement. This two dimensionality provides a low scattering cross section for photoelectrons and thus, for graphene, extrinsic scattering should be a minimum. This leaves the main broadening mechanisms of the C 1s to result from intrinsic scattering and instrumental broadening. The main intrinsic scattering mechanism for graphene is electron-electron coupling of photoelectrons with the conduction band. These inelastic collisions are more likely for slower moving photoelectrons which has the effect of producing an asymmetric lower kinetic energy (or higher binding energy) tail on the otherwise symmetric Lorentzian lineshape. This is a Diniach-Sunjic type effect true for many metals [66] and specifically graphene [67]. Consequently, since the instrumental broadening can be measured directly it should be possible to quantitatively account for changes in the chemical coordination through the introduction of disorder.

There have been many attempts to deconvolve the C 1s lineshape in the presence of disorder. Experiments involving graphene oxide provide many examples. In these works graphene oxide is created from graphite and then graphene is recovered through reduction. In the reduced material the lower kinetic energy tail is often only interpreted as a series of pure decay modes occurring at energies corresponding to different carbon bondings [5] [115][116] [113]. This is highly questionable since the pristine lineshape is already expected to show the asymmetric tail to higher binding energy. Consider again figure 4.8. The measured line shape shows no apparent maxima in the high energy tail. Still the authors take the liberty to decompose the curve into a series of apparently pure decay modes[1]. A similar analysis was done in references [6] and [7]. At least in these analyses a Voigt distribution is used and, there are apparent maxima in the data. The Gaussian component of the Voigt distribution would account for experimental broadening, however, in reference [6], the authors neglect to mention what that broadening might be. In reference [7] the broadening is placed between 400 meV to 700 meV which is quite large for a synchrotron based light source.

Annealed hydrogenated single-walled carbon nanotubes display broader C 1s lineshapes after consecutive hydrogenation and annealing which was interpreted as increased disorder [117]. Occasionally investigators acknowledge the asymmetry resulting from inelastic Fermi-photoelectron collisions in graphene [120] [121] [122] [123] [124] [125] [126]. This observation leaves these and other works [127] [128] [129] [7][6] to be reinterpreted since the asymmetry parameter alone can account for a significant fraction of the features claimed to be measured in data[2].

[1] The actual lineshape used is never mentioned.

[2] This is a key point in analysis. This is to say that the Shirley background of graphene, as describe in section 4.1.2, should be very small in the resulting fit

Modifications to graphene are likely to have a character extending in a direction normal to the crystal plane. Adsorbates and other types of defects will have valence orbitals extending out into the vacuum as opposed to disorder incurred by the substrate which lies below the atomic plane. XPS can readily measure the photoelectrons emitted from graphene – and from defected graphene. XPS is a quantitative technique that allows you to assume the relative faction of pristine/defected graphene, while the shift in the measured features provide information on the oxidation states of the graphene atoms. The nature of the modifications can be further revealed through their symmetries, which are not accessible through XPS. NEXAFS measurements of the symmetries of the excited state electronic configurations are performed to complement the XPS measurements.

5.2 Experimental Methods

5.2.1 Sample Preparation

Monolayer graphene samples grown through chemical vapor deposition, prepared on a 5 x 5 mm square substrate of highly hole-doped, thermally-oxidized silicon, were obtained.[3] The samples were annealed in ultra high vacuum (i.e., a starting base pressure of 5.1 x 10^{-9} Torr) at 300^{o} C for a total of four hours to remove adsorbates [139]. The annealing showed a negative chemical shift of less than 10 meV after two hours and no change thereafter. This small chemical shift could be due to water and other adsorbates such as PMMA residue [139][140]. The graphene, as a result of annealing, reached a chemical equilibrium with a featureless core level spectrum[4] and is therefore assumed to be in a practically pristine state. Following this, the graphene was ion bombarded with 500 eV argon ions which had the effect of dosing the graphene with lattice vacancies since the threshold to remove a single carbon atom is at least 90 eV [58]. The argon ion current was measured independently prior to dosing to maintain a consistent and uniform dosage of the graphene. Photoemission spectra were checked routinely for argon implantation by observing the argon K edge. For simplicity, approximately one defect is assumed to be created per argon ion. Since changes in the photoelectron signal due to defects appeared to be far more subtle than that seen in Raman spectra [58] the dosage was increased in near logarithmic steps.

[3] Multiple graphene samples were acquired from the Graphene Supermarket.

[4] By featureless it is meant that the core level spectrum does not have any obvious peaks such as those seen in the work of Pirkle et al. (2011) [139] and Lin et al. (2011) [140]

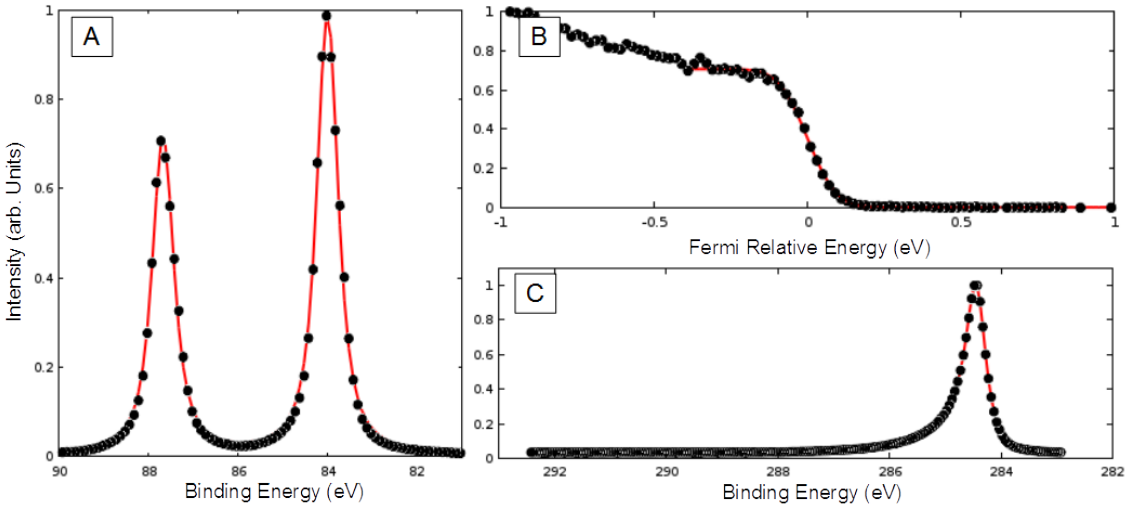

FIGURE 5.1: A)(black dots) Gold XPS signal. The $4f_{7/2}$ peak is taken to be at 84 eV whereas the spin orbit component $4f_{5/2}$ is found to be 3.7 eV higher at about 87.7 eV. (Red line) Voigt distribution fit. B) (black dots) Gold Fermi edge. (Red line) Fermi Dirac distribution fit, 100 eV Gaussian broadening. C) (Black dots) Pristine graphene C 1s XPS signal. (Red line) Single peak Doniach-Sunjic fit, Asymmetry 0.15, Lorentzian width 148 meV.

5.2.2 Spectroscopic Analysis

Photoelectron and NEXAFS measurements were preformed at the Australian Synchrotron Soft X-Ray beam line[5] with a spot size of 400 μm and excitation energy of 350 eV. Spectra were taken at an angle of 55^o after each dosage step with a SPECS hemispherical energy analyzer that utilizes the averaged signal of nine chaneltrons having a low pass energy of 10 eV to enhance resolution [82]. The C 1s core level energy and intensity was normalized to a standard gold 4f core level spectra measured at the start of our investigation, refere to figure 5.1A. The NEXAFS spectra were measured from the total electron yield by normalizing that signal to the photo-ionization current of a metal grid in the path of the x-ray source. The instrumental broadening was determined from a measurement of the photoemission edge of the gold standard held at room temperture. A fit calculated by the author to this edge with the Fermi-Dirac distribution, representing the occupancy of the conduction band at finite temperature, showed an instrumental broadening of 100 meV (see figure 5.1B). We found it sufficient to take this as the total instrumental broadening of the photoelectron lineshape since broadening from the x-ray source is taken to be independent of the excitation energy between the

[5]While any given beamline experiment can in principle be preformed by as few as two people, beamline experiments are constrained to be preformed within a time frame of about a week (The work described here was limited to 3 days). Hence, other people, mainly devoted beamline scientists directly familiar with the apparatus and additional scientists acting as spotters during measurement, are involved. Beamline scientists assist with the practicality of data acquisition while other assisting scientists act to spot potential problems. The resulting team of scientists, in effect, maximize the efficient use of time.

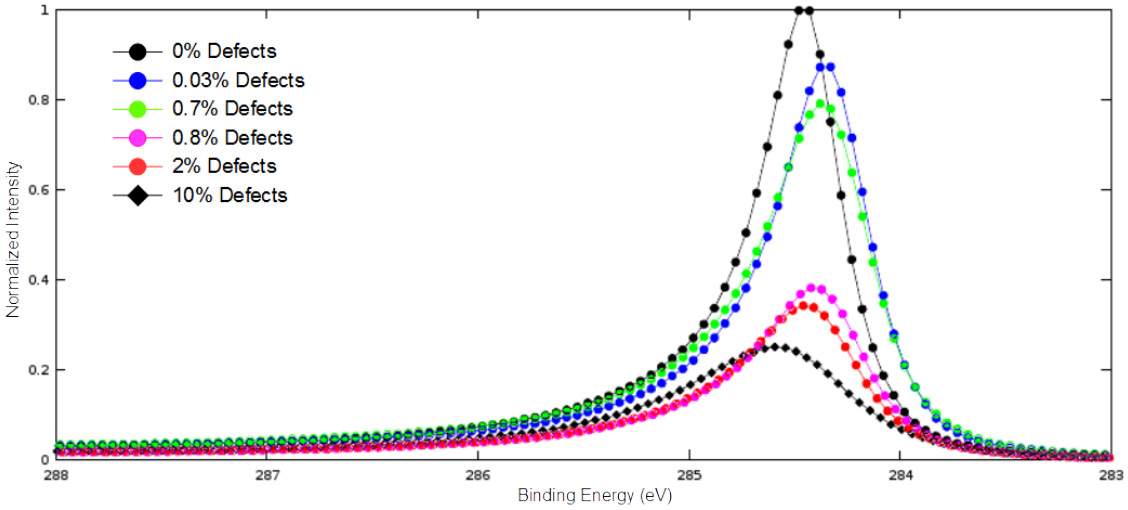

FIGURE 5.2: Graphene C1s Core Level XPS Spectra as a function of Argon Ion Irradiaton. (black dots) Unirradiated; (blue dots) 0.16 μA·s, 0.03% defects; (green dots) 4.00 μA·s, 0.7% defects; (magenta dots) 5.11 μA·s, 0.8% defects; (red dots) 10.1 μA·s, 2% defects; (black diamonds) 61.2 μA·s, 10% defects. An intensity correction referenced to a gold standard was done for each measurement.

gold emission edge and the excitation energy. As well, a previous analysis showed that an estimated instrumental brodening is likely to be within 5% of the actual value[6] [141].

The photoelectron data of the pristine graphene was initially fitted with a single broadened Doniach-Sunjic peak (refer again to figure 5.1C). This single peak fit determined the asymmetry index and Lorentzian width to be 0.15 and 148 meV, respectively. This is similar to what has been measured elsewhere [7][67]. That pristine lineshape was then used in a ten-peak fit of all the data. Using ten possible peaks to fit the data over-determines any possible vacancy defect peak distribution present in the graphene, as outlined by the work of Susi et al. (2014) [112]. I found that, in the pristine case, all but one of the peaks were suppressed, as expected. I conclude that the single broadened Doniach-Sunjic lineshape provides a satisfactory fit to the data and there is no evidence for multiple components in the pristine graphene lineshape. As vacancy defects were then added to the graphene through argon ion bombardment, an overall broadening of the C 1s core level signal over the range of zero to 10% defects was observed. This broadening, deconvolved into the ten-peak distribution, showed the development of a nine peak distribution about the original pristine maximum.

Since this preliminary multicomponent peak fit did not correlate well to theoretical expectations, the components could not be constrained appropriately to cases of a known set of binding energies and spectral widths. For this reason, to first order, I assumed that the nine peak distribution is a normal distribution of bombardment induced chemical

[6]Contributions from static disorder and phonon broadening due to the excitation of acoustic low-energy phonons is expected to be less than 50 meV of the net broadening [141].

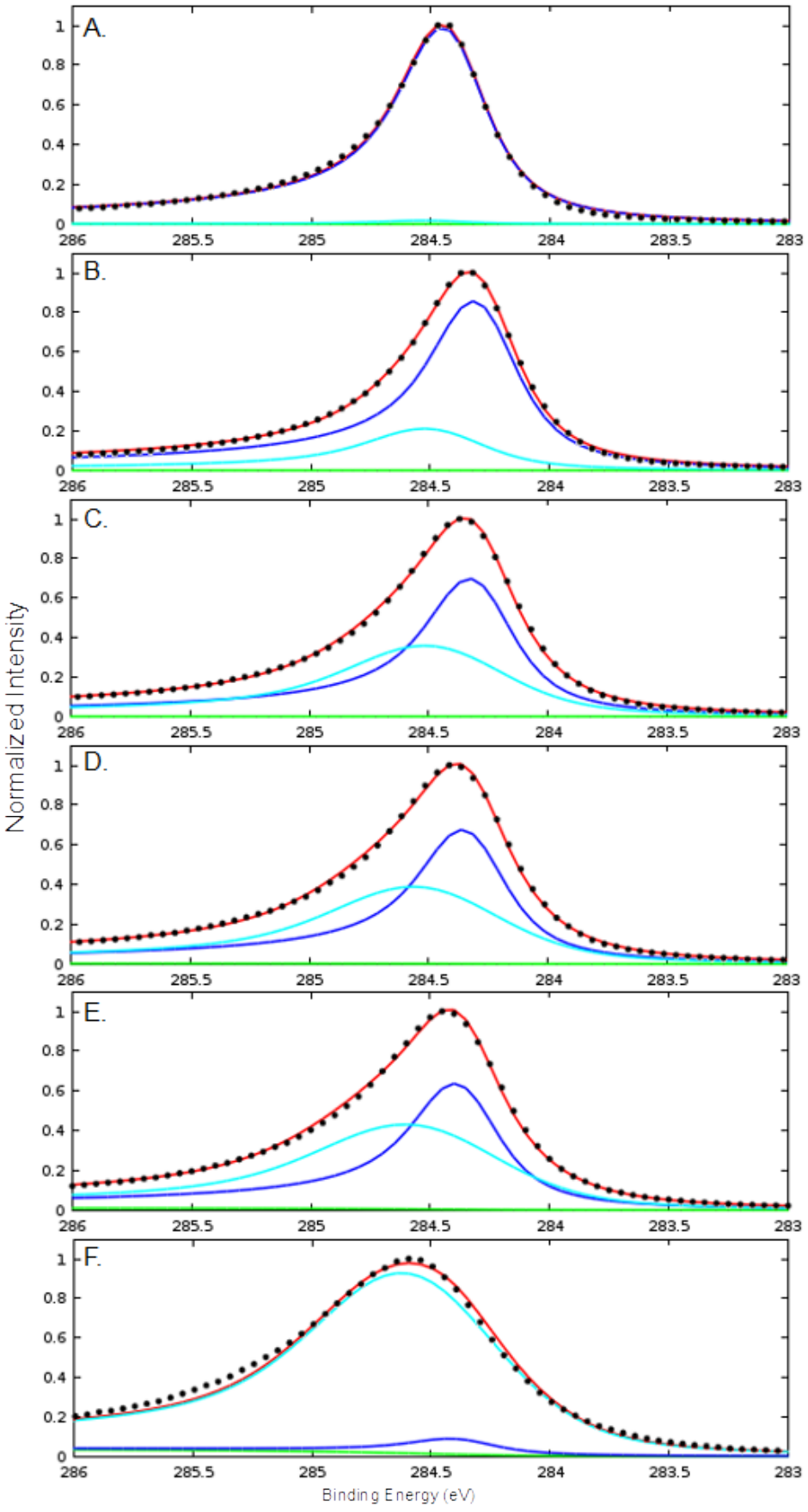

FIGURE 5.3: Evolution of the two peak fit (red lines) using the pristine linshape I_1 (dark blue lines), the defect induced lineshape I_2 (cyan lines) and an active Shirely background (green lines). Residual squared values: A) 0%, 4.5 x 10^{-5}; B) 0.03%, 2.6 x 10^{-5}; C) 0.7%, 2.0 x 10^{-5}; D) 0.8%, 2.7 x 10^{-5}; E) 2%, 4.1 x 10^{-5}; F) 10%, 2.0 x 10^{-4}

shifts on vacancy effected carbon atoms described by a Gaussian that convolves the pristine C 1s lineshape, I_1, over the observed energy range, i.e., this defect related distribution, I_2, can be written as,

$$I_2(\mathbb{E}) = \int_{\mathbb{E}} G_1(\mathbb{E} - \mathbb{E}')I_1(\mathbb{E}' - \mathbb{E}_o)\ \ d\mathbb{E}' \tag{5.1}$$

where G_1 is a Gaussian, and I_1, is itself a Gaussian convolution of the core-level Doniach-Sunjic type lineshape I_o [66], which can be expanded as

$$I_2(\mathbb{E}) = A\int_{\mathbb{E}} G_1(\mathbb{E} - \mathbb{E}')[\int_{\mathbb{E}'} G_o(\mathbb{E}' - \mathbb{E}'')I_o(\mathbb{E}'' - \mathbb{E}_o)\ \ d\mathbb{E}'']\ \ d\mathbb{E}' \ \ \Rightarrow \tag{5.2}$$

$$I_2(\mathbb{E}) = A\int_{\mathbb{E}} I_o(\mathbb{E}'' - \mathbb{E}_o)\ \ [\int_{\mathbb{E}''} G_1(\mathbb{E} - \mathbb{E}')G_o(\mathbb{E}' - \mathbb{E}'')\ \ d\mathbb{E}']\ \ d\mathbb{E}''. \tag{5.3}$$

Since the Gaussian convolution of a Gaussian is another Gaussian, this last equation can be written as,

$$I_2(\mathbb{E}) = A\int_{\mathbb{E}} G_2(\mathbb{E} - \mathbb{E}'')I_o(\mathbb{E}'' - \mathbb{E}_o) \quad d\mathbb{E}'' \tag{5.4}$$

where, A, is a fitting parameter and the net core level signal is described by the sum of I_1 with I_2 which then differ from one another by only intensity and Gaussian broadening. The function G_2 is the integral of G_1 and G_o. With this simplified reformulation of the preliminary ten peak fit results the data was again fitted with just two peaks I_1 and I_2 as described. It is from this perspective that the data will be interpreted in the following section.

5.3 Results and Discussion

5.3.1 XPS Results for Ar Ion - Irradiated Graphene

As shown in figure 5.2, the addition of vacancy defects generally broadens the C 1s lineshape. From figure 5.3, I found that the broadening can be accounted for by the

TABLE 5.1: Data reduction summary of figure 5.3

Defects	I_1 (Pristine C1s)		I_2 (Defected C 1s)		
(%)	Binding Energy (eV)	Area Fraction (%)	Binding Energy (eV)	Gaussian Width (meV)	Area Fraction (%)
0	284.42	98.3	284.50	100	1.7
0.03	284.29	68.7	284.42	180	31.3
0.7	284.30	57.2	284.46	255	42.8
0.8	284.33	53.0	284.50	283	47.0
2	284.37	47.8	284.53	310	52.2
10	284.38	5.0	284.55	315	95.0

reduction in intensity of the unbroadened C1s peak I_1, and the addition of a shifted and Gaussian-broadened component I_2. Figure 5.5A shows the Gaussian width of I_2 as a function of defect concentration. This Gaussian width appears to saturate towards 100% defect concentration.

Figure 5.5B shows the binding energy of the two components I_1 and I_2 as a function of defect concentration.

With the initial introduction of defects, the binding energies of both components decrease sharply, then they both slowly rise. The binding energy shifts are nearly parallel for both components which suggests a single cause likely resulting from a shift in the Fermi energy (doping) of the graphene. This could be due to removal of adsorbates by ion bombardment, creation of trapped charge in the substrate, or charge transfer to/from the defects themselves. The changes in binding energy are small, <150 meV. If this corresponds to a change in the Fermi energy then the change in carrier density would be less than $<1.7 \times 10^{12}$ cm^2 in neutral graphene, significantly smaller than the defect density.

The evolution of the integrated areas yields the fraction of defected graphene to pristine graphene shown in figure 5.4 resulting from the I_1 and I_2 components shown in figure 5.3. The plot is of the relative fraction of the pristine state to the defected state and is logarithmic in appearance. At the 100% concentration level (A 61.2 μA·s dosage) the pristine peak intensity falls below the nearly twice as wide defected peak intensity (figure 5.3F) and is obscured. This means that apparent linear increase in fraction above 20% may in fact saturate at a lower concentration.

5.3.2 NEXAFS Results for Ar Ion – Irradiated Graphene

The NEXAFS spectra of pristine graphene was observed to have five main features (see figure 5.6A). Most prominently is the split π^* resonance labelled as π_1^* and π_2^* and, the

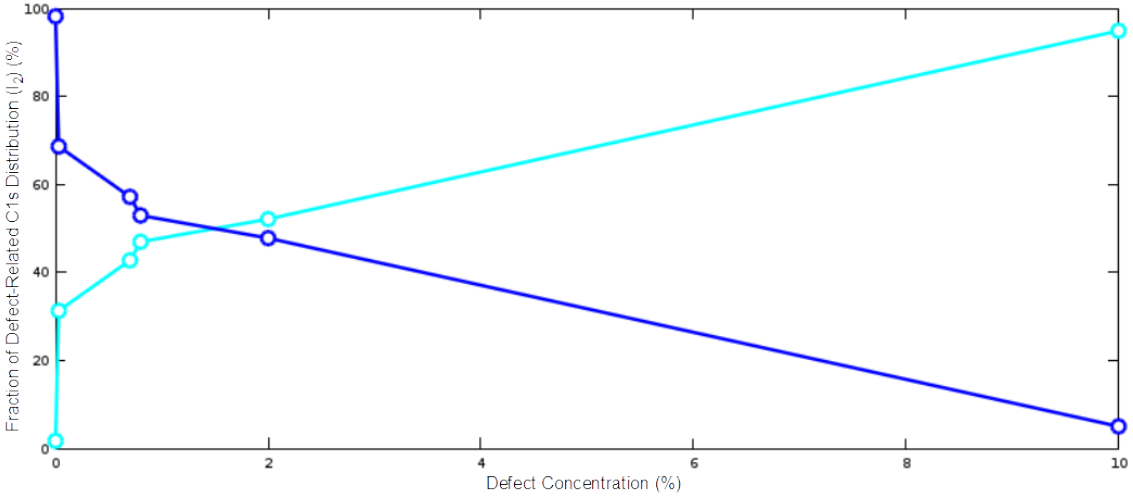

FIGURE 5.4: (Cyan) Plot of the fraction of the defect-related distribution, obtained from the relative areas of the pristine C1s lineshape, I_1, and the defect-related Gaussian broadened lineshape (I_2) vs. defect concentration calculated from argon ion irradiation. Relative areas were determined by the 2-peak fit of the measured spectra. (Blue) Plot of the fraction of the pristine graphene obtained in the same way.

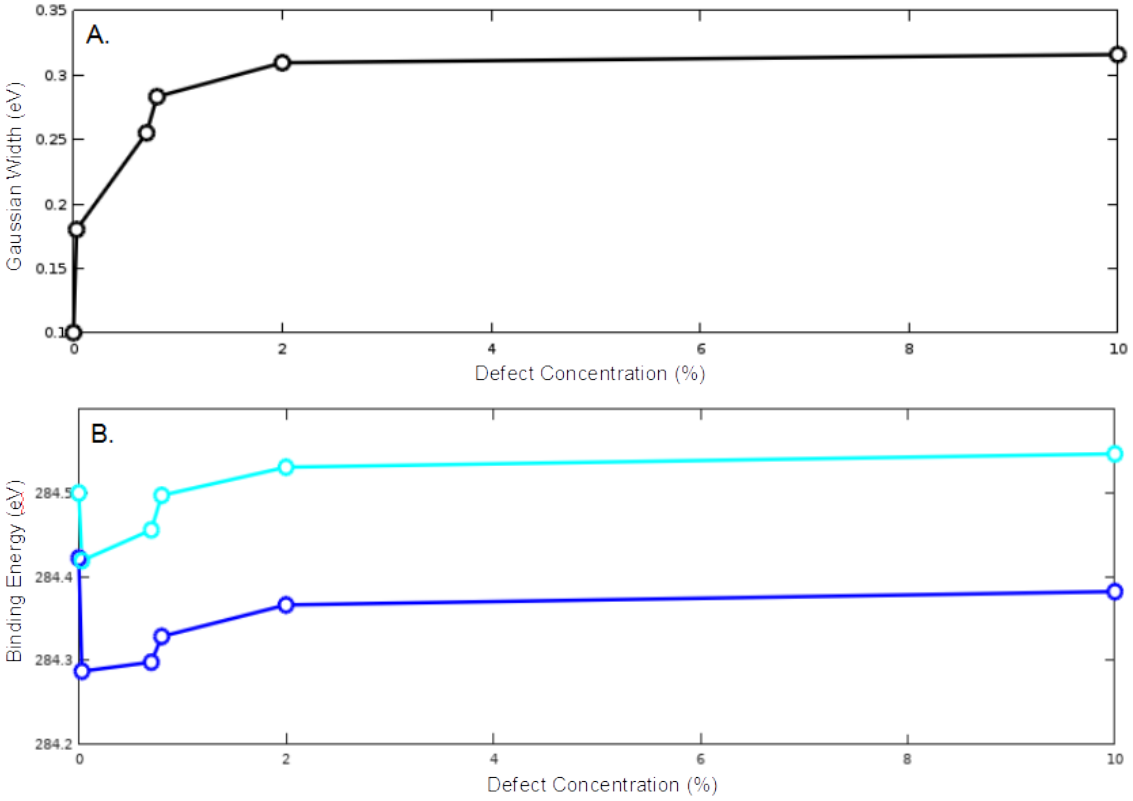

FIGURE 5.5: A) Evolution of the I_2 Gaussian width with increasing defect concentration. B) Evolution of the I_1 (dark blue) and I_2 (cyan) binding energies with increasing defect concentration.

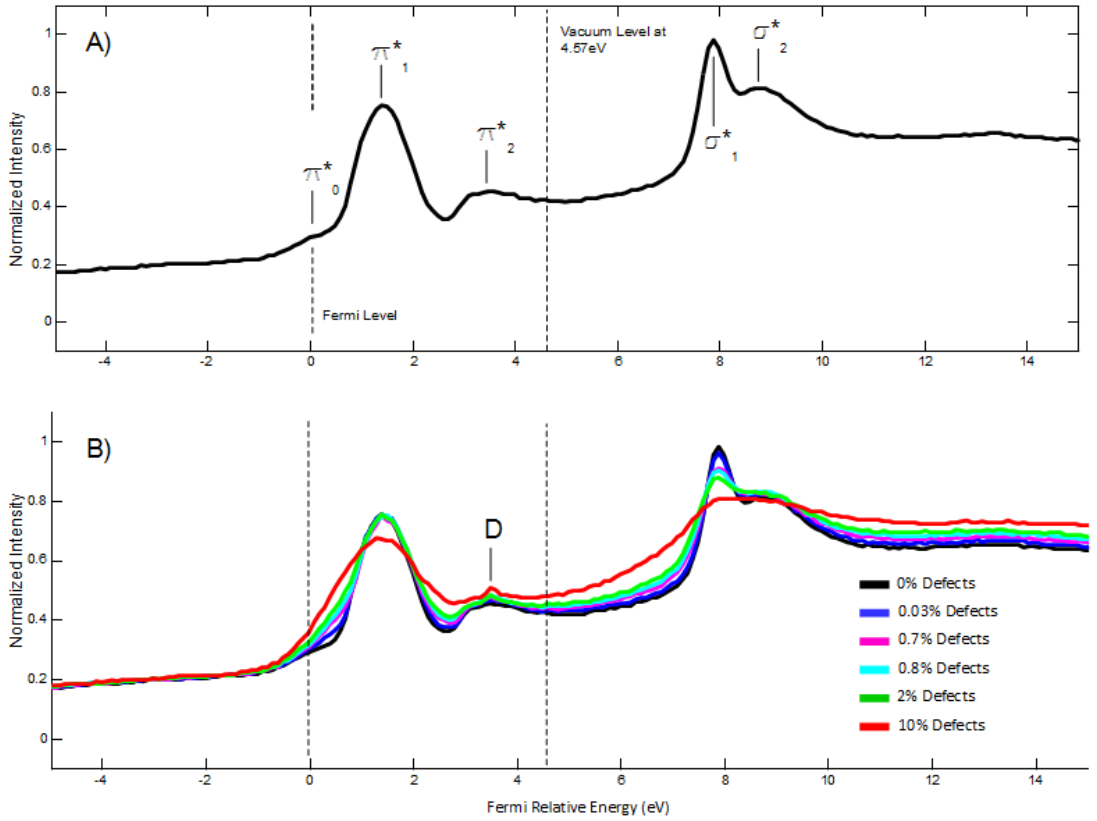

FIGURE 5.6: A)NEXAFS of the pristine state. B) Evolution of the NEXAFS with increasing percent of defects. The FWHM of the D resonance is estimated to be 300 meV which is 3 times that of the instrumental resolution.

split σ^* resonance labelled as σ_1^* and σ_2^*. The lowest energy feature is a faint shoulder just below the π_1^* resonance denoted as π_o^* and suggests the existence of hole doping [81][142]. As defects are added to the system, these five features are all broadened significantly causing the π_o^* feature to be obscured. The σ_1* resonance loses intensity in sequence with the expected loss of carbon resulting from vacancies and thus the loss of long range order [108]. A faint very sharp resonance labelled, D, observed on top of the π_2^* resonance forms and increases slightly in intensity with increasing defect concentration (see figure 5.6A). The appearance of this narrow D feature having a FWHM of about 300 meV is just three times that of the instrumental broadening. Such a narrow width suggests the emergence of a localized, long lifetime molecular-like state associated with the addition of vacancy defects [7].

5.3.3 Conclusions

The formation of vacancy defects through ion bombardment creates a concentration of modified carbon atoms associated with vacancy sites [58]. Within the double-peak

[7] Indeed, such sharp π-like resonances have been identified in C_{60} and C_{70} [131].

model, this manifests as the ever broader peak, I_2, whose width represents the energy range of modified carbon core levels as compared to pristine graphene carbons. That width, depicted in fugure 5.5B, which apparently saturates at high defect levels, yields an ever increasing concentration of defected graphene as seen in figure 5.4, however, the increase is not linear. To add to this, the secondary component peaks at higher binding energy[8] which is unexpected [112]. Generally, vacancy defects would reduce the binding energy of effected carbons since these carbons would have a reduced coordination.

At least it is clear that the vacancy sites are not in isolation. The graphene is of course adhered to its SiO_2 substrate. With regard to oxygen bonding, higher binding energy contributions to the C 1s signal have been expected from carbon bonding with ether/phenolic groups and ester/carboxylic groups [125]. This expectation that carbon-oxygen bonds produce positive chemically shifted components stems from other observations of reduced graphene oxide [143], ozone exposure of graphite [125] and atomic oxygen adsorbed on graphene [114]. The adsorption of atomic oxygen produced a component with a positive nearly 2 eV chemical shift. Silicon bonding, in contrast, has been described in the context of interfacial bonding between epitaxial graphene and its silicon carbide substrate. Positive chemically shifted components were also observed [126][7]. The shift, attributed to Si-C bonding, was noted to be on the order of 1 eV or less. In all, both oxygen and silicon are main components of the substrate and it is therefore possible that the effective splitting of the C 1s is due to a distribution of graphene substrate bonds.

The NEXAFS spectra shed some light on this idea. The split π^* resonance is indicative of adhesion of graphene with the substrate [2] and this splitting exists very clearly in the pristine state. With an increasing number of defects the D resonance is observed and increases in response. This very narow resonance appears coincident with the π_2^* resonance. This may suggest the formation of a very specific type of substrate hybridization. This is to say that the small chemical shift of the I_2 component is more characteristic of silicon bonding [7] and so the D peak may, for example, indicate that Si-C bonds are preferred over C-O bonds. However, this feature also lies very close to the vacuum level. Near-vacuum-level features have been seen in graphite [132], carbon nanotubes [136] and C_{60} [109]. In fact, the near-vacuum-level feature seen in graphite was attributed to either interlayer states [144] or defects [121]. A D-like resonance has analogously been seen in boron nitride thin films [134][135] and nanotubes [137]. More to the point, in a study of boron nitride exposed to argon ion bombardment, not only is the π^* resonance seen to split but a near-vacuum-level peak is observed which increases with increased bombardment independently of the π^* pair. Specifically, the analogue of

[8]The existence of the peak component, I_2, at higher binding energy is comparable to observations of graphene on metal surfaces [122]. The positive chemical shift of this secondary component is smaller, i.e., nearly 140 meV compared to about 565 meV between graphene on ruthenium and rhodium.

the π_2^* resonance (peak B in reference [135] and peak π_B^* in reference [134]) is seen to immediately saturate in intensity after the initial bombardment leaving only the D peak analogue to further increase[9] [135]. The appearance and enhancement of the D peak in the presence of lattice vacancies could also be explained as being due to the creation of excess Rydberg states. Such states would result from the existence of molecular-like vacancy edge carbon atoms. These excess states would exist far from the surface having little overlap with surface crystal states and be degenerate with image potential states [10] of the metallic graphene. Natural degeneracy breaking would thereby enhance the existing density of states at the vacuum level independently of crystal states.

In summary, argon ion irradiation gives rise to the formation of defect states which result in an increase of C 1s binding energy. From figures 5.2 and 5.3, the peak in the overall C1s binding energy distribution can be seen to initially shift to lower binding energy. From the two peak data reduction shown in figure 5.3 the pristine C1s peak decreases in binding energy (by about 100 meV), consistent with chemical changes for sp2 to sp3 carbon, and a broad C1s "Defected" peak increases in binding energy (by about 200 meV relative to the original position). The changes in the XPS spectra are correlated to changes in the NEXAFS in that there is an emergence of near vacuum level unoccupied states which increase in intensity with increasing defect concentration. This suggests a two step process.

Step 1, Carbon Activation

- C(graphene) + Ar^+ (500 eV) $\rightarrow$ C(graphene) + C*(activated)

Step 2, Different scenarios:

1. C* + H_2(g) $\rightarrow$ C-H (sigma bond) + H
2. C* + H–O–Si $\rightarrow$ C-H (sigma bond) + O–Si
3. C* + O $\rightarrow$ C-O-C

The first step involves surface roughening through ion bombardment which has been observed to leave hillocks in the electron density across the surface [58]. With roughening, the graphene is locally activated. For all carbon system, the binding energy increases when going from sp2 to sp3 carbon. The overall increase in binding energy of both I_1 and I_2 is seen in figure 5.5B could reflect this.

If the near vacancy edge activated carbon does not react then a negligible shift of less than 100 meV would be anticipated since the electronegativity of the sp2 carbon should

[9] This feature is also enhanced in the presence of oxygen for single wall carbon nanotubes [137]

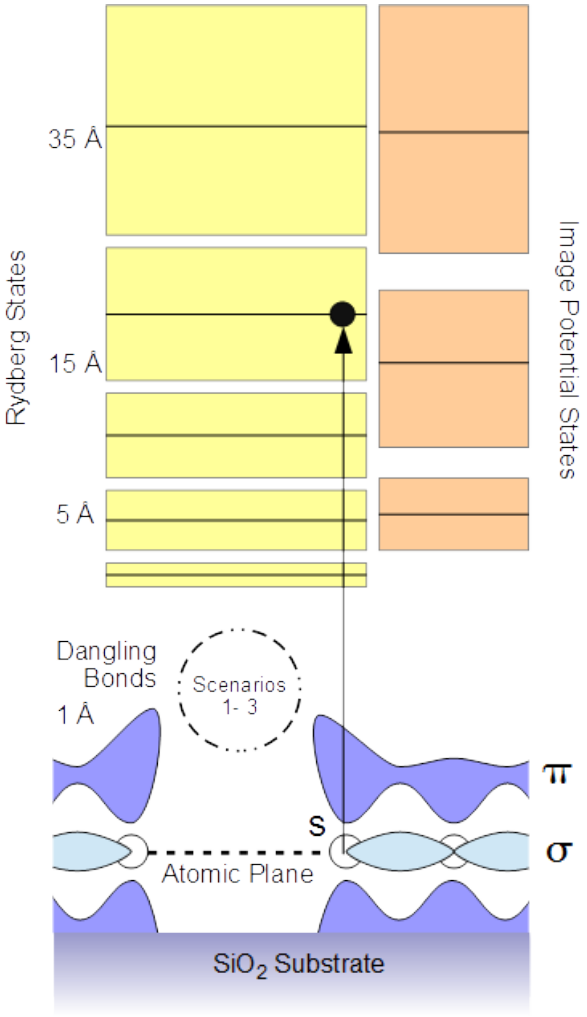

FIGURE 5.7: Diagram showing the hypothetical spatial orientation of the molecular orbitals in the presence of lattice vacancies. The visualization of the image potential states (and by analogy the Rydberg states) was derived from reference [10]. Implicitly, the Rydberg states have been assumed to be spatially more localized to the vacancy region and would therefore overlap the strongest with lower energy image potential states.

be nearly that of the activated. Thus, in the second step the activated carbons are likely being passivated as they form. The observed binding energy shift of the I_2 peak suggests what types of chemical termination may be involved. Substrate bonding to silicon would increase the overall binding energy, however, it is not easy to rationalize why a random ion bombardment would yield a very particular substrate bonding arrangement[10] Another possibility is that these carbenes bind with residual vacuum hydrogen.

Vacuum hydrogen bonding may be more energetically favourable. Binding energy in the range of 284.5 to 285 eV are often assigned to hydrocarbon bond formation since the C-H bond is energetically more favourable than C-O or C-Si bond formation [113]. Binding energy shifts in the range of less than 400 meV have been expected [112].

[10]Keep in mind that the substrate, which results from thermal oxidation of single crystal silicon, generally lacks long range symmetry to any apprciable domain size.

Residual vacuum hydrogen is also ever present in UHV systems and when one considers the ion gun used to ionize and bombard with argon it is likely residual hydrogen is in close company. Surface bound hydrogen on a roughened graphene surface would have a molecular-like character. Photoelectrons far from the surface that are associated with these hydrogen passivated vacancy sites must have zero orbital angular momentum and are then likely to enter Rydberg-like states when excited to energies near the vacuum level, see figure 5.7. These states will be degenerate with pre-existing image potential states and thereby enhance the density of states near the vacuum level in proportion to the defect density.

Future work to elucidate the vacancy effect will involve three main parameters. The first is control over the argon ion energy. The Gaussian approximation of the I_2 peak does not encompass the asymmetry observed when the defected graphene lineshape is deconvolved into ten or more components. The 500 eV argon ions are far above the 90 eV threshold and may be creating more complex defect types. Activating the surface at lower energies may then produce a normal distribution of a single defect type and in turn a symmetric broadening of the I_2 peak. The second is control over the chemical environment. The vacuum level of the system can be pushed to lower pressures removing residual hydrogen. The "back filled" ion gun used can be replaced with differentially pumped gun further ensuring extraneous residual gas is not involved in the bombardment process. In a state of the art UHV environment one would expect the the defect lineshape and position to change with various chemical species other than hydrogen. Finally, time resolved XPS and angle resolved XPS (ARPES) can yield a more detailed surface state picture which could be correlated with scanning probe measurements.

Chapter 6

Scanning Probe Microscopy

The goal of this chapter is to describe my work concerning scanning tunnelling and atomic force microscopy. This chapter is divided into three sections. The first section covers the work I have done to design a device-oriented scanning tunnelling / atomic force microscope, which later supported the purchase of a scanning tunnelling / atomic force microscope. This purchased instrument was then calibrated and used to acquire data. The second section describes the calibration done on the instrumentation that was purchased. The last section describes local density of states measurements which I performed and shows the resultant data.

6.1 Design Parameters

Scanning tunnelling and and atomic force microscopy, over the past three decades, have helped pave the way for nano-scale science of nano-scale devices. Scanning tunnelling and atomic force microscopy allow one to measure correlations between the surface structure and the performance of a device. My work has had the aim of of measuring local defects in the surface lattice structure of a device and correlating this with global transport measurements.

Scanning tunnelling microscopy (STM) measurements are markedly different from atomic force microscopy (AFM) measurements, although, both are applied to the determination of surface structure and the two techniques can be practically used simultaneously. The STM is the more basic measuring technique due to its use of a single feedback system to locate surface structure, shown in figure 6.1A. In contrast, the AFM, depending on the type of surface structure being investigated, uses a number of multiple feedback systems [145] as illustrated in figure 6.1B.

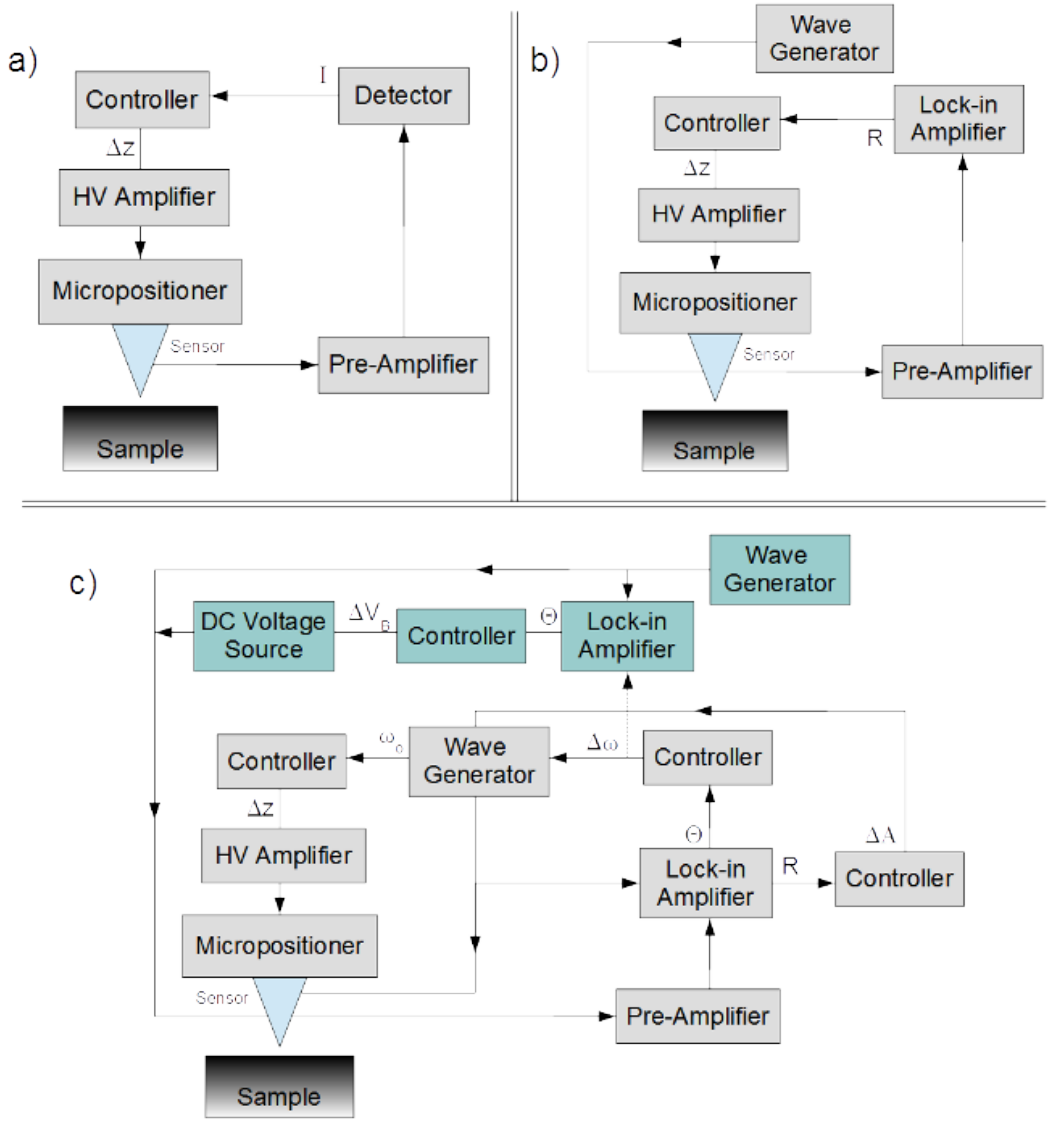

FIGURE 6.1: A "zeroth order" expansion of three scanning probe microscopes in terms of basic lab equipment. a) Scanning tunnelling microscope: I, is the current detected and Δz is the correction to the sensor-sample distance. b) Amplitude-modulated atomic force microscope: R is the root-mean-square amplitude of the cantilever signal and Δz is the correction to the sensor-sample distance. c) Θ, is the phase of the cantilever signal relative to the driving signal; R, is the root-mean-square amplitude of the cantilever signal; ΔA, is the correction to the cantilever amplitude; Δw, is the correction to the driving frequency, i.e., the frequency shift; w_o, is the resulting driving frequency; Δz is the correction to the sensor-sample distance; (blue) Θ, is the phase of the frequency shift relative to twice the bias voltage modulation frequency; ΔV_B, is the correction to the bias voltage.

The STM, which measures electrons tunnelling from surface electronic states, is used to locally determine the density of states of surface structure. A single atomic scale defect on a surface will register as a notable change in the local density of states for a given energy through STM. That defect can then be identified as a lattice vacancy or adatom by measuring spatial extent relative to the surrounding surface. The AFM measures the molecular surface force or the force gradient which implicitly includes a measure of the local work function. This local work function, which is the energy required to free electrons from the surface will also change in the presence of adatoms or structural defects.

The main challenge of performing both STM and AFM on nano-scale devices is mating the sample to be measured with the sensor without destroying the sample or sensor. Doing so at the nano-scale is accomplished by first approaching at a larger scale (millimeters down to microns). Then the final nano-scale measurement is tuned to what is required. A modern off-the-shelf microscopy system capable of doing this is not yet common. Therefore, as a part of the Williams group at the University of Maryland, I set out to design a microscopy system with this capability.

I decided that large scale coupling of the nano-scale sensor with a nano-scale surface is best accomplished optically. An optical apparatus can illuminate the sample with low radiation power at a select frequency. This has the advantage of avoiding any burning of the sample[1].

Optical illumination and detection of the sample is not trivial in that it requires high angle reflective bright field alignment of the optics away from the surface normal. The high angles needed ($\approx 120^o$) are a result of the sensor necessarily being in the optical path. Fortunately, the optics required for either the detection or illumination can be purchased as a single unit. Such a unit is known as a long-working-distance microscope[2] and is specified with a resolution on the order of 3 to 5 μm.

Actual movement of the sensor relative to the device is best accomplished with a piezo based inertial micropositioner. The inertial micropositioner is a scheme where a series of piezo stacks actively move or "walk" along a raceway. The orientation of the stacks and raceway is relative, which means the stacks can also remain stationary thereby allowing the raceway to move instead. The size of the raceway determines the extent of the motion. In figure 6.2a and b one can see two traditional examples of inertial micropositioners where the stacks move [146]. Figure 6.2c shows a configuration where the raceway moves [147].

[1] chemically altering, vaporizing or melting of the sample

[2] These working distances are on the order of 300 mm or more.

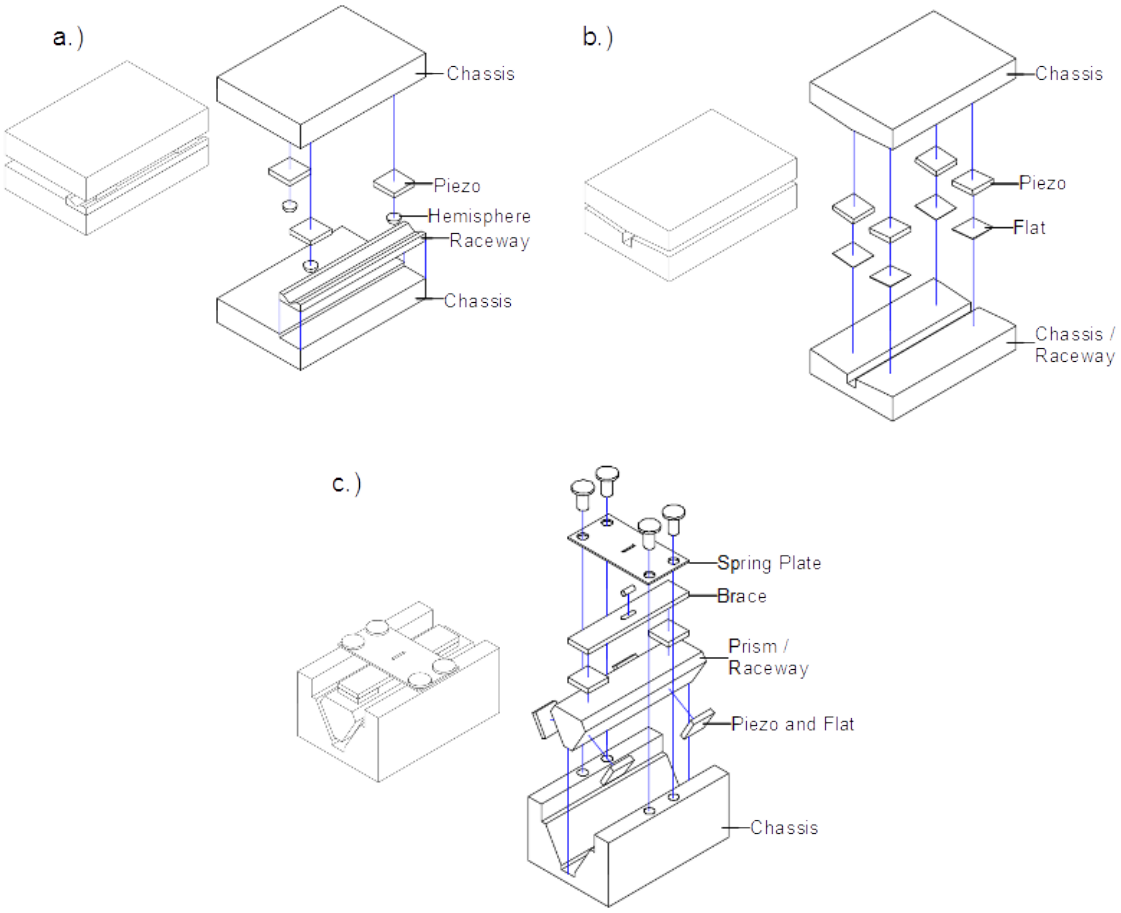

FIGURE 6.2: A) Ball bearing-like linear micropositioner design. The hemispheres apply a large pressure to the raceway. The race way is typically made from a material much harder than the chassis. B) A low pressure contact linear micropositioner design. Here a single raceway is used. The hardness of the raceway material is less critical and can be part of the chassis. The large area of the flats prevent wear over time. C) An adaptation of B to scanning probe microscopy. Here, the geometry is inverted in that what is now the raceway (prism) moves while the chassis is stationary. For this geometry the probe is often connected to the prism and moved in a direction along the main axis.

If the sample is an electrical device, the device itself must be electrified to make correlations between the STM measurements and the device transport measurements. Devices are typically created in a Hall / transistor configuration. This requires that the device have a gate, source and drain along with at least four other contacting electrodes[3]. The final design to be implemented at the University of Maryland was intended to have two sets of four contacting electrodes which would actively connect to the device.

To summarize, the main design parameters for the device oriented microscope designed at Maryland are as follows:

- Reflective bright field imaging of the sensor / device region with at least 5 μm resolution.

[3]There are typically more than four since electrode failure is common

- Control over three degrees of freedom of the sensor / device orientation.
- At least a 1 μm square field of view for STM and AFM.
- At least seven electrical contacts to the device.

This preliminary work supported later construction of a microscope now housed at the University of Maryland. Later, funding for the development and purchase of two separate systems specified to include these design characteristics was obtained. Those systems were placed and operated at Monash University, Melbourne, Australia. The main difference between the newly purchased systems and the system designed at Maryland was an additional criterion regarding sensor-surface stability from 300 K down to 4.2 K. At 4.2 K additional sensor-surface stability was specified on application of a 2 T magnetic field.

6.2 Calibration

Calibration of both the STM and AFM first requires understanding each measurement technique. In this section I mainly describe the calibration performed on the newly purchased microscopy system. First I will cover the physics of both STM and AFM separately then describe the calibration procedures necessary to obtain local density of states measurements.

6.2.1 Tunnelling Current

Tunnelling current[4], as the name implies, relies on the tunnelling of electrons between the sensor material and sample material through a vacuum barrier. The sensor and sample are metals held with a potential difference between them. The potential difference allows electrons in the filled states of one material (the source) to tunnel into the empty states of the other (the sink). The tunnelling current is then a result of the rate at which electrons transition through the vacuum barrier from the source to the sink[5]. This is scaled by the number of occupied states in the source and the unoccupied states in the sink, i.e.,

$$I = 2q(2\pi\hbar^{-1}) \int_0^\infty |M_{01}|^2 \quad D(\mathbb{E}) f(\mathbb{E}) \quad D_1(\mathbb{E}+qV)[1-f(\mathbb{E}+qV)] \quad d\mathbb{E} \quad (6.1)$$

[4]Early observations of current through thin oxide films established the phenomenon of tunnelling [148]

[5]The source and sink could be the sample or sensor

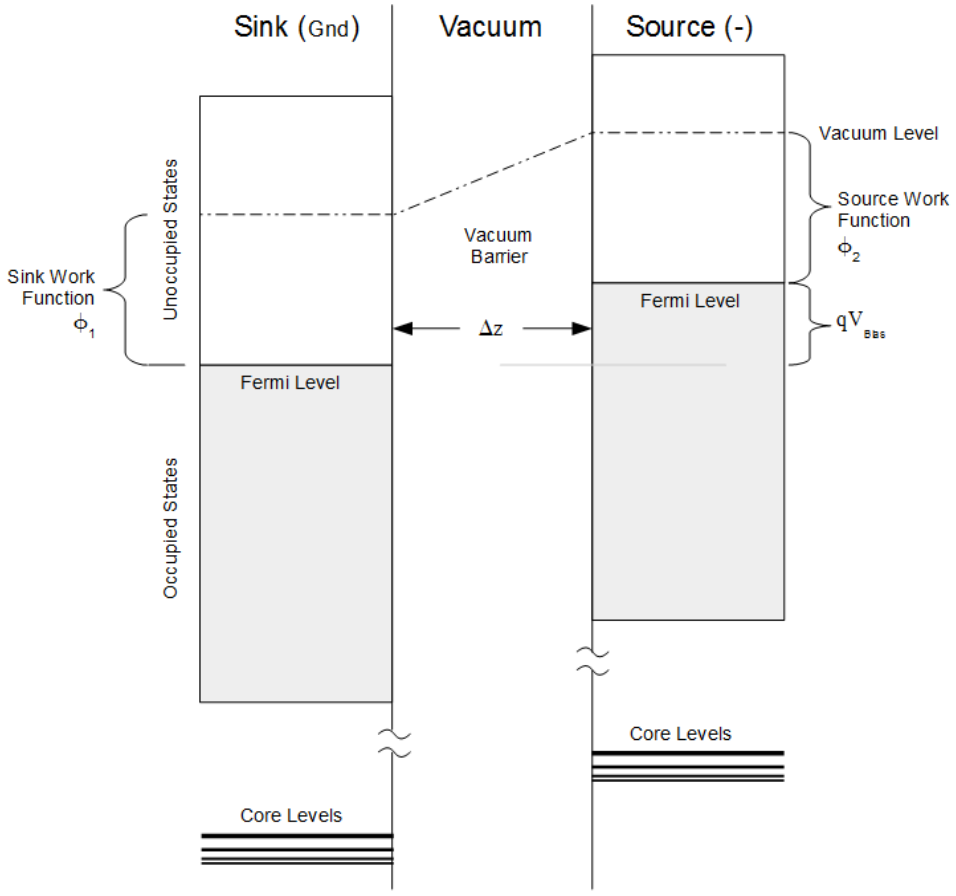

FIGURE 6.3: Energy diagram illustrating the vacuum barrier resulting from the work function difference and applied bias voltage between a sensor and sample labelled interchangeably as the source and sink.

Here n_1 is the source and n_o is the sink density of states[6] held at a bias V between them. The quantity $|M_{01}|^2$ is the tunnelling matrix of transition between the source and sink akin to Fermi's golden rule[7] [150]. Not all the current will occur from source to sink and at high temperatures the net current will be reduced by a small back flow, i.e.,

$$I = 2q(2\pi\hbar^{-1}) \int_0^\infty |M_{01}|^2 \quad D(\mathbb{E}) n_1(\mathbb{E}+qV) \\ (f(\mathbb{E})[1-f(\mathbb{E}+qV)] - f(\mathbb{E}+qV)[1-f(\mathbb{E})]) \quad d\mathbb{E} \tag{6.2a}$$

$$= 2q(2\pi\hbar^{-1}) \int_0^\infty |M_{01}|^2 \quad D(\mathbb{E}) n_1(\mathbb{E}+qV) \\ [f(\mathbb{E}) - f(\mathbb{E}+qV)] \quad d\mathbb{E} \tag{6.2b}$$

[6] Of course, tunnelling occurs at the scale of the sensor structure and so it is actually the local density of states.

[7] Tunnelling is formally different in that the wave functions of the source and sink are nonorthogonal states of different Hamiltonians [149]

To fully describe the tunnelling current, the wave functions of the source and sink must be known [151]. A free electron of mass, m, with energy, $\mathbb{E}$, within the source or sink bounded by a vacuum barrier, $U(z)$, will be modified at the boundary by an exponential [151], i.e.,

$$\psi(z) = \psi(0)e^{-kz} \qquad \text{such that} \tag{6.3}$$

$$k = [2m\hbar^{-2}(\mathbb{E} - U(z))]^{1/2} \tag{6.4}$$

where $\psi(0)$ is the electron wave function at the boundary. This bounded wave function depends on the atomic structure of the sensor or sample and is generally not known [151]. One is therefore motivated to simplify equation 6.2b and to that, a few approximations can be made. Firstly, one can assume the system is at a reasonably low temperature for which the Fermi-Dirac distribution, $f(\mathbb{E})$, is step-like[8] and there is no current back flow. In this limit the energy range is restricted to between qV and the Fermi level and the density of states for a metallic sensor over that range is assumed to not change appreciably [12]. As well, the wave functions in the sensor and sample interact through decay only so that the overlap of the two wave functions is nearly independent of energy. Here equation 6.1 becomes,

$$I \approx 2q(2\pi\hbar^{-1})|M_{01}|^2 D_1(qV) \int_0^{qV} D(\mathbb{E}) \quad d\mathbb{E} \tag{6.5}$$

The sensor should in principal be capable of detecting the smallest possible structure and towards this limit the sensor becomes a point source/sink for current. In effect, the density of states of the sample, n_o, is only the local density of states at the position of the sensor and this resultant one-dimensional current path allows the tunnelling matrix to be described under the WKB approximation [151] [149], i.e.,

$$I \propto e^{-2\kappa z} \quad \Rightarrow \tag{6.6}$$

[8] At liquid helium temperatures this amounts to a sharpness of 0.36 meV which also happens to be the work function of an electron in Earth's gravitational field.

$$I = I_o e^{-2\kappa z} \int_0^{qV} D(\mathbb{E}) \quad d\mathbb{E} \tag{6.7}$$

Here κ takes on the same form as k except the barrier, $U(z)$, has been integrated over the vacuum distance, Δz, and results from both the applied potential difference, V, and the work functions of the sensor, ϕ_1, and sample, ϕ_2. More specifically, the difference between the sensor and sample work functions creates a linear change in potential energy through the vacuum, i.e.,

$$\phi(z) = \phi_1 + \frac{\Delta\phi + qV}{\Delta z} z \tag{6.8}$$

where the contact potential difference, $\Delta\phi$, is the difference between the sensor and sample work functions, namely, ϕ_1 and ϕ_2 such that $\phi_1 < \phi_2$ (see fig. 6.3). Other factors such as image charge will act to further modify the barrier and in general, the barrier is asymmetric (see figure 6.4) [151].

The expression for the tunnelling current (eq. 6.7) does indeed hold in the case where 1) the sensor has a uniform density of states, 2) the bias voltage is less than ≈10 mV, 3) the temperature is low and 4) only s-wave electrons are involved in the tunnelling [151]. In practice the low voltage approximation is often violated where bias voltages between ±4 V are needed to achieve a high dynamic range [152].

6.2.2 Cantilevers

The cantilever based sensor depends on the collective molecular interaction of the sensor materials and sample material at the scale of the sensor. The forces involved near the sensor-sample interface vary from attractive to repulsive during approach which is what one expects from observations of condensing noble gases [153]. Over a long range, the sensor and sample are weakly attracted to one another through van der Waals forces which fall off as z^{-7} [154]. Over a much shorter range, the sensor and sample are strongly repelled as z^{-13} just as any two objects are repelled by one another on contact

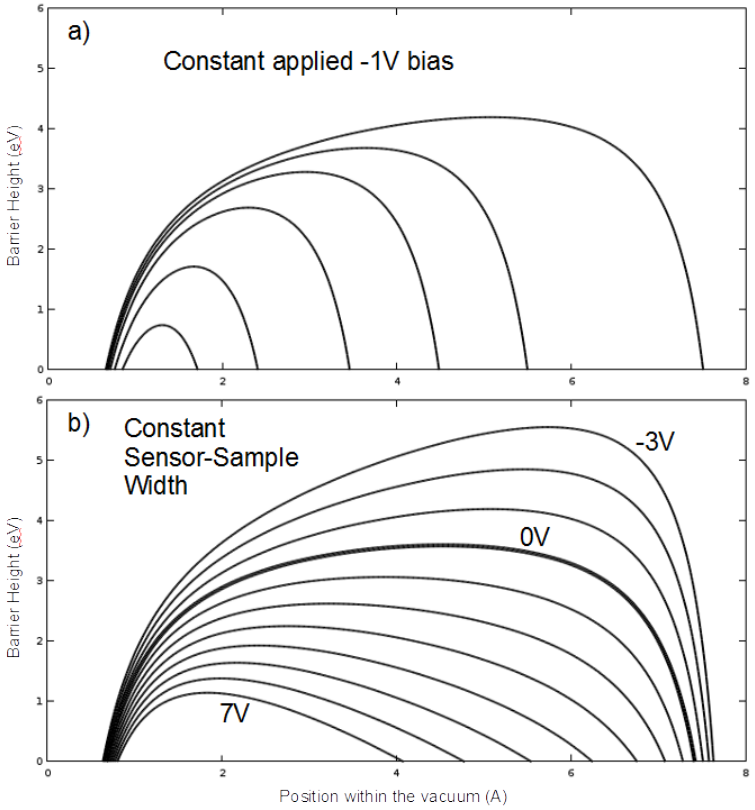

FIGURE 6.4: Calculation of the tunnel barrier using the work functions of graphene 4.6 eV and palladium 5.4 eV recreated from reference [11]. This calculation of the sensor-sample separation dependent potential barrier, $U(z)$, includes the effects of image charge which contributes to the potential like $1/[z(\Delta z - z)]$ [12][11]. a)The barrier at an applied -1V bias as a function of sensor-sample separation. b) The barrier at constant 8Å sensor-sample separation as a function of applied bias voltage.

[153]. The net potential energy between the sensor and sample may be described by the Lennard-Jones potential [155],

$$U = -\mathbb{E}_B \left[2\left(\frac{z_o}{z}\right)^6 - \left(\frac{z_o}{z}\right)^{12} \right] \tag{6.9}$$

Here the potential is segregated into two regimes that of attractive interactions where the potential energy decreases as the sensor-sample distance decreases and, that of repulsive interactions where the potential energy increases as the sensor-sample distance decreases.

As the cantilever type sensor approaches the sample, the collective forces deflect the cantilever away from its resting position in proportion to the spring constant of the cantilever, k (1800 to 2000 N/m). To first order, the cantilever can respond with simple

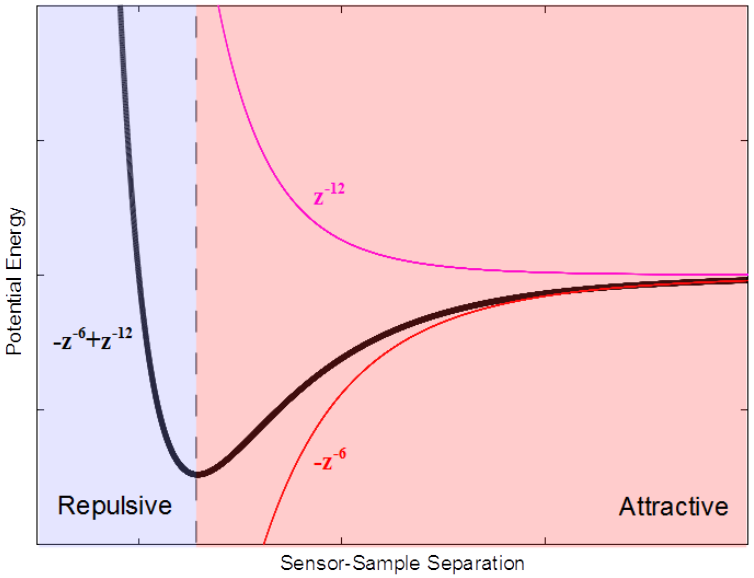

FIGURE 6.5: A calculation of the Lennard-Jones potential (black). Shown in red is the attractive Van der Waals component. Shown is magenta is the repulsive empirical component

harmonic oscillations at a frequency, ω (2π 32 kHz). The motion takes the form,

$$F = m(d^2z/dt^2) - C(d^2z/dt^2) + kz \quad \text{or} \tag{6.10}$$

$$F(m-C)^{-1} = (d^2z/dt^2) + k(m-C)^{-1}z \tag{6.11}$$

where $w^2 = k(m-C)^{-1}$ is the oscillation frequency and C is a damping parameter (0.1 μg). Equation 6.11 has solutions of the form

$$z = Ae^{iwt} \tag{6.12}$$

If C is greater than m, then w is a complex quantity, i.e.,

$$w = \alpha + i\beta \quad \Rightarrow \tag{6.13}$$

$$z = Ae^{i\alpha t - \beta t} = Ae^{-\beta t}e^{i\alpha t} \tag{6.14}$$

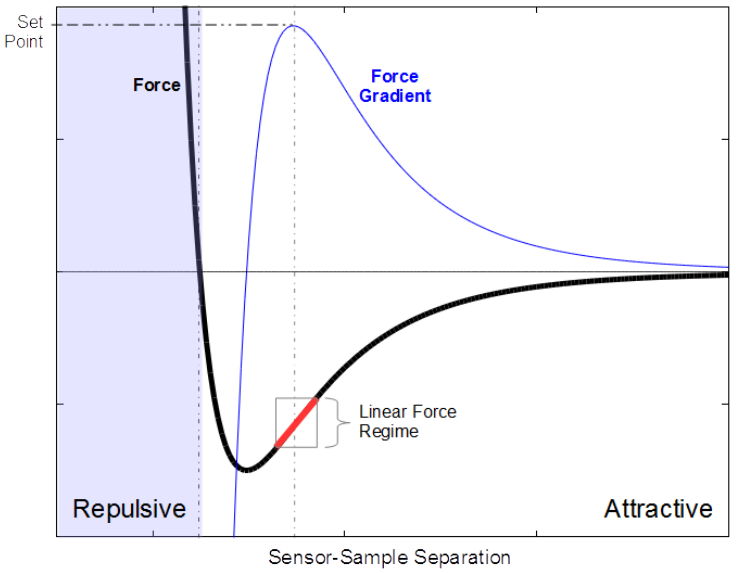

FIGURE 6.6: A calculation of the sensor-sample force (black) and force gradient (blue). The maximum in the force gradient defines the operational set point for a frequency modulated measurement. Highlighted in red is an operation window that defines the optimal cantilever oscillation for which the force is linear.

Equation 6.14 shows that the amplitude of the cantilever is exponentially damped. This damping, in this context, will be considered due to energy losses from inelasticity of the cantilever system.

Damping of the cantilever occurs after any impact with the sample. The response can be characterised by a ratio of the cantilever deflection to the force applied, which is essentially the reciprocal of the cantilever spring constant, namely $(dz/dF_o) = k^{-1}$. From this perspective, a more flimsy cantilever will produce a greater response, though a flimsy cantilever is more susceptible to chemical bonding with the sample[9]. This phenomenon is commonly observed as jump-to-contact, in which, a chemical bonding event appears as an abrupt change in the sensor-sample system.

One way around this is to drive the cantilever at resonance and measure the root-mean-square amplitude of the cantilever in response to the sample. This will be referred to as the amplitude modulation (AM) method[10]. This technique does not actually prevent chemical bonding but makes it less likely during scanning.

Sensitivity is defined as the ratio of the resultant change in the z position of the tip to the change in the surface force that produced it, i.e., (dz/dF_o). Where sensitivity is paramount, it is more practical to avoid contact with the surface altogether thereby avoiding chemical bonding. This means that one must use the weaker attractive forces

[9] This implies that equation 6.9 is not a complete description, i.e., there is a bound state in the contact regime. Indeed, the repulsive term in eq. 6.9 is entirely empirical [156]

[10] Amplitude modulation is commonly known as tapping mode. The author uses the term AM as opposed to tapping mode to better preserve the physics involved

to detect sample surface structure. In this regime, it is the van der Waals forces which are being detected as an additional damping on the the cantilever. The dynamics of the cantilever for this type of interaction is that of a damped driven harmonic oscillator (i.e., a second order dynamic process, refer to equation 6.11),

$$m(d^2z/dt^2) + \lambda(dz/dt) + k(z-s) = sin(\alpha t) \quad \Rightarrow \tag{6.15}$$

$$m(d^2z/dt^2) + k(z-s) = sin(\alpha t) - \lambda(dz/dt) \quad \text{where} \tag{6.16}$$

$$F = sin(\alpha t) - \lambda(dz/dt) = F_o + (dF_o/dz)(z-s) + ... \quad \Rightarrow \tag{6.17}$$

$$m(d^2z/dt^2) + k(z-s) = F_o + (dF_o/dz)(z-s) \tag{6.18}$$

where the net driving force has been Taylor expanded to first order. This expansion describes the fact that the net driving force is a combination of the force delivered by the driver and sensor-sample interactions. One can see that the net force $F = F_o + (dF_o/dz)\Delta z$ is a function of the force gradient about a set point, $\Delta z \equiv z - s$. For maximum sensitivity the set point is taken to be that point where the force gradient is a maximum, see figure 6.6.

For small amplitudes the force gradient from sensor-sample interactions will modify both the spring constant and resonant frequency, i.e., from equation 6.18 let

$$F_o = m(d^2z/dt^2) + [k - (dF_o/dz)](z-s) \tag{6.19}$$

This allows one to define an effective spring constant,

$$k_o \equiv k - (dF_o/dz) = k - \partial_z F_o \quad \Rightarrow \tag{6.20}$$

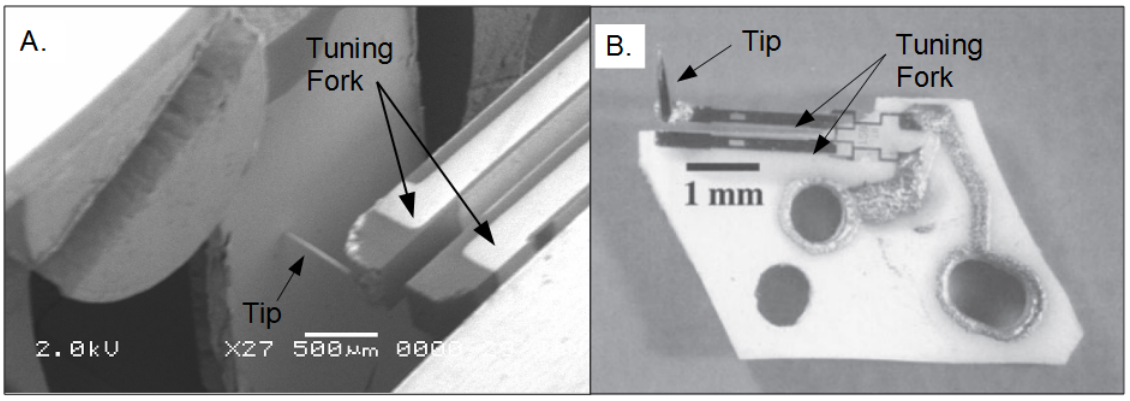

FIGURE 6.7: a.) Scanning electron microscope image of an early AFM sensor designed by the author used to image gold (111) at room temperature ($Q \approx 40000$, $k \approx 2000$ N/m and $\omega \approx 2\pi 32768$ Hz). A quartz crystal tuning fork is used as the resonator. A chemically etched platinum-iridium wire as in figure 6.8 was used as the AFM and STM sensor. b.) An example of a comercially available AFM sensor which the sensor in a. is based on. This sensor was developed by F. Giessibl and is known as the qPlus sensor. The picture was taken from reference [13].

$$w = (k_o m^{-1})^{1/2} \tag{6.21a}$$
$$= (km^{-1} - \partial_z F_o m^{-1})^{1/2} \tag{6.21b}$$
$$= (w_o^2 - \partial_z F_o m^{-1})^{1/2} \tag{6.21c}$$
$$= w_o(1 - \partial_z F_o m^{-1} w_o^{-2})^{1/2} \tag{6.21d}$$
$$= w_o(1 - \partial_z F_o k^{-1})^{1/2} \quad \Rightarrow \tag{6.21e}$$
$$w \approx w_o(1 - \frac{1}{2}\partial_z F_o k^{-1}) \quad \Rightarrow \tag{6.21f}$$

$$\Delta w \equiv w_o - w \approx \frac{1}{2} w_o \partial_z F_o k^{-1} \tag{6.22}$$

where Δw is the frequency shift which is proportional to the force gradient and $w_o^2 \equiv km^{-1}$ is the unperturbed resonant frequency. The frequency shift can be directly measured by demodulating the cantilever response. This frequency modulation method leaves one to calculate the atomic force by integrating over the force gradient.

One can now compare FM detection to static repulsion, i.e., refer to equation 6.11)

Frequency Modulation

$$(dz/dF_o) = \frac{1}{2} w_o \Delta w^{-1} k^{-1} = \frac{1}{2} Q k^{-1} \tag{6.23}$$

Static Repulsion

$$(dz/dF_o) = k^{-1} \tag{6.24}$$

where, Q, is known as the "quality factor" or q-factor which typically refers to the quality of a resonator, *i.e.*, the sharpness of resonance. Clearly both methods are limited by k. Still, driving the cantilever at resonance in the attractive regime provides an addition parameter to enhance the sensitivity. In fact, increasing the q-factor solves jump-to-contact issues in that a very large q-factor allows for a very stiff cantilever (i.e., a large spring constant, k) and thus potentially very low oscillation amplitudes. This means that the cantilever will not react appreciably to impacts with the sample surface. This frequency modulation technique is also potentially less destructive of very delicate sample surfaces. Figure 6.7 is a scanning electron microscope image taken of a quartz crystal tunning fork sensor built in operate in FM mode.

6.2.3 Sensor Calibration for Imaging

Sensor / Surface Preparation

In traditional optics, an optical apparatus is calibrated by first characterizing the aperture with a point source and observing the aberration. The same logic is used in STM and AFM with the exception that as the scale of the measurement is reduced a standard source becomes questionable. As in optics, the final image is a convolution of the source with the response of the sensor [151] and so true calibration involves reducing the aberration incurred by the sensor to a simple function.

First, the scale of the sensor is established and characterized. The sensor used in my work is a platinum-iridium wire chosen because it is brittle and chemically inert. The wire is extruded to a fine point through controlled electrochemical etching. This procedure will reduce the resulting tip radius to $\approx$ 20 nm. Refer to figure 6.8 for an example of a good starting sensor geometry. The sensor is then transferred into the ultra-high vacuum microscopy environment, which was typically a base pressure of 1 x 10^{-10} Torr or better.

Once the tip is in vacuum it is cleaned via field emission. This is accomplished in two ways. Often the easiest method is to use a metallic sample surface as the anode. The advantage is that this method has a potentially short turn around time if this field emission step is done after imaging. This field emission step is used to remove adsorbates or native oxides from the sensor. Field emission to a surface will then transfer these

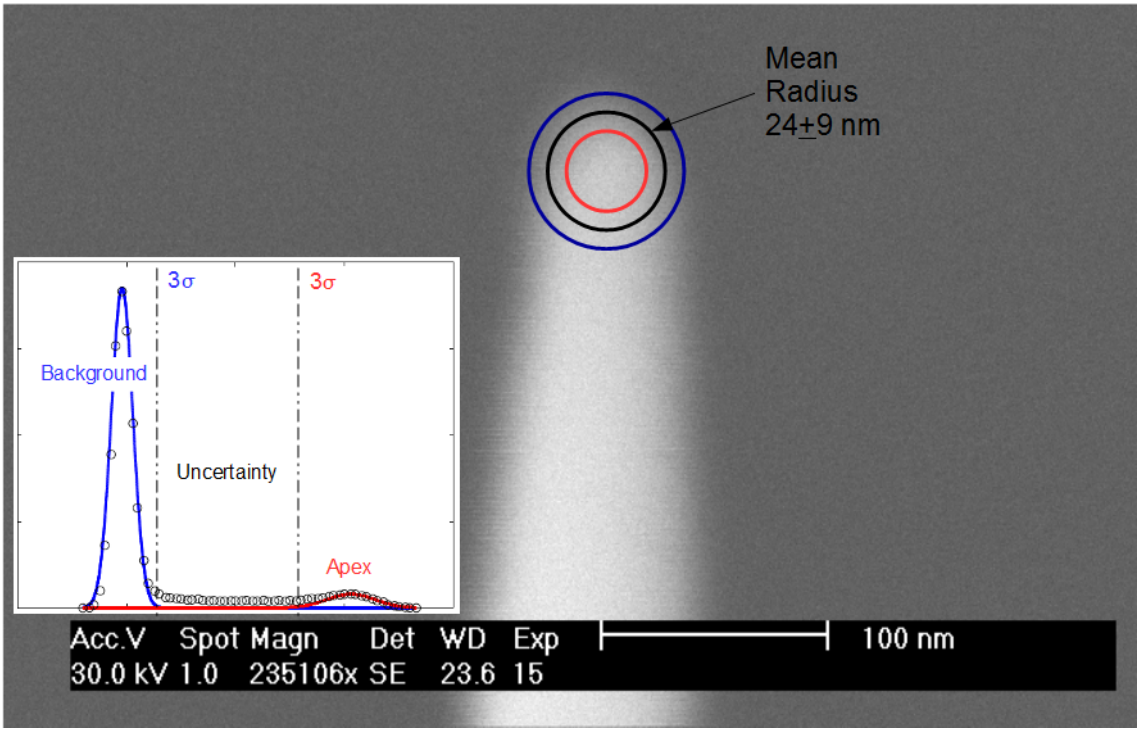

FIGURE 6.8: Scanning electron microscope image of an etched platinum-iridium wire constructed and imaged by the author for STM. The sensor radius was measured to be 24±9 nm which is the mean of the radii which include the uncertainty and exclude the apex. The edge of the apex can be distinguished as the uncertain or blurry region in the image. This region can be isolated from a histogram of the image (inset). Gaussian distributions represent the intensity of the background and apex. Three standard deviations from both distributions highlight the edge.

unwanted materials onto the anodic surface. Alternatively one can use a larger scale anode such as a ring. This step is difficult to monitor and must be done pro-actively to minimize this source of error.

Following this a clean gold surface was prepared by heating the gold until it is visually a bright orange in color. Heating the sample can be accomplished through Joule heating, thermal conduction or electron bombardment [157]. For my work. I chose to electron bombard the holder of the gold sample for less than a minute[11]. The gold (111) surface acts a imaging standard. Known properties of the gold (111) surface are measured and point-like features such as single adatoms are used to characterize the sensor. The scale of the sensor is established by withdrawing the sensor from the softer metallic surface under a 100 V bias. To accomplish this the sensor is lightly crashed into the surface then pulled away while monitoring the current. The withdrawal of the wire is evidenced by monitoring the gradual change in current as the sensor is pulled away. Abrupt uncontrollable changes in current from zero to some value are an indication of

[11] Any more can cause the gold to melt and thereby bead into a spherical surface which would make optical alignment virtually impossible.

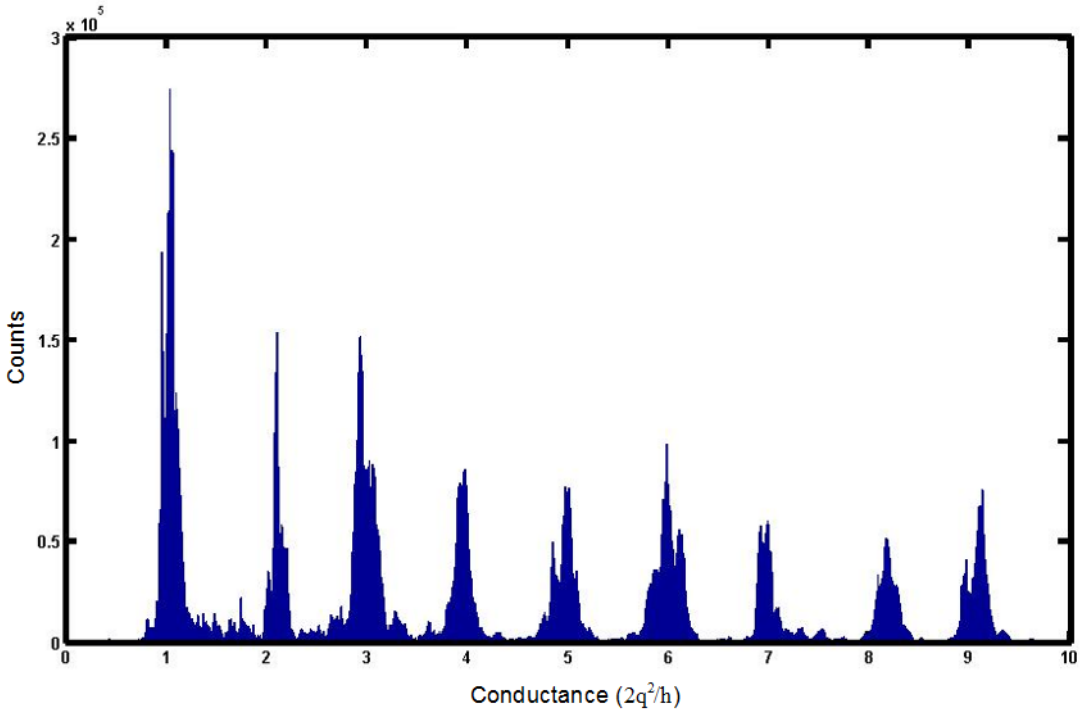

FIGURE 6.9: Histogram measured by the author of the conductance through a gold wire break junction. The envelope reflects the stability of the state. While there is a decrease in stability towards higher states, above $15(2q^2/h)$ conductance becomes nearly completely stable and quantization is not easily observed.

an effectively large radius tip while slow, gradual, controllable and reproducible changes indicate a sharp tip.

In performing this procedure, it is important to be aware that as the wire is drawn to a fine point the conductance is reduced. As the conductance approaches zero the decrease in conductance shifts from a classical continuum to discrete quanta. Consider figure 6.9 which shows the distribution of discrete quantum current states through a gold wire break junction [158]. In the quantum limit there is an apparent tendency to form a single conduction path rather than multiple conduction paths [159]. For a sensor, contacting that sensor to a softer metallic sample surface will alloy the sensor in the immediate vicinity of the point contact [160]. Thus, under an applied current, a careful disconnection of the sensor from the surface is expected to produce a cone-like structure ideally having a single atom at the apex. Under an applied electric field the tip can be thought of as a Schottky emitter where the field is strongest at the apex. This would then decrease the Fermi level at the apex with respect to the bulk of the sensor. For strong field gradients, atoms from the bulk surface can be transported toward this apex thereby 'sharpening' out a tip [161]. In practice, a controlled extrusion at 1 kV and 1 μA will yield tip radii on the order of 1Å given a starting radius of ≈ 20 nm.

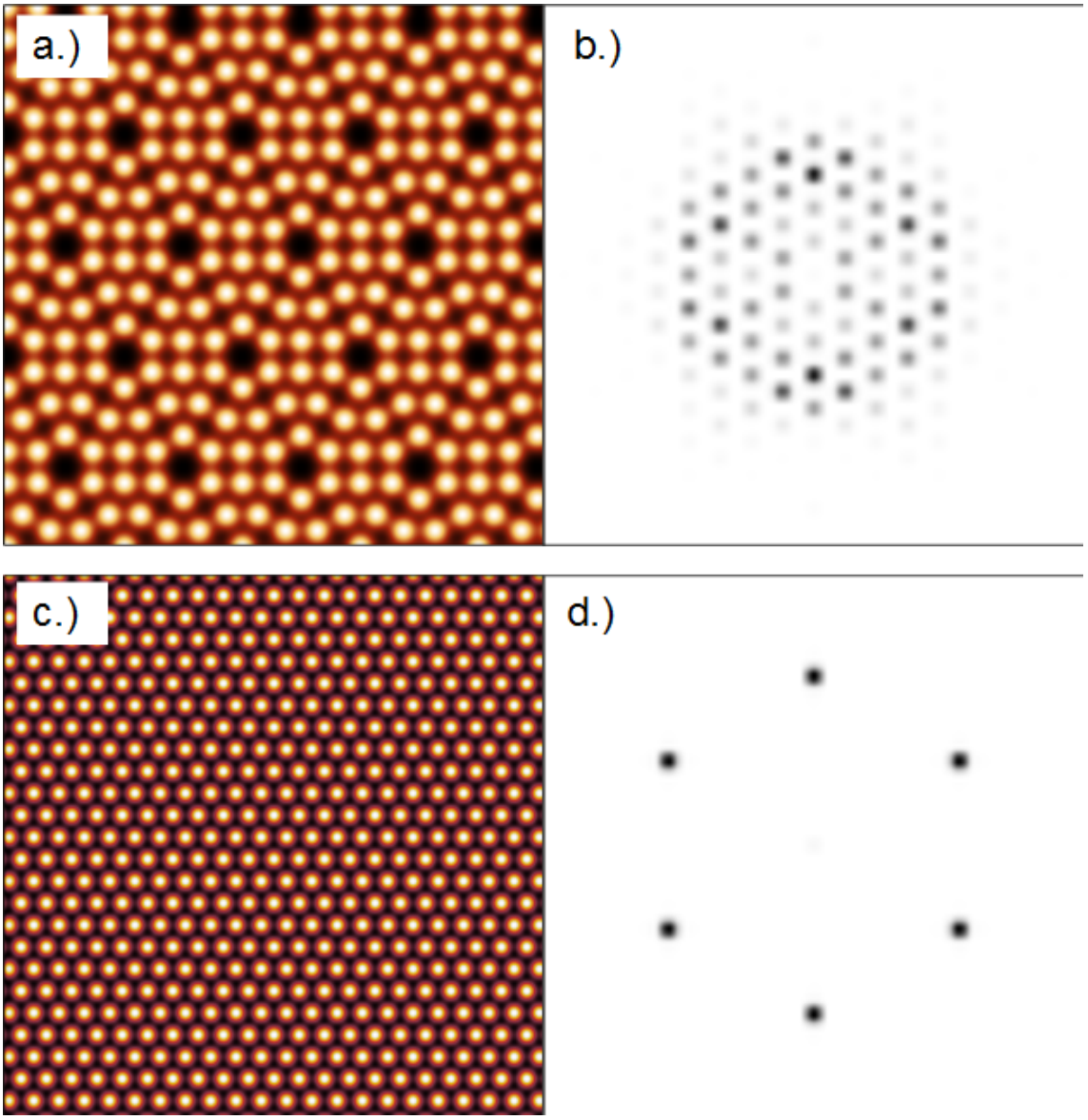

FIGURE 6.10: a.) Simulation (256 x 256 pixel), computed by the author, of the silicon (111) 7 x 7 reconstructed lattice (11 nm x 11 nm). b.) The resulting two-dimensional fast Fourier transformation of the Si (111) 7 x 7 lattice (23.3 nm^{-1} x 23.3 nm^{-1}). c.) Simulation computed by the author of the gold (111) (6.1 nm x 6.1 nm) lattice. At this scale surface reconstruction is not always visible. d.) The resulting two-dimensional fast Fourier transformation of the gold (111) lattice (41.7 nm^{-1} x 41.7 nm^{-1}). The darkest spots in figures b. and d. represent an average of the periodicity in that direction from the center. In these simulations Gaussian distributions have been used in place of the spherical distributions of the atom shape for analytical simplicity in the Fourier fitting.

Sample / Sensor Characterization

For calibration at large scales chemically inert structures, typically oxides, work best. At large scales sample preparation is often trivial in that careful out-of-vacuum cleanliness is sufficient. Calibration at the atomic scale is very different. It is this regime which requires in vacuum heating. The silicon (111) and gold (111) surfaces are extensively used. Silicon (111) is reactive, making the surface difficult to image in poorly evacuated

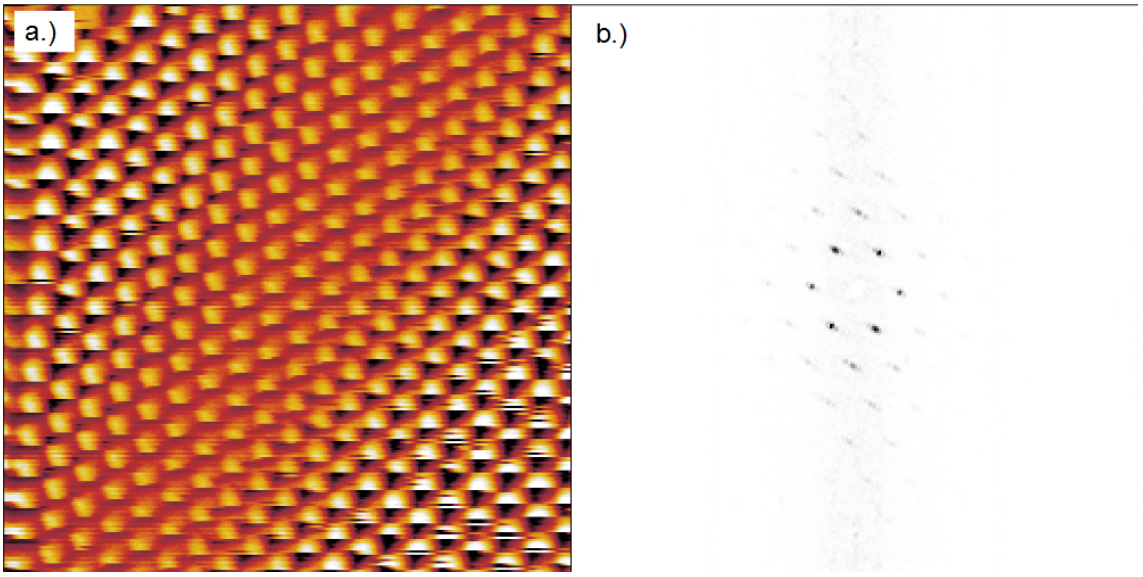

FIGURE 6.11: A.) STM measurement made using the Monash STM of the gold (111) (5 nm x 5 nm) lattice at 4K. B.) The two-dimensional fast Fourier transformation of the image (51.2 nm^{-1} x 51.2 nm^{-1}). More of the higher frequency spectrum is shown than in the simulated spectrum of figure 6.10D. Notice that there are faint higher frequency components (temporal noise) in the image coincident within a gray vertical stripe. This results form feedback error in the fast scan direction. The suggests that the sensor is essentially skipping off the atoms in scan. The calibration resulting from this measurement required a correction factor of 0.99 in fast scan direction.

environments. The 7 x 7 reconstructed surface provides a lower symmetry structure which provides immediate visual feedback of the image quality. The gold (111) surface is stable and is also prone to steps and defects that are useful in tip calibration. The surface reconstruction of gold[12] provides an excellent means of calibrating the sensor response normal to the surface.

Distance calibration is done by analysing the frequency spectrum of the image recorded by the sensor. For large scale measurements artificial periodic arrays suffice. At the atomic scale the atomic lattice is used. Calibrating imaging feedback is best done with steep step edges either artificial or atomic for the respective scales. Calibrating lateral distances requires imaging a surface comprised of simple periodic structures. It is important that pixel size of the image properly measures the surface according to the the Nyquist–Shannon sampling theorem. Consider a periodic array of objects equally spaced with spatial frequency k, then, according to this theorem the image of this array can be resolved given there is a pixel for every $\frac{1}{2k}$ of the image. The Nyquist–Shannon sampling theorem places a limit on the number of pixels required to measure a given structure. Indeed, measurements at or near this limit are not fully resolved. Calibration measurements should then be preformed far from this limit.

[12]This is the gold herringbone surface structure.

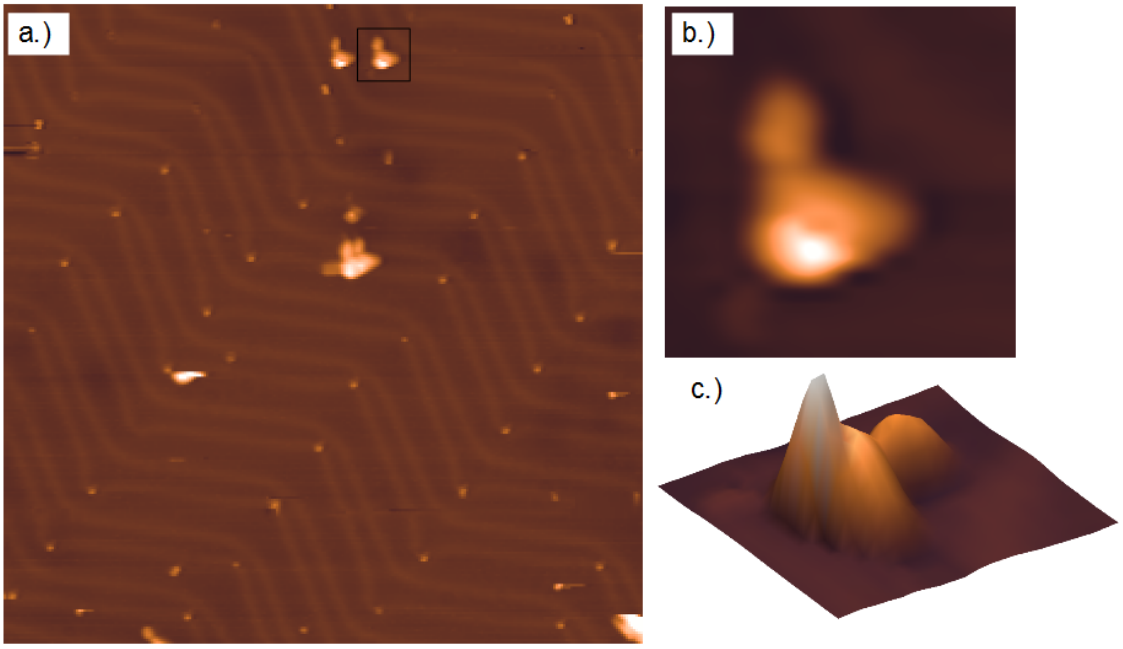

FIGURE 6.12: a.) Measurement made by the author of the gold (111) lattice at 4K (75 nm x 75 nm). b.) An enlargement (6.7 nm x 6.7 nm) of the motif which is convolved throughout the image. c.) A three-dimensional rendering of the same motif which represents the sensor apex. The height was measured at 80 nm some of which is due to feedback.

It is important to model the structure being imaged to get a precise handle on the error incurred from a particular calibration technique. For example, the simulation shown in figure 6.10c places a maximum precision of four significant figures on the lattice parameters at the relative scale shown. At large scales four-fold symmetric arrays with mostly four-fold symmetric motifs are often used. This makes Fourier analysis trivial. At the atomic scale lattice motifs can be quite complex when surface reconstruction is present such as in the case of Si (111), see figure 6.10a. For this reason surfaces with simple hexagonal lattice structure are preferred since the peaks in the frequency spectrum are easier to measure and interpret.

Once distance calibration is complete the sensor sample system must be fine tuned. This procedure is best accomplished by scanning over single adsorbates or defects across a large range. This type of measurement will reveal the degree with which the sensor structure is convolved with the surface structure. Repeating motifs in the image (see figure 6.12) represent the shape of the sensor apex convolved with the defect at that point. These types of observations are commonly referred to as "double tip effects" [151]. As on can see in figure 6.12c the sensor can be quite sharp at one scale and not as much at a larger scale. When these effects dominate the image, one must recondition the sensor before further measurement. In addition to the methods described above,

reconditioning can be as simple as pulsing the bias voltage across between the sensor and sample[13].

6.2.4 Local Density of States

From equation 6.7 one can see that the local density of states (LDOS) is proportional to the differential conductance, i.e.,

$$D(\mathbb{E}) \propto (dI/dV_{Bias}) \tag{6.25}$$

Measuring the LDOS allows one to separate electronically dependent structure from geometric structure. Calibration for a metalic LDOS measurement can be performed on the gold (111) surface. Gold is a noble metal with a nearly free two-dimensional electron gas having a parabolic dispersion [162]. The gold (111) surface reconstructs after annealing into fcc and hcp domains (see the profile inset of figure 6.13) forming rows in a herringbone pattern. The narrower hcp domains form ridges which appear to be 165 pm higher than the wider fcc regions. These hcp ridges are formed by bridge site atoms. Taking a differential conductance profile normal to the rows (the black line in figure 6.13a) reveals the onset of an sp derived surface state at around 500 meV [14]. The differential conductance map in figure 6.13 was taken along the black line and directly reflects the surface LDOS.

Calibration for a semiconducting LDOS measurement would ideally be performed on a known semi-conducting surface such as gallium arsenide [15]. Calibration is impotant to ensure that the sensor is not behaving as a semiconductor at the desired energy scales of the measurement of the sample. For the measurements presented in the following section a suitable calibration on a known semiconductor was not possible at the time. Prior to all those measurements, only a calibration as described previously to the gold (111) surface was performed.

6.3 Preliminary to Device Measurement

At this point, my goal has been to measure devices made from low dimensional crystals such as graphene and layered dichalcogenides. To that end, the first step was to understand the crystal in a three dimensional bulk. Next, the crystal was reduced to its two

[13]The experimenter must rely on knowledge of the sensor and sample materials to properly pulse the bias

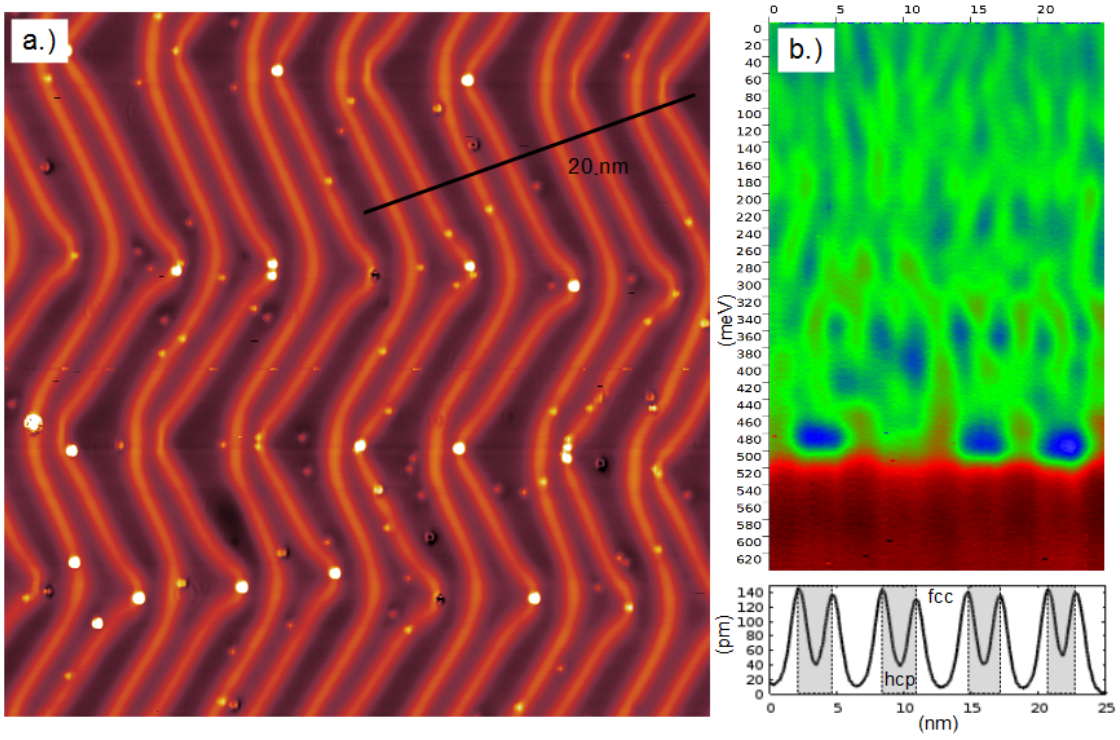

FIGURE 6.13: a.) Height image (50 nm x 50 nm) of the gold (111) surface at 4K taken using the Monash STM. The herringbone pattern is due to (22 x $\sqrt{3}$) surface reconstruction. b.) dI/dV measurement along the 25 nm black line in a. measured in 1.25 meV increments with a 20 mV bias modulation at 1,423 Hz. The ripples seen in the vertical direction above 520 meV could be attributed to barrier resonances. The height profile along the black line is below highlighting the fcc and hcp regions. This type of measurement follows closely the work presented in reference [14] and was used as a routine check of the tip quality for LDOS measurements.

dimensional state (this is one mono-layer). Then finally, a device would be constructed from the 2-D crystal. In each step success was defined as obtaining a clear atomically resolved image of the surface with a LDOS measurement distinguishing the pristine state from a defected state. A part of this process involves understanding how to prepare the surface reproducibly.

6.3.1 Bulk MoS_2

In the first step, a bulk molybdenum disulphide surface was prepared in UHV by annealing in vacuum at 100 C for an hour. The sample surface was then scanned repeatedly until the surface could be clearly imaged. A series of height images was taken shown in figure 6.14[14]. As the bias voltage is varied from negative to positive the measured shape of the defects change. On close inspection at high positive and negative bias (±1.5 V) atomic resolution is observed which is then lost in the intermediate voltages.

[14]Imaging delicate surfaces like MoS_2 is tricky since high annealing temperatures can not be used to prepare the surface. Often, the surface must be swept clean by the sensor and then the sensor must be re-prepared

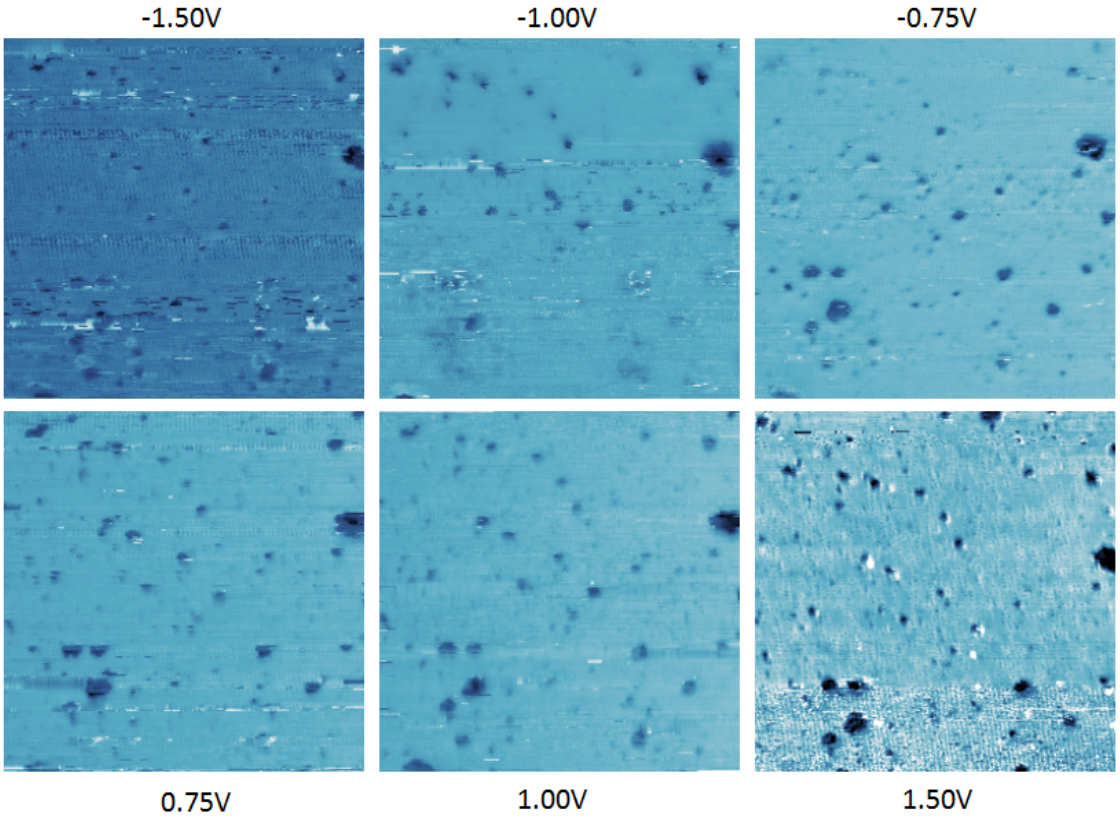

FIGURE 6.14: Consecutive height images (80 nm x 80 nm) of single crystal molybdenum disulphide at 4K made using the Monash instrument. The respective bias voltages are labelled above and below each image. A slight drift can be observed due to the time required to take each image.

Surface states are expected to be extremely sensitive to adsorbates and other defects. For gold, the identification of the surface position is a little easier than for a semiconductor which has an off state. The direct band gap of MoS_2 makes measurements near the band edge difficult. From equation 6.7 the tunneling current is exponentially proportional to the tunnelling gap. Thus, depending on the sensor-to-sample distance stability, the bias voltage can be reduced to a corresponding arbitrarily small value relative to the band edge, so long as the sensor-to-sample distance is reduced to compensate for the drop in tunnelling current [15]. The resulting set of tunnelling spectra (figure 6.15A, B) can be normalized by the corresponding change in sensor distance through equation 6.7. The result is a collapsed series of I-V curves (figure 6.15C) spanning a high dynamic range. Figure 6.16 shows how the abrupt changes in the slope of the normalized I-V curve can identify donor states at the surface [15].

The crater-like defects observed in figure 6.14 have an apparent sub-Ångström depression suggesting they may result from surface reconstruction, see figure 6.17. When these defects are imaged at the donor impurity state level, where conduction is minimized (detailed in figure 6.16(left)), they appear to have fewer states than the surrounding

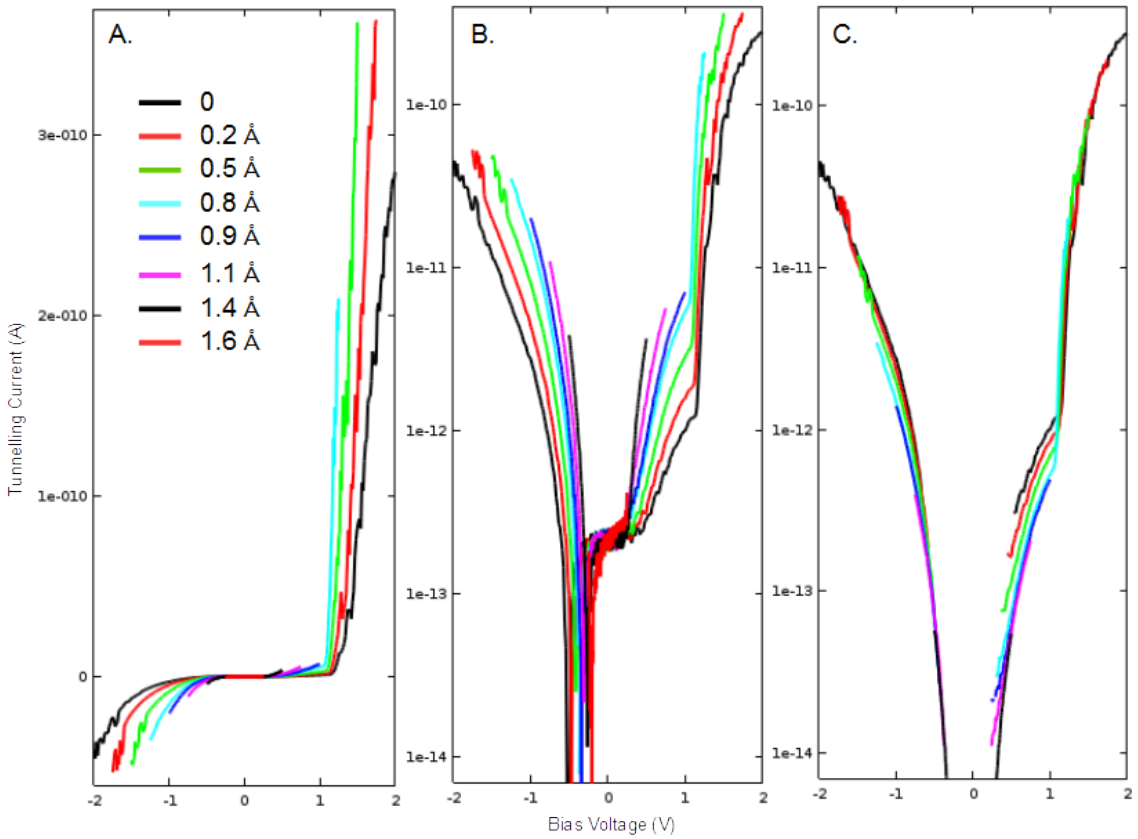

FIGURE 6.15: A) I-V curves taken at different heights. B) The absolute value of the same set of I-V curves in semi-log scale. C) The I-V curves of B normalized by their relative heights. Note that the un-normalized current is noise limited just above 1 x 10^{-13} A, whereas, the normalized current measures below 1 x 10^{-14} A yielding a dynamic range over four orders of magnitude.

area, see figure 6.18. At larger negative bias, which corresponds to imaging in the conduction band, these defected areas are instead enhanced. This suggests that the defected regions act like electron traps until the bias potential is below the trapping potential at which point the conduction is enhanced.

The apparent surface reconstruction being an explanation for the crater-like defects could result entirely from point-like sulphur vacancies [163]. The regions may also represent a qusai-polytype phase separation causing more of a lattice distortion in the region of defects rather than true domains.

6.3.2 Monolayer WS_2

Measuring lower dimensional crystals requires more preparation in that single layer crystals are like single monolayers of adsorbates. More care must be used to maintain the crystal's integrity across many heating cycles during sample preparation. In this

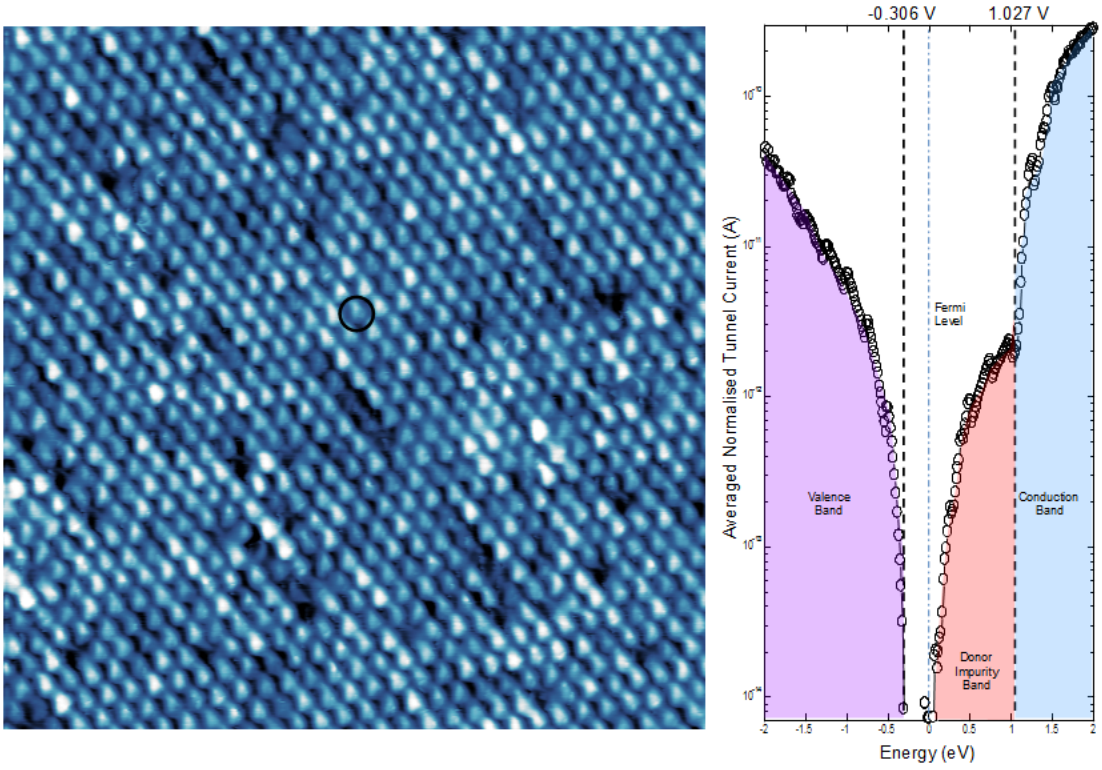

FIGURE 6.16: (Right) High dynamic (HD) range I-V measurement [15] of molybdenum disulphide at 4K taken on the Monash instrument. The measurement was taken at the encircled point in the image on the left (10 nm x 10 nm). This result appeared to vary little across the image shown on the left. The color segregation is a guide for the eye.

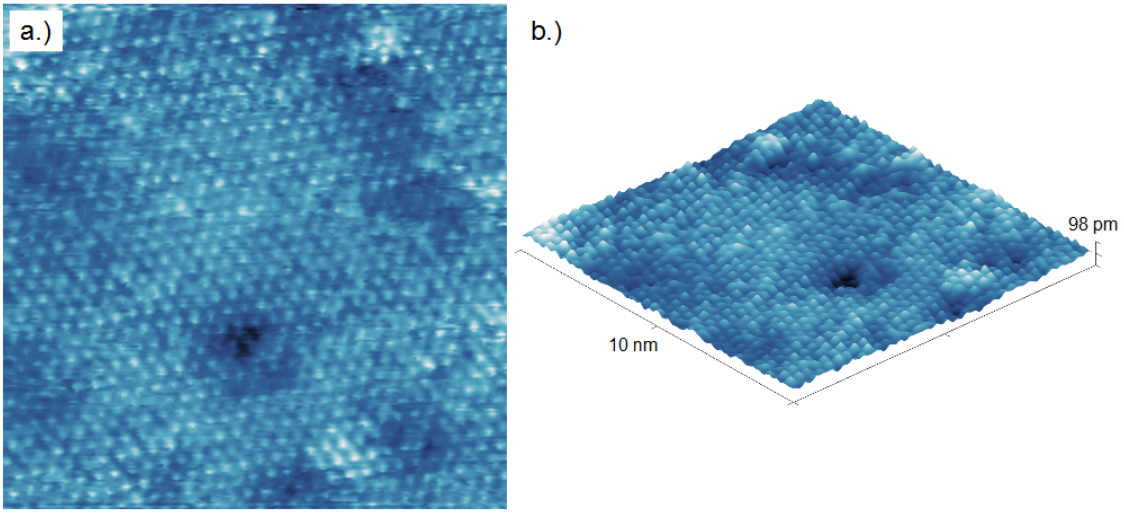

FIGURE 6.17: a.) Atomically resolved STM image (10 nm x 10 nm) taken using the Monash instrument at 4K around one of the "crater" defects seen in figure 6.14. b.) Three-dimensional rendering of the same image.

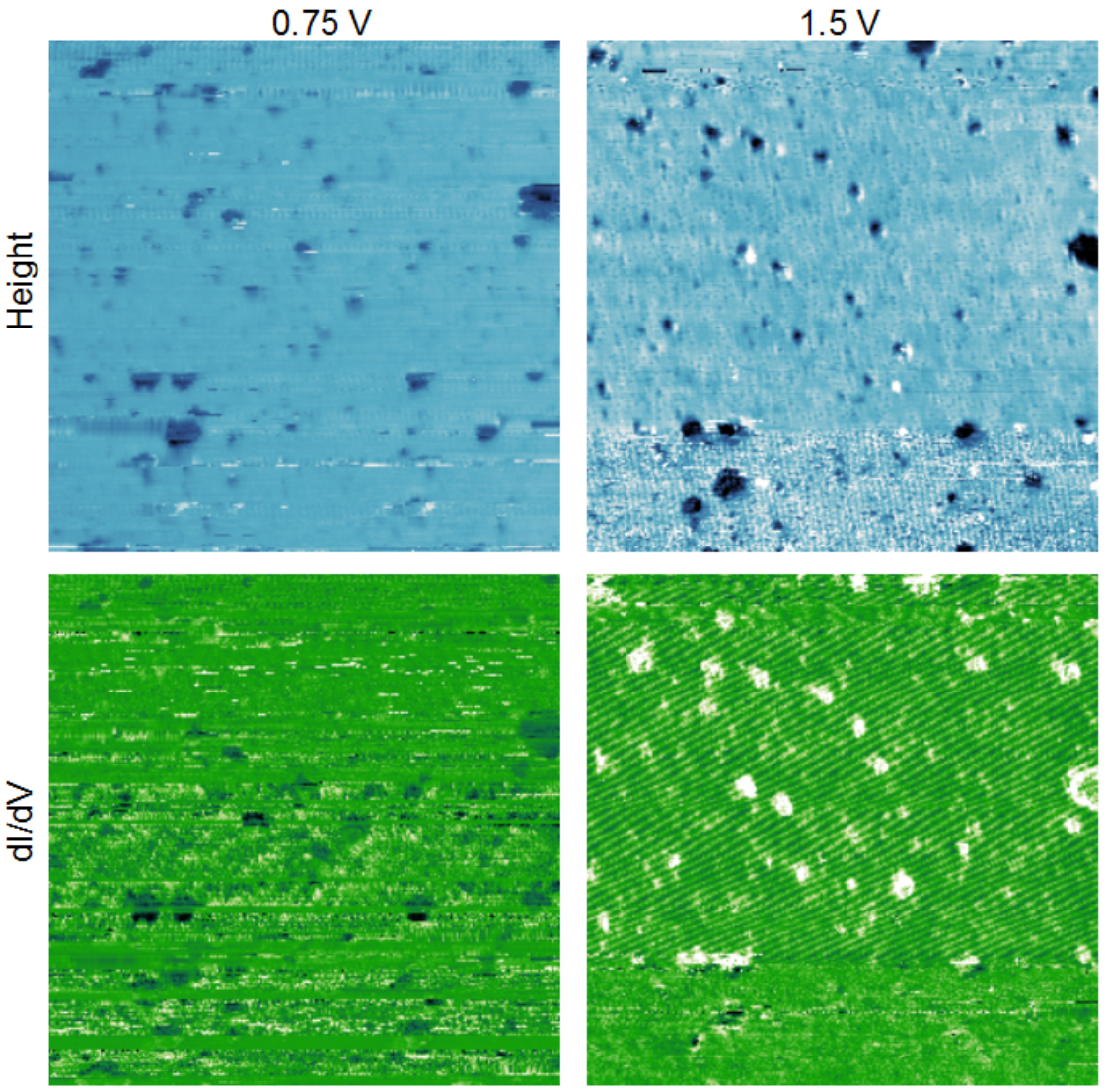

FIGURE 6.18: 80 nm x 80 nm Height images (blue) and the corresponding dI/dV maps (green)

next step, monolayer tungsten disulphide crystals were grown on sapphire substrates via chemical vapor deposition.

These crystals begin growth at random nucleation sites across the substrate. The growth was continued until the substrate was covered, though gaps typically remain as shown in figure 6.19B. This discontinuity is hazardous to an STM sensor which can only image a conducting surface. To add to this, annealing in UHV (75^oC for one hour) was done at a lower temperature to prevent against sample decomposition. Consequently, the surfaces were observed to be markedly "dirtier" preventing atomically resolved imaging.

All measurements began in AFM mode since the potentially "dirty" poorly conducting, semiconducting or insulating surface of the WS_2 can still be imaged by AFM measurements. Images often appeared as noise with only the suggestion, to the trained eye, of

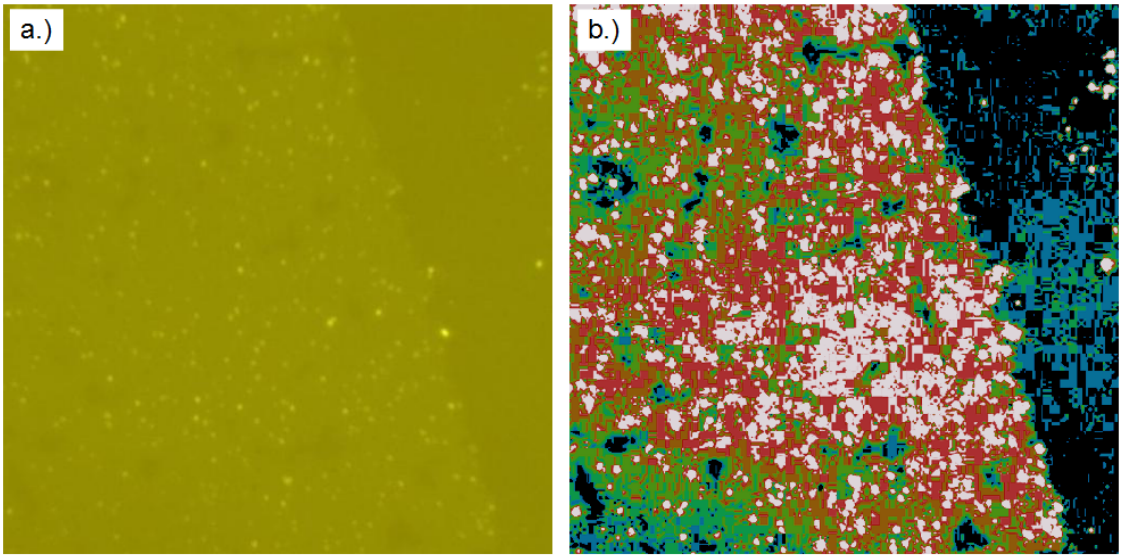

FIGURE 6.19: a.) Optical reflective bright field image (75 μm x 75 μm, 100X, 0.9 NA) of a sapphire substrate fully covered by monolayer WS_2 grown as described in the text. A region in the right of this image has been scratched away to measure the substrate contrast. b.) Same image as on the left with false coloring to highlight the coverage. Black regions are more than one standard deviation below the mean intensity. Black and blue regions indicate probable holes in the coverage. White regions are more than one standard deviation above the mean intensity and indicate probable multilayer growth.

surface structure. Optical bright field images such as figure 6.19 were first taken to understand the coverage. Imaging the surface in optical bright field allows an estimate of the location of covered regions suitable for imaging. Figure 6.19b shows holes in the coverage of monolayer tungsten disulphide after growth on a sapphire substrate. In addition to holes multilayer regions also form. The quality of this surface is first characterized by measuring the photoluminescence of the semiconductor, see figure 6.20.

Gold electrodes were then thermally deposited onto the surface to provide electrical continuity. Due to the multi layer growth large conductive regions for imaging were not easy to find. However, tunnelling spectroscopy near the gold electrodes did suggest that this type of sample was heavily doped with donors and acceptors, as suggested in figure 6.20b. The differential conductance (figure 6.20c), too, suggests a narrow gap and a non-zero density of states near this gap region. In both the I-V measurement and the (dI/dV) measurement the Fermi level sits in the middle of the gap indicating the material is naturally in an off state. That may be the reason for the extreme difficulty of imaging the surface at any appreciable distance from the electrode.

Future work will involve the production of complete monolayer devices. Such a device must have a source, drain and gate electrode. The gate electrode will increase the feasibility of tunnelling measurements. In addition to WS2 monolayers, the chalcogenides

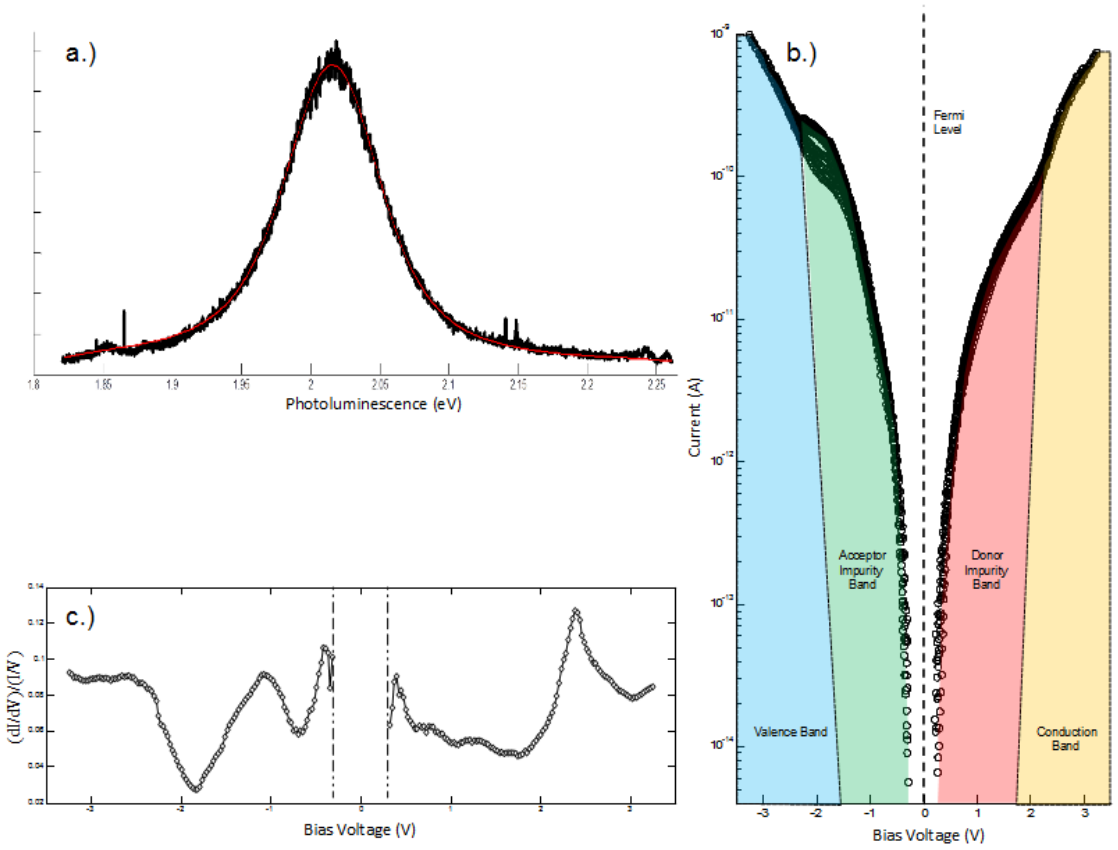

FIGURE 6.20: a.) (Black) Photoluminescence of WS_2 measured using the Monash STM with a 2.331 eV excitation energy at 10 mW and a spot size of $\approx 1\mu$m. (Red) Voigt distribution fit which yielded a Lorentzian lifetime of 144fs with a 20 meV broadening centred at 2.019 eV. b.)Normalized I-V curve showing the existence of donor and acceptors states. The presence of impurities obscuring the expected 2 eV band gap indicates poor surface quality. The color segregation in a guid for the eye. c.) Example of the differential conductance of the surface.

offer a large number of layered materials to explore. To this, as eluded to in chapter 5, there is bound to be emergent similarities among these materials yet to be discovered.

Bibliography

[1] A. C. Ferrari, J. C. Meyer, V. Scardaci, C. Casiraghi, M. Lazzeri, F. Mauri, S. Piscanec, D. Jiang, K. Novosolov, S. Roth, and A. K. Geim, Phys. Rev. Lett. **97**, 187401 (2006).

[2] E. Voloshina, R. Ovcharenko, A. Shulakov, and Y. Dedkov, The Journal of Chemical Physics **138**, 154706 (2013).

[3] D. C. Mason, D. M. Mintz, and A. Kuppermann, Review of Scientific Instruments **48**, 926 (1977).

[4] Y. C. Chou, M. J. Robrecht, and B. P. Tonner, Rev. Sci. Instrum. **58**, 1164 (1987).

[5] S. Stankovich, R. D. Piner, X. Chen, N. Wu, S. T. Nguyen, and R. S. Ruoff, J. Mater. Chem. **16**, 155 (2006).

[6] C. Deng, W. Lin, G. Agnus, D. Dragoe, D. Pierucci, A. Ouerghi, S. Eimer, I. Barisc, D. Ravelosona, C. Chappert, and W. Zhao, J. Phys. Chem. C. **118**, 13890 (2014).

[7] P. Merino, M. Svec, J. I. Martinez, P. Jelinek, P. Lacovig, M. Dalmiglio, S. Lizzit, P. Soukiassian, J. Cemicharo, and J. A. Martin-Gago, Nat.Comm. **5**, 503 (2014).

[8] S. Ohmagari, T. Yoshitake, A. Nagano, S. AL-Riyami, R. Ohtani, H. Setoyama, E. Kobayashi, and K. Nagayama, Journal of Nanomaterials **2009**, 876561 (2009).

[9] Y. Muramatsu, E. M. Gullikson, and R. C. C. Perera, Physica Scripta. **T115**, 501 (2005).

[10] U. Hofer, I. L. Shumay, C. Reuss, U. Thomann, W. Wallauer, and T. Fauster, Science **277**, 1480 (1997).

[11] A. Frye, *Defect induced electrical/optical properties of $SrTiO_{3-x}$ (001) by photo-assisted tunnelling spectroscopy*, Ph.D. thesis (1999).

[12] J. G. Simmonos, J. Appl. Phys. **34**, 2581 (1963).

[13] S. Morita, R. Wiesendanger, and E. Meyer, *Noncontact Atomic Force Microscopy* (Springer-Verlag, 2002).

[14] L. Burgi, H. Brune, and K. Kern, Physical Review Letters **89**, 17 (2002).

[15] R. M. Feenstra and J. A. Stroscio, Journal of Vacuum Science and Technology B **5**, 923 (1987).

[16] M. A. Van Hove and S. Y. Tong, *The Structures of Surfaces* (Springer-Verlag, 1985).

[17] W. Monch, *Semiconductor Surfaces and Interfaces* (Springer-Verlag, Berlin, 1993) pp. 221–3.

[18] E. H. Lock, M. Baraket, M. Laskoski, S. P. Mulvaney, W. K. Lee, P. E. Sheehan, D. R. Hines, J. T. Robinson, J. Tosado, M. S. Fuhrer, S. C. Hernandez, and S. G. Walton, Nano Lett. **12**, 102 (2012).

[19] J. Tosado, A. Tadich, M. Edmonds, J. Reutt-Robey, and M. S. Fuhrer, "Formation and analysis of graphene vacancies via xps and nexafs measurements," To be submitted.

[20] A. K. Geim and K. S. Novosolov, Nat. Mat. **6**, 182 (2007).

[21] V. Palenskis, World Journal of Condensed Matter Physics **3**, 3 (2013).

[22] K. S. Novoselov, A. K. Geim, S. V. Morozov, D. Jiang, M. I. Katsnelson, I. V. Grigorieva, S. V. Dubonos, and A. A. Firsov, Nature **438**, 197 (2005).

[23] S. V. Morozov, K. Novoselov, M. Katsnelson, F. Schedin, D. Elias, J. Jaszczak, and A. Geim, Phys. Rev. Lett. **100**, 016602 (2008).

[24] J. H. Chen, C. Jang, S. Xiao, M. Ishigami, and M. S. Fuhrer, Nature Nanotechnology **3**, 206 (2008).

[25] S. Cho and M. S. Fuhrer, Phys. Rev. B **77**, 081402 (2008).

[26] Y. Zhang, V. W. Brar1, C. Girit1, A. Zettl, and M. F. Crommie, Nat. Phys. **5**, 722 (2009).

[27] C. R. Dean, A. F. Young, I. Meric, C. Lee, L. Wang, S. Sorgenfrei, K. Watanabe, T. Taniguchi, P. Kim, K. L. Shepard, and J. Hone, Nat. Nano Tech. **5**, 722 (2010).

[28] L. Banszerus, M. Schmitz, S. Engels, J. Dauber, M. Oellers, F. Haupt, K. Watanabe, T. Taniguchi, B. Beschoten, and C. Stampfer, Sci. Adv. **1**, e1500222 (2015).

[29] S. Deng and V. Berry, Materials Today **19**, 197 (2016).

[30] J. N. Grima, S. Winczewski, L. Mizzi, M. C. Grech, R. Cauchi, R. Gatt, D. Attard, K. W. Wojciechowski, and J. Rybicki, Advanced Materials **27**, 1455 (2014).

[31] I. V. Fialkovsky and D. V. Vassilevich, International Journal of Modern Physics A **27**, 15 (2012).

[32] F. Ortmann, S. Roche, S. O. Valenzuela, and L. W. Molenkamp, *Topological Insulators: Fundamentals and Perspectives* (Whiley-VHC Verlag GmbH and Co. KGaA, 2015).

[33] A. Jorio, M. Dresselhaus, R. Saito, and G. Dresselhaus, *Raman Spectroscopy in Graphene Related Systems* (Wiley-VCH Verlag GmbH & Co. KGaA, 2011).

[34] P. Delhaes, *Graphite and Precursors* (Gordon and Breach Science Publishers, 2001) pp. 27–31.

[35] P. R. Wallace, Phys. Rev. **71**, 622 (1947).

[36] R. Saito, G. Dresselhaus, and M. S. Dresselhaus, *Physical Properties of Carbon Nanotubes* (Imperial College Press, 1998) pp. 23, 27.

[37] A. H. Castro Neto, F. Guinea, N. M. R. Peres, K. S. Novoselov, and A. K. Geim, Rev. Mod. Phys. **81**, 109 (2009).

[38] N. J. Turro, J. S. Scaiano, and V. Ramamurthy, *Principles of Molecular Photochemistry: an Introduction* (University Science Books, 1st Edition, 2009) pp. 63–6.

[39] S. Das Sarma, S. Adam, E. H. Hwang, and E. Rossi, Rev. Mod. Phys. **83**, 407 (2011).

[40] T. Stauber, N. M. R. Peres, and F. Guinea, Phys. Rev. B **76**, 205423 (2007).

[41] A. W. W. Ludwig, M. P. A. Fisher, R. Shankar, and G. Grinstein, Phys. Rev. B **50**, 7526 (1994).

[42] E. H. Hwang, S. Adam, and S. Das Sarma, Phys Rev Lett. **98**, 186806 (2007).

[43] J. H. Chen, C. Jang, S. Adam, M. S. Fuhrer, E. D. Williams, and M. Ishigami, Nat. Lett. **4**, 377 (2008).

[44] K. Hess, *Advanced Theory of Semiconductor Devices* (John Wiley and Sons, Inc., 2000) p. 96.

[45] L. Tapaszto, G. Dobrik, P. Nemes-Incze, G. Vertesy, P. Lambin, and L. P. Biro, Phys. Rev. B **78**, 233407 (2008).

[46] B. Krauss, T. Lohmann, D.-H. Chae, M. Haluska, K. von Klitzing, and J. H. Smet, Phys. Rev. B **79**, 165428 (2009).

[47] J. H. Chen, W. G. Cullen, C. Jang, M. S. Fuhrer, and E. D. Williams, Phys. Rev. Lett. **102**, 680501 (2009).

[48] J. H. Chen, L. Li, W. G. Cullen, E. D. Williams, and M. S. Fuhrer, Nat. Phys. **7**, 535 (2011).

[49] D. C. Kim, D.-Y. Jeon, H.-J. Chung, Y. S. Woo, J. K. Shin, and S. Seo, Nanotechnology **20**, 375703 (2009).

[50] Y. B. Zhou, Z. M. Liao, Y. F. Wang, G. S. Duesberg, J. Xu, Q. Fu, X. S. Wu, and D. P. Yu, J. Chem. Phys. **133**, 234703 (2010).

[51] G. Buchowicz, P. R. Stone, J. T. Robinson, C. D. Cress, J. W. Beeman, and O. D. Dubon, Appl. Phys. Lett. **98**, 032102 (2011).

[52] G. Liu, D. Teweldebrahn, and A. A. Balandin, IEEE Trans. Nanotechnol. **10**, 865 (2011).

[53] S. Nakaharai, T. Iijima, S. Ogawa, S. Suzuki, S.-L. Li, K. Tsukagoshi, S. Sato, and N. Yokoyama, ACS Nano **7**, 5694 (2013).

[54] R. R. Nair, I.-L. Tsai, M. Sepioni, O. Lehtinen, J. Keinonen, A. V. Krasheninniov, A. H. C. Neto, M. I. Katsnelson, A. K. Geim, and I. V. Grigorieva, Nat. Comm. **4**, 2010 (2013).

[55] S. Ichinokura, K. Sugawara, T. T. A. Takayama, and S. Hasegawa, ACS Nano **10**, 2761 (2016).

[56] C. Gomez-Navarro, R. T. Weitz, A. M. Bittner, M. Scolari, A. Mews, M. Burghard, and K. Kern, Nano Letters **7**, 3499 (2007).

[57] J. O. Sofo, A. S. Chaudhari, and G. Barber, Physical Review B **75**, 153401 (2007).

[58] M. M. Lucchese, F. Stavale, E. H. M. Ferreira, C. Vilani, M. V. O. Moutinho, R. B. Capaz, C. A. Achete, and A. Jorio, Carbon **48**, 1592 (2010).

[59] A. Das, S. Pisana, B. Chakraborty, S. Piscanec, S. K. Saha, U. V. Waghmare, K. S. Novosolov, H. R. Krishinamurthy, A. K. Beim, A. C. Ferreri, and A. K. Sood, Nat. NanoTech. **3**, 210 (2008).

[60] Y. Zhang, L. Zhang, and C. Zhou, Acc. Chem. Res. **46**, 2329–39 (2013).

[61] D. Graf, F. Molitor, K. Ensslin, C. Stampfer, A. Jungen, C. Hierold, and L. Wirtz, Nano Lett. **7**, 238 (2007).

[62] V. P. Verma, S. Das, I. Lahiri, and W. Choi, Appl. Phys. Lett. **96**, 203108 (2010).

[63] K. S. Kim, Y. Zhao, H. Jang, S. Y. Lee, J. M. Kim, K. S. Kim, J.-H. Ahn, P. Kim, J.-Y. Choi, and B. H. Hong, Nature **457**, 706 (2009).

[64] J. W. Suk, A. Kitt, C. W. Magnuson, Y. Hao, S. Ahmed, J. An, A. K. Swan, B. B. Goldberg, and R. S. Ruoff, ACS Nano **5**, 6916 (2011).

[65] D. A. Shirley, Phys. Rev. B **5**, 4709 (1972).

[66] S. Doniach and M. Sunjic, J. Phys. C: Solid St. Phys. **3**, 285 (1970).

[67] V. Despoja and M. Sunjic, Phys. Rev. B **88**, 245416 (2013).

[68] T. A. Carlson, Physics Today **25**, 30.

[69] T. A. Carlson, *Photoelectron and Auger Spectroscopy* (Plenum Press, New York, 1975).

[70] M. Newville, *Fundamentals of XAFS* (Consortium for Advanced Radiation Sources University of Chicago, Chicago, IL, 2004).

[71] J. Moscovoci, G. Loupias, P. Parent, and G. Tourillon, J. Phys. Chem. Solids **57**, 1159 (1996).

[72] J. A. Horsley, J. Stöhr, and R. J. Koestner, J. Chem. Phys. **83**, 3146 (1985).

[73] H. Boersch, Journal of Electron Microscopy **16**, 39 (1967).

[74] J. Stöhr, *NEXAFS Spectroscopy* (Springer-Verlag, Berlin, 1992).

[75] F. Sette, J. Stöhr, and A. P. Hitchcock, J. Chem. Phys. **81**, 4906 (1984).

[76] D. Arvanitis, H. Rabus, L. Wenzel, and K. Babersehke, Z. Phys. D **11**, 219 (1989).

[77] D. A. Outka and J. Stöhr, Z. Phys. D **11**, 3539 (1988).

[78] J. A. Horsley, J. Chem. Phys. **76**, 1451 (1982).

[79] G. D. Mahan, Physical Review **163**, 3 (1967).

[80] P. M. T. M. van Attekum and G. K. Wertheim, Physical Review Letters **43**, 25 (1979).

[81] E. J. Mele and J. J. Ritsko, Physical Review Letters **43**, 1 (1979).

[82] J. A. Simpson, Rev. Sci. Instrum. **35**, 1698 (1964).

[83] V. D. Meyer, A. Skerbele, and E. N. Lassettre, J. Chem. Phys. **43**, 805 (1965).

[84] U. Amaldi Jr., A. Egidi, R. Marconero, and G. Pizzella, Review of Scientific Instruments **40**, 1001 (1969).

[85] D. W. Turner, Proc. R. Soc. A **307**, 15 (1968).

[86] A. L. Hughes and V. Rojansky, Phys. Rev. **34**, 284 (1929).

[87] E. M. Purcell, Phys. Rev. **54**, 818 (1938).

[88] T. A. Carlson and A. E. Jonas, J. Chem. Phys. **55**, 4913 (1969).

[89] B. P. Pullen, T. A. Carlson, W. E. Moddeman, G. K. Schweitzer, W. E. Bull, and F. A. Grimm, J. Chem. Phys. **53**, 768 (1970).

[90] B. P. Pullen, T. A. Carlson, W. E. Moddeman, G. K. Schweitzer, W. E. Bull, and F. A. Grimm, Faraday Discuss. Chem. Soc. **54**, 277 (1972).

[91] C. L. Allyn, T. Gustafsson, and E. W. Plummer, Rev. Sci. Instrum. **49**, 1197 (1978).

[92] H. Liebl, *Applied Charged Particle Optics* (Springer-Verlag, Berlin, 2008).

[93] G. V. Hansson, B. Goldberg, and R. Z. Bachrach, Rev. Sci. Instrum. **52**, 517 (1981).

[94] J. E. Pollard, D. J. Trevor, Y. T. Lee1, and D. A. Shirley, Rev. Sci. Instrum. **52**, 1837 (1981).

[95] D. DiChio, S. V. Natali, C. E. Kuyatt, and A. Galejs, Rev. Sci. Instrum. **45**, 566 (1974).

[96] C. E. Kuyatt, D. DiChio, and S. V. Natali, Rev. Sci. Instrum. **45**, 1275 (1974).

[97] A. Galejs and C. E. Kuyatt, J. Vac. Sci. Technol. **10**, 1114 (1973).

[98] C. E. Kuyatt, D. DiChio, and S. V. Natali, J. Vac. Sci. Technol. **10**, 1124 (1973).

[99] D. DiChio, S. V. Natali, and C. E. Kuyatt, Rev. Sci. Instrum. **46**, 71 (1975).

[100] S. Doukas, I. Madesis, A. Dimitriou, A. Laoutaris, T. J. M. Zouros, and E. P. Benis, Rev. Sci. Instrum. **86**, 043111 (2015).

[101] D. Ceolin, J.-O. Forsell, B. Wannberg, S. Legendre, J. Palaudoux, G. Ohrwall1, S. Svensson, and M. N. Piancastelli, Rev. Sci. Instrum. **81**, 063112 (2010).

[102] M. Dogan1, M. Ulu, G. G. Gennarakis, and T. J. M. Zouros, Rev. Sci. Instrum. **84**, 043105 (2013).

[103] D. Q. Hu and K. T. Leung, Rev. Sci. Instrum. **66**, 2865 (1995).

[104] H. Daimon, Rev. Sci. Instrum. **59**, 545 (1988).

[105] P. K. Chu and L. Li, Materials Chemistry and Physics **96**, 253 (2006).

[106] B. K. Tay, X. Shi, H. S. Tan, and D. H. C. Chua, Surface and Interface Analysis **20**, 231 (1999).

[107] R. Haerle, E. Riedo, A. Pasquarello, and A. Baldereschi, Physical Review B **65**, 045101 (2001).

[108] G. Comelli, J. Stohr, C. J. Robinson, and W. Jark, Physical Review B **38**, 11 (1988).

[109] M. Ramm, M. Ata, K.-W. Brzezinkab, T. Grossb, and W. Unger, Thin Solid Films **354**, 106 (1999).

[110] V. Despoja, M. Sunjic, and L. Marusic, Physical Review B **77**, 035424 (2008).

[111] J. L. Figueiredo, M. F. R. Pereira, M. M. A. Freitas, and J. J. M. Orfao, Carbon **37**, 1379 (1999).

[112] T. Susi, M. Kaukonen, P. Havu, M. Ljungberg, P. Ayala, and E. I. Kauppinen, Beilstein J. Nanotechnol. **5**, 121 (2014).

[113] D. Yang, A. Velamakanni, G. Bozoklu, S. Park, M. Stoller, R. D. Piner, S. Stankovich, I. Jung, D. A. Field, C. A. Ventrice Jr., and R. S. Ruoff, Carbon **47**, 145 (2009).

[114] M. Z. Hossain, J. E. Johns, K. H. Bevan, H. J. Karmel, Y. T. Liang, S. Yoshimoto, K. Mukai, T. Koitaya, J. Yoshinobu, M. Kawai, A. M. Lear, L. L. Kesmodel, S. L. Tait, and M. C. Hersam, Nat. Chem. **4**, 305 (2012).

[115] D. Wei, Y. Liu, Y. Wang, H. Zhang, L. Huang, and G. Yu, Nano Lett. **9**, 1752 (2009).

[116] R. Lv, Q. Li, A. R. Botello-Mendez, T. Hayashi, B. Wang, A. Berkdemir, Q. Hao, A. L. Elias, R. Cruz-Silva, H. R. Gutierrez, Y. A. Kim, H. Muramatsu, J. Zhu, M. Endo, H. Terrones, J.-C. Charlier, M. Pan, and M. Terrones, Sci. Rep. **2**, 586 (2012).

[117] A. Nikitin, H. Ogasawara, D. Mann, R. Denecke, Z. Zhang, H. Dai, K. Cho, and A. Nilsson, Phys. Rev. Lett. **95**, 225507 (2005).

[118] W. Zhao, S. M. Kozlov, O. Hofert, K. Gotterbarm, M. P. A. Lorenz, F. Vines, C. Papp, A. Gorling, and H.-P. Steinruck, J. Phys. Chem. Lett. **2**, 759 (2011).

[119] W. Zhao, J. Gebhardt, K. Gotterbarm, O. Höfert, C. Gleichweit, C. Papp, A. Görling, and H.-P. Steinrück, J. Phys.: Condens. Matter **25**, 445002 (2013).

[120] K. C. Prince, I. Ulrych, M. Peloi, and B. Ressel, Physical Review B **62**, 11 (2000).

[121] S. Lizzit, L. Petaccia, A. Goldoni, R. Larciprete, P. Hofmann, and G. Zampieri, Physical Review B **76**, 153408 (2007).

[122] A. B. Preobrajenski, M. L. Ng, A. S. Vinogradov, and N. Martensson, Physical Review B **78**, 073401 (2008).

[123] A. Gruneis, K. Kummer, and D. V. Vyalikh, New Journal of Physics **11**, 073050 (2009).

[124] A. Bagari, C. Mattevi, M. Acik, Y. J. Chabal, M. Chhowalla, and V. B. Shenoy, Nat.Chem. **2**, 581 (2010).

[125] M. J. Webb, P. Palmgren, P. Pal, O. Karis, and H. Grennberg, Carbon **49**, 3242 (2011).

[126] D. Ferrah, J. Penualas, C. Bottela, G. Grenet, and A. Ouerghi, Surface Science **615**, 47–56 (2013).

[127] K. V. Emtsev, A. Bostwick, K. Horn, J. Jobst, G. L. Kellogg, L. Ley, J. L. McChesney, T. Ohta, S. A. Reshanov, J. Röhrl, E. Rotenberg, A. K. Schmid, D. Waldmann, H. B. Weber, and T. Seyller, Nat.Mat. **8**, 203 (2009).

[128] R. J. Koch, M. Weser, W. Zhao, F. Vines, K. Gotterbarm, S. M. Kozlov, O. Höfert, M. Ostler, C. Papp, J. Gebhardt, H.-P. Steinrück, A. Göling, and T. Seyller, Phys.Rev. **86**, 075401 (2012).

[129] R. Rozada, J. I. Paredes, S. Villar-Rodi, A. Martinez-Alonso, and J. M. D. Tascon, Nano Research **6**, 216 (2013).

[130] R. A. Rosenberg, P. J. Love, and V. Rehn, Physical Review B **33**, 6 (1986).

[131] L. J. Terminello, D. K.Shuh, F. J. Himpsel, D. A. Lapiano-Smith, J. Stohr, D. S. Bethune, and G. Meijer, Chemical Physics Letters **182**, 5 (1991).

[132] D. A. Fischer, R. M. Wentzcovitch, R. G. Carr, A. Continenza, and A. J. Freeman, Physical Review B **44**, 3 (1991).

[133] J. Stohr, D. A. Outka, K. Baberschke, D. Arvanitis, and J. A. Horsley, Physical Review B **36**, 5 (1987).

[134] I. Shimoyama, Y. Baba, T. Sekiguchi, and K. Nath, Journal of Electron Spectroscopy and Related Phenomena **137**, 573 (2004).

[135] I. Jimenez, A. Jankowski, L. J. Terminello, J. A. Carlisle, D. G. J. Sutherland, G. L. Doll, J. V. Mantese, W. M. Tong, D. K. Shuh, and F. J. Himpsel, Applied Physics Letters **68**, 2816 (1996).

[136] S. Banerjee, T. Hemraj-Benny, M. Balasubramanian, D. A. Fischer, J. A. Misewichb, and S. S. Wong, Chemical Communication **7**, 772 (2004).

[137] T. Hemraj-Benny, S. Banerjee, S. Sambasivan, D. A. Fischer, W. Han, J. A. Misewich, and S. S. Wong, Physical Chemistry: Chemical Physics **7**, 1103 (2005).

[138] D. Pacile, M. Papagno, A. F. Rodriguez, M. Grioni, L. Papagno, C. O. Girit, J. C. Meyer, G. E. Begtrup, and A. Zettl, Phys. Rev. B **101**, 066806 (2008).

[139] A. Pirkle, J. Chan, A. Venugopal, D. Hinojos, C. W. Magnuson, S. McDonnell, L. Colombo, E. M. Vogel, R. S. Ruoff, and R. M. Wallace, Applied Physics Letters **99**, 122108 (2011).

[140] Y.-C. Lin, C.-C. Lu, C.-H. Yeh, C. Jin, K. Suenaga, and P.-W. Chiu, Nano Letters **12**, 414 (2011).

[141] F. Sette, G. K. Wertheim, Y. Ma, , G. Meigs, S. Modesti, and C. T. Chen, Physical Review B **41**, 14 (1990).

[142] X. Liu, T. Pichler, M. Knupfer, J. Fink, and H. Kataura, Physical Review B **70**, 205405 (2004).

[143] A. Bagri, C. Mattevi, M. Acik, Y. J. Chabal, M. Chhowalla, and V. B. Shenoy, Nature Chemistry **2**, 581 (2010).

[144] T. Balasubramanian, J. N. Andersen, and L. Wallden, Physical Review B **64**, 205420 (2001).

[145] T. R. Albrecht, P. Grutter, D. Horne, and D. Rugar, Journal of Applied Physics **69**, 668 (1991).

[146] P. Niedermann, R. Emch, and P. Descouts, Rev. Sci. Instrum. **59**, 368 (1988).

[147] S. H. Pan, E. W. Hudson, and J. C. Davis, Rev. Sci. Instrum. **70**, 1459 (1999).

[148] J. C. Fisher and I. Glaever, J. Appl. Phys. **32**, 172 (1961).

[149] J. Tersoff and D. R. Hamann, Physical Review B **31**, 2 (1985).

[150] J. Bardeen, Physical Review Letters **6**, 57 (1961).

[151] E. D. Bonnell, *Scanning Probe Microscopy and Spectroscopy: Theory, Techniques, and Application, Second Edition* (Wiley-VCH, 2001).

[152] J. A. Stroscio, R. M. Feenstra, and A. P. Fein, Phys. Rev. Lett. **57**, 2579 (1986).

[153] J. E. Jones, Proceedings of the Royal Society of London. Series A **106**, 441 (1924).

[154] F. London, Trans. Faraday Soc. **33**, 8 (1936).

[155] J. E. Jones, Proc. Phys. Soc. **43**, 431 (1931).

[156] N. W. Ashcroft and N. D. Mermin, *Solid State Physics* (Holt Rinehart and Winston, U.S.A., 1976).

[157] C. T. Naber, Review of Scientific Instruments **38**, 1161 (1967).

[158] H. Ohnishi, Y. Kondo, and K. Takayanagi, Nature **395**, 780 (1998).

[159] J. L. Costa-Kramer, N. Garcia, and H. Olin, Physical Review B **55**, 19 (1997).

[160] U. Landman, W. D. Luedtke, N. A. Burnham, and R. J. Colton, Science **248**, 454 (1990).

[161] M. S. Bronsgeest and P. Kruita, J. Vac. Sci. Technol. B **27**, 2524 (2009).

[162] Y. Hasegawa and P. Avouris, Physical Review Letters **71**, 7 (1993).

[163] P. Vancso, G. Z. Magda, J. Peto, J.-Y. Noh, Y.-S. Kim, C. Hwang, L. P. Biro, and L. Tapaszto, Nature Scientific Reports **6**, 29726 (2016).